

Mohamed Khider University of Biskra Faculty of Exact Sciences Material Sciences Department

MASTER DISSERTATION

Materials sciences
Physics
Physics of Materials

Ref.:

Presented by SLIM Sara

On: 02/06/2025

Stability issue in perovskite solar cells: Comparison between Conventional and Inverted Structures

Jury:

SENGOUGA Nouredine Prof University of Biskra President

MEFTAH Afak Prof University of Biskra Supervisor

OUAHAB Abdelouahab Prof University of Biskra Examiner

Academic Year: 2025

X Dedications **X**

Praise be to ALLAH at the beginning and at the end
To my parents, whose unwavering love, encouragement,
and sacrifices have been the cornerstone of my journey.

Your belief in me has been my guiding light
through every challenge and triumph.

This Dissertation is dedicated to you,
As a token of my deepest gratitude for your
endless support and inspiration.



Acknowledgments

I would like to express my sincere gratitude to my supervisor, Prof MEFTAH Afak, for their invaluable guidance, unwavering support, and constructive feedback throughout the process of researching and writing this dissertation. Their expertise, encouragement, and patience have been instrumental in shaping the direction of this work.

I am also deeply thankful to my committee members, Prof SENGOUGA Nouredine and Prof OUAHAB Abdelouahab, for graciously accepting to evaluate this dissertation. Their comments and suggestions will significantly enhance its quality.

I extend my appreciation to the staff and faculty of Exact Sciences, whose resources and facilities have provided me with the necessary tools to conduct my research effectively.

I am grateful to my friends and family for their understanding, encouragement, and unwavering support during this challenging journey. Their belief in me has been a constant source of motivation.

This dissertation would not have been possible without the contributions and support of these individuals, and for that, I am truly grateful.

ABSTRACT

In this work, the Solar Cell Capacitance Simulator (SCAPS) was used to investigate stability issues in perovskite solar cells (PSCs) with both P-I-N and N-I-P structures. The focus was on elucidating the impact of various types of defects caused by degradation processes related to illumination, thermal, and bias stresses, and on comparing the degradation severity in both structures. The defects (electron and hole deep and shallow traps) are created in the HTL/bulk interface, bulk, and bulk/ETL interface. The findings highlighted the critical influence of defect density on key performance metrics such as open-circuit voltage (V_{oc}) , short-circuit current density (J_{sc}) , fill factor (FF), and power conversion efficiency (PCE). Initially, the N-I-P structure exhibited a slight performance advantage (22.72%) due to a higher open-circuit voltage; 1.180 V vs. 1.145 V in P-I-N (22.41%). The initial electrical outputs prior to degradation showed good agreement with the experimental measurements for both structures. Under extreme defect conditions (bulk defects induced by thermal stress $N_R = N_{DA} = N_{DT} = N_{AT} = 10^{16} \text{ cm}^{-3}$), the N-I-P structure experienced a catastrophic drop in PCE to 2.430%, while the P-I-N structure maintained, under the similar condition, a PCE of 13.175%. These results suggest that P-I-N structures exhibit better defect tolerance, making them more suitable for long-term stability in defect-prone conditions.

Keywords: SCAPS, perovskite solar cell, stability issues, efficiency, defects.

ملخص

في هذا العمل، تم استخدام برنامج محاكاة السعة في الخلايا الشمسية (SCAPS) لدراسة مشكلات الاستقرار في خلايا بيروفسكايت الشمسية (PSCs) ذات التركيبتين P-I-N و N-I-P. ركزت الدراسة على توضيح تأثير الأنواع المختلفة من العيوب الناتجة عن عمليات التقهقر المرتبطة بالإجهادات الضوئية والحرارية والكهربائية، وعلى مقارنة شدة التقهقر في كلتا التركيبتين. يتم توليد العيوب (فخاخ إلكترونية وثقوبية عميقة وسطحية) عند واجهة طبقة النقل الثقوبي\الطبقة الفعالة، وفي الطبقة الفعالة نفسها، وعند واجهة الطبقة الفعالة \طبقة النقل الإلكتروني. أظهرت النتائج التأثير الحرج لكثافة العيوب على مؤشرات الأداء الرئيسية مثل جهد الدائرة المفتوحة (V_{oc}) ، وكثافة تيار الدائرة القصيرة (J_{sc}) ، وعامل الامتلاء (FF)، وكفاءة تحويل الطاقة (PCE). في البداية، أظهرت بنية N-I-P أفضلية طفيفة في الأداء (22.72%) نتيجة لجهد دائرة مفتوحة أعلى؛ حيث بلغ 1.180 فولت مقارنة بـ 1.145 فولت في بنية (P-I-N(22.41%). وقد أظهرت المخرجات الكهربائية الأولية قبل حدوث التقهقر توافقاً جيدًا مع القياسات التجريبية لكلتا التركيبتين. تحت ظروف عيوب قصوى (عيوب في الطبقة الفعالة ناجمة عن الإجهاد N-I-P الحرارى بقيم N-I-P $N_{CM}=N_{DA}=N_{DA}=N_{DT}=N_{AT}=10^{16}cm^{-3}$ المحرارى بقيم كارثي في كفاءة تحويل الطاقة لتصل إلى \$2.430، بينما حافظت بنية P-I-N، تحت نفس الظروف، على كفاءة قدرها \$13.175. تشير هذه النتائج إلى أن التركيبات من نوع P-I-N تظهر قدرة أكبر على تحمل العيوب، مما يجعلها أكثر ملاءمة للاستقرار طويل الأمد في البيئات المعرضة للعيوب.

الكلمات المفتاحية : (SCAPS)، خلايا بيروفسكايت الشمسية، مشكلات الاستقرار، المردود، العيوب.

Contents

D	edica	ations	11
Ac	knov	wledgments	iii
Ał	ostra	ct	iv
Li	st of	Figures	X
Li	st of	Tables	xii
Li	st of	Abbreviations	xiii
In	trod	uction	1
1	Per	ovskite Materials: Advances in Solar Cell Technology	3
	1.1	Introduction	3
	1.2	Fundamentals of Perovskite Materials	3
	1.3	Fabrication Techniques and Processing	5
	1.4	Perovskite Solar Cells	6
		1.4.1 Mesoporous Scaffold Architecture	7
		1.4.2 Planar Architecture	7
		1.4.3 ETL and HTL materials	8
		1.4.4 Electrical characterization	8
	1.5	Advancements and Challenges in Perovskite Solar Cells	10
		1.5.1 PSC Modules	10
		1.5.2 Tandem Devices	10
2	Stal	bility Issues In Perovskite Solar cells	12
	2.1	Introduction	12
	2.2	Major Stability Issues in Perovskite Solar Cells	13
		2.2.1 Environmental Degradation	14
		2.2.1.1 Humidity and Oxygen	14
		2.2.1.2 Light Induced Degradation	16
		2.2.1.3 Temperature Induced Degradation	17

		2.2.2	Structural Instability and Ion Migration	0
			2.2.2.1 Hole Transport Layer	0
			2.2.2.2 Metal Counter Electrode	1
			2.2.2.3 Effect of Interface	2
			2.2.2.4 Bias Voltage-Induced Degradation	3
		2.2.3	Lead Leaching Toxicity	4
	2.3	Alterr	native Stable Materials for Perovskites	6
		2.3.1	Mixed-Halide Perovskites	6
	2.4	Engin	eering Techniques for Stability Enhancement	7
		2.4.1	Encapsulation Technologies	8
		2.4.2	Interfacial Engineering for efficiency and stability	8
3	Def	ects in	Perovskite Solar Cells and Passivation Strategies 2	9
	3.1	Intro	duction	9
	3.2	Defec	ts in MAPbI ₃ Perovskite	0
	3.3	Defec	t Migration and Device Stability	1
	3.4	Passiv	vation Strategies	4
		3.4.1	Passivation of Defects in Perovskite Films	5
			3.4.1.1 Ionic Compounds	5
			3.4.1.2 Organic Molecules	5
		3.4.2	Passivation of Defects on the Surface of Perovskite	6
			3.4.2.1 Perovskite/Hole Transport Layer Interface	7
			3.4.2.2 Electron/Perovskite Transport Layer Interface	7
4	Stal	bility is	ssue- Comparison between P-I-N and N-I-P PSCs 3	8
	4.1	Intro	duction	8
	4.2	SCAP	S	9
		4.2.1	Definition of the problem	0
		4.2.2	Define the working point	0
		4.2.3	Selection of the measurement(s) to simulate	0
		4.2.4	Starting the calculation(s)	1
		4.2.5	Displaying the simulated curves	1
	4.3	Mater	rial inputs and defects used to simulate the working condition 4	2
	4.4	Resul	ts and discussion	4
		4.4.1	Initial case	4
		4.4.2	Effect of defects at the HTL/bulk interface	5
		4.4.3	Effect of defects in the bulk	7
		4.4.4	Effect of defects at Bulk/ETL interface	1
	4.5	Conc	usion 5	4

Conclusion	55
Bibliography	56

List of Figures

1.1	Structural illustration of ABX3 Perovskite [3]	4
1.2	Typical one and two-steps deposition methods for MAPbI $_3$ Perovskite [22]	6
1.3	Basic structure of PSC	7
1.4	Architectures of perovskite SC in n-i-p and p-i-n configurations [22]	7
1.5	J-V characteristic and electrical outputs of a solar cell	9
1.6	Example of J-V characteristics measured for (a) standard and (b) inverted PSCs	
	[24]	9
1.7	PSCs small module illustration [3]	10
1.8	Illustration of Tandem Solar cell	11
2.1	Timeline of the development of the PSCs conversion efficiency	13
2.2	Degradation in PSCs by: (1) illumination, (2) heat, (3) electrical bias, and (4)	
	atmosphere (moisture and oxygen). (a) halide/phase segregation, (b) forma-	
	tion of hydrates, crystal decomposition (c) releasing volatile molecules methy-	
	lamine (MA), I2, NH3, and HI or (d) forming precipitates (Pb0, I2, etc.), and (e)	
	morphology changes [44]	14
2.3	Degradation of MAPbI3 by oxidation and humidity [50]	15
2.4	light-induced degradation mechanism in MAPbI3 [51]	17
2.5	Schematic illustration of thermal degradation processes in MAPbI3 [52]	18
2.6	Schematic illustration of metal counter electrode degradation processes in OInH-counter electrode degradation and the counter electrode degradat	
	PSCs [61]	22
2.7	Illustration of an example of bias voltage-induced degradation in OInH-PSCs	
	[67]	25
2.8	Relation between the perovskite structure and the Goldschmidt tolerance fac-	
	tor [69]	26
2.9	Structure illustration of 2D, Quasi 2D, and 3D- Perovskites [75]	27
3.1	Imperfections in MAPbI ₃ perovskite [83]	31
3.2	The transition energy levels of (a) intrinsic acceptors and (b) intrinsic donors	
	in MAPhI ₂ [83]	32

3.3	Schematic diagram of the MAPbI ₃ perovskite structure and diffusion paths of	
	the point defects [92]	33
3.4	The various defects and ions generated under illumination in the perovskite	
	solar cell device structure [92]	34
3.5	$Illustration \ of \ the \ coating \ process \ utilized \ to \ create \ CH_3NH_3PbI_3 \ films \ with \ and$	
	without excess MAI [107]	36
4.1	The SCAPS start-up panel: the Action panel or main panel	39
4.2	Definition of problem panel and selection of example	40
4.3	Definition of the working point	41
4.4	Selection of the measurement(s) to simulate	41
4.5	Results panels	42
4.6	: Simulation procedure using SCAPS software	42
4.7	The studied structures of the P-I-N and N-I-P PSC	44
4.8	J-V characteristic calculated by SCAPS for initial case, i.e. low defect densities:	
	(a) in P-I-N PSC ,(b) in N-I-P PSC	44
4.9	J-V characteristic of the P-I-N PSC calculated by SCAPS when defects are at	
	the HTL/bulk interface: (a) recombination center, (b) shallow donor and (c)	
	shallow accepter.	45
4.10	: Comparison of the effect of HTL/bulk interface defects in P-I-N PSC and N-I-P	
	PSC	47
4.11	J-V characteristic of the P-I-N PSC calculated by SCAPS when defects are in the	
	bulk of the perovskite: (a) recombination center, (b) deep donor, (c) shallow	
	donor and (d) shallow accepter.	48
4.12	Comparison of the effect of the bulk defects in P-I-N PSC and N-I-P PSC	50
4.13	J-V characteristic calculated by SCAPS when defects are at the bulk/ETL inter-	
	face: (a) recombination center, (b) shallow donor and (c) shallow acceptor	51
4.14	: Comparison of the effect of the bulk/ETL defects in P-I-N PSC and N-I-P PSC.	53

List of Tables

2.1	Summary of some device architectures and theirs stability for PSCs [39]	14
4.1	Material's inputs used in the simulation for the P-I-N PSC [123]	43
4.2	Material's inputs used in the simulation for the N-I-P PSC [124, 125]	43
4.3	Initial electrical outputs (Before degradation) compared to experimental mea-	
	surements. Data for the P-I-N PSC are from [126, 128] and data for the N-I-P	
	PSC are from [127]	45
4.4	Effect of HTL/bulk interface defects on electrical output of the P-I-N PSC when	
	defect density of N_R was varied from 10^{11} to 10^{14} cm ⁻²	46
4.5	Effect of HTL/bulk interface defects on electrical output of the P-I-N PSC when	
	defect density of N_{AT} was varied from 10^{11} to 10^{14} cm ⁻²	46
4.6	Effect of HTL/bulk interface defects on electrical output of the P-I-N PSC when	
	defect density of N_{DT} was varied from 10^{11} to 10^{14} cm ⁻²	46
4.7	Effect of HTL/bulk interface defects on electrical output of the P-I-N PSC when	
	all defect densities N_R , N_{DT} , and N_{AT} are equal to $10^{14}~{\rm cm}^{-2}$	46
4.8	Comparison of the effect of HTL/bulk interface defects in P-I-N PSC and N-I-P	
	PSC when all defect densities N_R , N_{DT} , and N_{AT} are equal to $10^{14}~{\rm cm}^{-2}$	47
4.9	Effect of the bulk defects on electrical output of the P-I-N PSC when defect	
	density of N_R is varied from 10^{14} to 10^{16} cm $^{-3}$	47
4.10	Effect of the bulk defects on electrical output of the P-I-N PSC when defect	
	density of N_{DP} changes from 10^{14} to 10^{16} cm ⁻³	49
4.11	Effect of the bulk defects on electrical output of the P-I-N PSC when defect	
	density of N_{DT} is varied from 10^{14} to 10^{16} cm ⁻³	49
4.12	Effect of the bulk defects on electrical output of the P-I-N PSC when defect	
	density of N_{AT} is varied from 10^{14} to 10^{16} cm ⁻³	49
4.13	Effect of the bulk defects on electrical output of the P-I-N PSC when all defect	
	densities N_R , N_{DT} , N_{DP} , and N_{AT} are equal to 10^{16} cm ⁻³	49
4.14	Comparison between P-I-N PSC and N-I-P PSC of the bulk defect's effect when	
	all defect densities N_R , N_{DT} , N_{DP} , and N_{AT} are equal to $10^{16}~{\rm cm}^{-3}$	49
4.15	Effect of the bulk/ETL interface defects on electrical output of the P-I-N PSC	
	when defect density of N_R is varied from 10^{11} to 10^{14} cm ⁻²	52

4.16	Effect of the bulk/ETL interface defects on electrical output of the P-I-N PSC	
	when defect density of N_{DT} is varied from 10^{11} to 10^{14} cm ⁻²	52
4.17	Effect of the bulk/ETL interface defects on electrical output of the P-I-N PSC	
	when defect density of N_{AT} changes from 10^{11} to 10^{14} cm ⁻²	52
4.18	Effect of the bulk/ETL interface defects on electrical output of the P-I-N PSC	
	when all defect densities N_R , N_{DT} , and N_{AT} are equal to $10^{14}~{\rm cm}^{-2}$	52
4.19	Comparison of the effect of the bulk/ETL interface defects in P-I-N PSC and	
	N-I-P PSC when all defect densities N_B , N_{DT} , and N_{AT} are equal to 10^{14} cm ⁻² .	53

List of Abbreviations

Abbreviation	Description
PSCs	Perovskite Solar Cells
$MAPbI_3$	Methylammonium Lead Iodide
ETL(M)	Electron Transport Layer (Material)
HTL(M)	Hole Transport Layer (Material)
J-V	Density of Current - Voltage Characteristic
J_0	Dark Saturation Current Density
J_{ph}	Photo-current Density
V_{oc}	Open Circuit Voltage
$k_{\rm B}$	Boltzmann Constant
J_{sc}	Short Circuit Current Density
$V_{\rm m}$	Voltage at which the solar cell operates most
	efficiently
$J_{\mathbf{m}}$	Current Density at which the solar cell oper-
	ates most efficiently
PCE	Photo-Conversion Efficiency
FF	Fill Factor
E_{g}	Band Gap Energy
DSSCs	Dye-sensitized solar cells
OSCs	Organic solar cells
PV	Photovoltaic
t	Tolerance factor
μ	Octahedral factor
CdTe	Cadmium telluride
FTO	Fluorine-doped tin oxide
CaTiO ₃	Calcium titanium oxide
Si	Silicon
TiO_2	Titanium dioxide
	Continued on next page

xiii

Abbreviation	Description		
ITO	Indium Tin Oxide		
EQE	External quantum efficiency		
OMeTAD	Organic Metal Halide Absorber		
SCAPS	Solar Cell Capacitance Simulator		
PEDOT:PSS	Poly(ethylenedioxythiophene):poly(styrene		
	sulfonic acid)		
DR	Degradation rate		
QDs	Quantum dots		
BA	Butyl amine		
PEA	Phenylethylamine		
HAADF	High-angle annular dark-field		
PL	Photoluminescence		
V_{MPP}	Maximum power point voltages		
SRH	Shockley–Read–Hall		
O-InH	Organic-Inorganic Hybrid		
CB	Conduction band		
VB	Valence band		
Pb	Lead		
$N_{\rm C}$	Effective density of conduction band		
N_{V}	Effective density of valence band		
E _C	Conduction Band Edge		
E_V	Valence Band Edge		
N_R	Recombination center		
N_{DT}	Shallow donor		
N_{DP}	Deep donor		
N_{AT}	Shallow acceptor		
Homo	Highest occupied molecular orbital		
Lumo	Lowest unoccupied molecular orbital		

Introduction

Electricity consumption is crucial for modern life, but global demand is surpassing energy production capabilities. Currently, fossil fuels such as oil, coal, and gas are the predominant sources of electricity due to their convenience. However, these fuels are finite, meaning their reserves will eventually be exhausted. Additionally, their combustion releases significant carbon emissions, posing substantial environmental risks [1, 2]. Transitioning from fossil fuels to clean, renewable energy sources is paramount and in high demand. Embracing environmentally friendly technologies alongside renewable energy is essential for global progress. Advances in energy conversion and management technologies are rapidly improving across natural and renewable resources like wind, solar, hydro, and biomass. Among these, solar photovoltaic (PV) technology is particularly notable for its effectiveness and promise. Solar energy is abundant and widely recognized as the most abundant renewable energy source on the planet [1,2].

Photovoltaic (PV) technology directly converts solar energy into electricity, providing a sustainable solution to meet global energy demands cleanly. Research since the 1950s has yielded various PV concepts, including monocrystalline, multi- and polycrystalline materials, and advanced technologies like quantum dots and perovskites. Despite advancements, PVs currently contribute minimally to global energy consumption. Silicon-based cells dominate the market but face limitations such as low absorption coefficients and high production costs. Researchers aim to enhance efficiency and reduce costs through alternatives like thin-film and nanocrystal-based cells [1–5].

The efficiency of PV cells, crucial for cost reduction, has a theoretical limit of 33.7% as calculated by Shockley and Queisser in 1961 for single-junction solar cells under standard conditions. Achieving this limit remains a focus for advancing PV technology [3,6].

Among the various types of 3rd generation PV devices, the perovskite solar cells (PSCs) have received greater attention from the scientific community. In the year 2009, based on the DSSC technology, the PSC was introduced as a potential renewable energy PV technology. In PSCs, key material is the perovskite which formed by the organic–inorganic mixed compound [2,3].

PSCs show promise as a transformative PV technology due to their low cost, high efficiency, and ease of processing. PSCs have rapidly increased in efficiency from 3.8% to 25.8% within a short timeframe, surpassing many established PV technologies like silicon (Si), cad-

mium telluride (CdTe), and gallium arsenide (GaAs) based solar cells. However, their stability has not yet matched that of commercial solar cells. A significant challenge lies in the instability of perovskite materials, which contain elements prone to degradation. The stability of perovskite technology is heavily influenced by environmental factors such as humidity, thermal conditions, and light exposure. In addition, challenges remain before their widespread commercialization, including scaling up production to fabricate efficient large-area modules and managing concerns related to the toxicity of materials and manufacturing processes involved [2, 7, 8].

The aim of this study is to simulate the stability issues in two structures of perovskite solar cells (PSCs), namely P-I-N and N-I-P. To achieve this, we employ the Solar Cell Capacitance Simulator (SCAPS) as a simulation tool to investigate the impact of various defects induced by degradation processes. Our focus is on understanding how these defects influence device performance. Through a comprehensive analysis, we aim to elucidate the relationship between defect formation and performance degradation in both structures. Additionally, a comparative study between the P-I-N and N-I-P architectures will be conducted to identify which configuration offers greater stability and reliability. Ultimately, this research seeks to contribute to the development of more durable and efficient perovskite solar cell technologies

Chapter 1

Perovskite Materials: Advances in Solar Cell Technology

1.1 Introduction

Perovskite solar cells (PSCs) have garnered significant attention as a promising photovoltaic (PV) technology for cost-effective solar electricity. Their rapid rise in efficiency, achieved through a low-cost and straightforward fabrication process, has made them competitive with established technologies [9, 10].

Since the introduction of organometal halide perovskite as a visible-light absorber in 2009, with an initial efficiency of 3.8%, PSCs have made remarkable progress. By 2020, they achieved a world-record efficiency of 25.5%, comparable to state-of-the-art crystalline silicon cells dominating the PV market [11]. This advancement is credited to the unique properties of organic-inorganic hybrid metal trihalide perovskite materials, such as strong light absorption, minimal exciton binding energy, and efficient charge carrier transport with long diffusion lengths [9, 10, 12, 13].

The development of various PV technologies, including PSCs, silicon cells, dye-sensitized solar cells (DSSCs), and organic solar cells (OSCs), has significantly reduced the cost of solar electricity, making it competitive with conventional energy sources [9, 10]. This chapter explores the latest developments and innovations in perovskite-based solar cells, highlighting their potential to reshape the renewable energy field.

1.2 Fundamentals of Perovskite Materials

A perovskite solar cell (PSC) utilizes a metal halide perovskite compound as its light-absorbing material. These compounds have a general chemical formula of ABX₃, where A and B are cations of differing atomic radii (with A larger than B), and X is an anion. The crystal structure of these organic-inorganic hybrid metal halide perovskites is similar to calcium titanium

oxide (CaTiO₃), a mineral first identified by Russian mineralogist L. A. Perovski. In the 1920s, Goldsmith described the ABX₃ perovskite structure based on this mineral, naming it after Perovski [3, 9, 14, 15].

In metal halide perovskites, the A-site cation is typically monovalent, such as methylammonium ($CH_3NH_3^+$, MA^+), formamidinium ($(NH_2)_2CH^+$, FA^+), cesium (Cs^+), or their combinations. The B-site cations are bivalent metals from Group IV of the periodic table (e.g., Pb^{2+} , Sn^{2+}), while the X site is occupied by a halide anion (Cl^- , Br^- , I^-). In the crystal structure as shown in Figure 1.1, the B-site cation resides at the center of corner-linked octahedra formed by X-site anions [3, 9].

The cubic structure of perovskites often undergoes distortion due to the varying ionic sizes of A^- , B^{2+} , and X^- , resulting in tunable optical, electronic, magnetic, and dielectric properties. Research efforts primarily focus on optimizing the A^- and X-site configurations, as changes in the B-site composition, particularly from the conventional lead (Pb), pose challenges due to instability in the perovskite phase [9, 16].

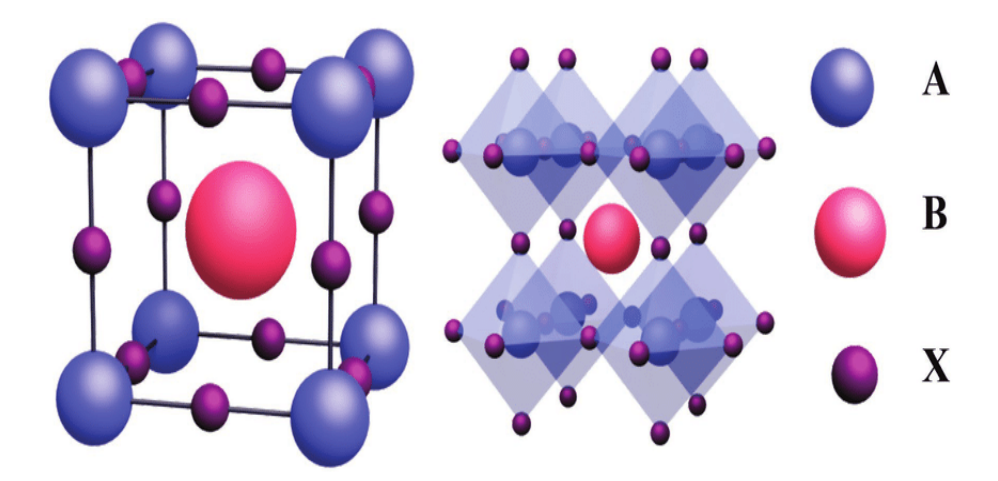


Figure 1.1: Structural illustration of ABX3 Perovskite [3].

The crystallographic stability of a perovskite material structure is predicted by two factors; a tolerance factor t and an octahedral factor μ which are defined as [3, 9, 17]:

$$t = \frac{r_A + r_X}{\sqrt{2}[r_B + r_X]} \tag{1.1}$$

$$\mu = \frac{r_B}{r_X} \tag{1.2}$$

where r_A , r_B and r_X are the ionic radii of elements A, B and X. For a cubic high stability structure; t must be close to 1 and μ between 0.44 and 0.9.

Additional qualities, along with their tunable composition and optoelectronic properties, contribute to their potential in solar energy applications. Perovskite material for photovoltaic exhibit outstanding characteristics such as high absorption coefficients, low exciton binding energies, tolerance to defects, large diffusion lengths, and high charge mobilities [3].

MAPbI₃ (Methylammonium Lead Iodide), the pioneering perovskite studied extensively since its first report in 2009 by Miyasaka and colleagues [12], exhibits three distinct phases depending on temperature: orthorhombic below -113°C, tetragonal from -113°C to approximately 57°C, and pseudocubic above 57°C. The phase transition near 57°C, achievable under sunlight, could potentially influence the performance of perovskite solar cell devices [3, 18, 19]. It is possible to control the luminescence color of MAPbX₃ (where X = Cl, Br, I) perovskites by changing the halide anions. For instance, MAPbCl₃, with a wide bandgap of approximately 3.1 eV, is suitable for light-emitting diode applications. On the other hand, MAPbBr₃ (bandgap $E_g = 2.3$ eV) and mixed-halide perovskite MAPbI_xBr_{3-x} are preferred for tandem devices. MAPbI₃, with an absorption edge at approximately 780 nm ($E_g = 1.53$ eV), is highlighted for its potential use as a light absorber in single-junction photovoltaic devices (PV) [3].

In addition to MAPbX₃ perovskites, there are other notable perovskite materials such as FAPbX₃ (formamidinium lead halide perovskites) and CsPbX₃ (cesium lead halide perovskites). Compared to MAPbX₃, FAPbX₃ is characterized by: Smaller bandgap, Higher thermal stability, higher annealing temperature (~ 150 °C) due to the larger FA cation, Instability of the cubic α -phase at room temperature, prone to transforming into the undesirable δ -phase with a larger bandgap, Mixed-cation perovskites with smaller MA cation improve phase stability [2, 3]. In the other hand, CsPbX₃ is characterized by: excellent thermal stability (stable even at 400 °C), larger bandgap (1.73 eV) suitable for tandem device applications as the top subcell, similar phase transition issue from the stable α -phase to the undesirable δ -phase in the presence of moisture [3, 20].

In this study, our focus remains on $MAPbX_3$ due to its status as the pioneering material in perovskite research, and being the most susceptible to instability issues.

1.3 Fabrication Techniques and Processing

Perovskite device fabrication employs a variety of techniques: vapor deposition, one-step and two-step solution methods, and hybrid processes. Vapor deposition methods include co-evaporation and sequential evaporation. Solution methods utilize spin coating (one-step) and dip coating (two-step). Hybrid processes integrate both vapor and solution techniques [21,22]. Conventional thin-film solar cells predominantly rely on vapor-phase deposition for large-scale production. While vapor-phase deposition is feasible for perovskite solar cells (PSCs), it is less cost-effective and operationally advantageous compared to solution-based approaches. The ionic properties of organic hybrid perovskites enable the use of low-temperature solution methods that are well-suited for scalable manufacturing. Spin coating stands out in laboratory environments for its straightforward application and high efficiency [3].

Perovskite device fabrication employs one-step and two-step solution-based methods

utilizing both liquid and gas phases for chemical processing (see Figure 1.2). In the one-step method, a solution containing CH_3NH_3I and PbI_2 , essential for $CH_3NH_3PbI_3$ perovskites, is prepared and applied onto a substrate with a transport layer. Heat treatment follows to ensure the formation of the perovskite layer. The two-step method offers two approaches: sequential deposition of CH_3NH_3I and PbI_2 solutions followed by annealing, or deposition of PbI_2 followed by immersion in CH_3NH_3I solution and subsequent heat treatment. The two-step method is hindered by challenges such as reproducibility and uniformity issues, favoring the one-step method for solar cell fabrication due to its superior control and reliability in layer formation [21,22].

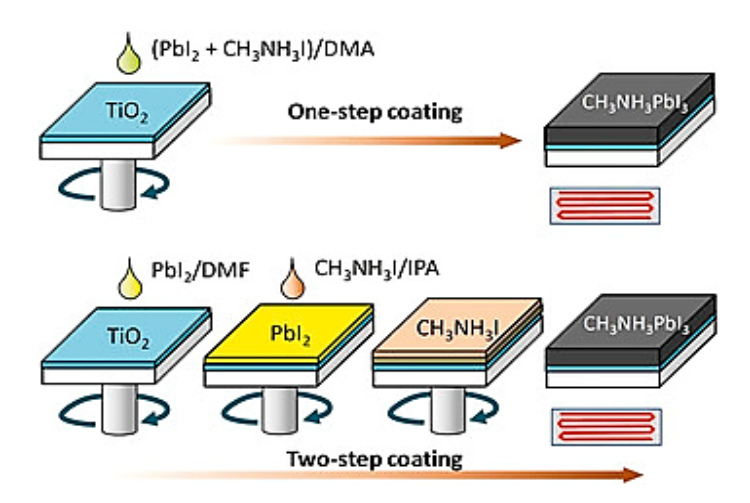


Figure 1.2: Typical one and two-steps deposition methods for MAPbI₃ Perovskite [22].

1.4 Perovskite Solar Cells

Perovskite solar cells (PSCs) have evolved from classical dye-sensitized solar cells (DSSCs). A typical PSC structure consists of a perovskite layer, which serves as the active material for light absorption. This layer is positioned between an Electron Transport Layer (ETL), typically composed of TiO₂ nanoparticles, responsible for collecting photo-generated electrons, and a Hole Transport Layer (HTL). The HTL is commonly an organic material like spiro-OMeTAD, though it can also be an inorganic material such as a p-type transparent oxide.

When exposed to light, the perovskite layer generates excitons that separate into free electrons and holes within the absorber layer. Electrons migrate towards the ETL, while holes move towards the HTL. By connecting the PSC to an external circuit, it can generate electric power based on the photogenerated current and voltage. Figure 1.3 provides a visual representation of this process.

Perovskite solar cells (PSCs) exhibit various device designs based on their fundamental building blocks and fabrication methods. The main architectures are mesoporous and planar, each with unique characteristics and applications (Figure 1.4) [22].

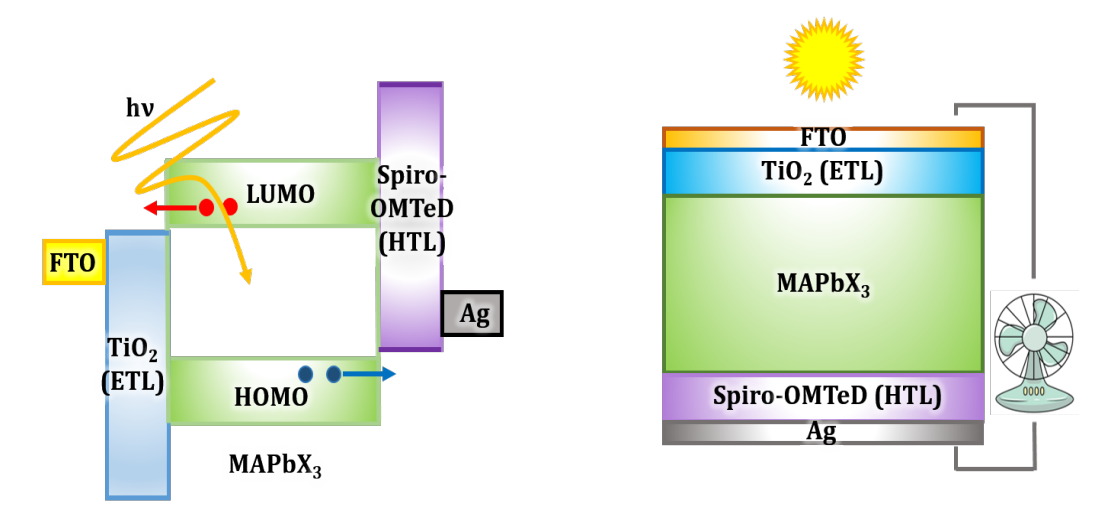


Figure 1.3: Basic structure of PSC.

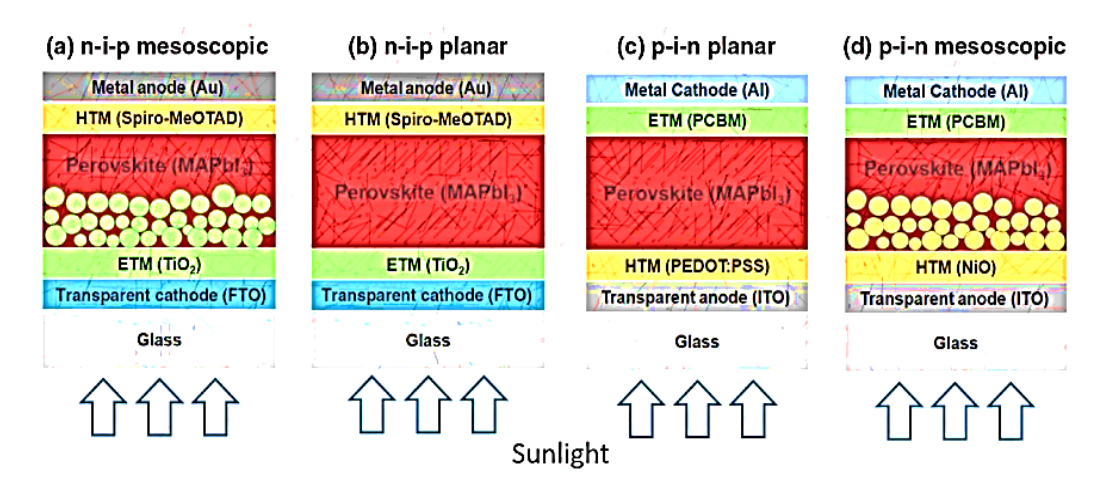


Figure 1.4: Architectures of perovskite SC in n-i-p and p-i-n configurations [22].

1.4.1 Mesoporous Scaffold Architecture

- This architecture is predominant in PSCs and is similar to the structure of solid-state dye-sensitized solar cells (DSSCs).
- Nanoparticles are sintered onto a TiO₂ layer to create porosity, allowing the perovskite material to self-assemble within the mesoporous TiO₂ network.
- The mesoporous TiO₂ is crucial for facilitating electron transfer between the perovskite layer and the fluorine-doped tin oxide (FTO) electrode.
- The mesoporous PSCs are categorized into two types: standard (n-i-p) and inverted (p-i-n) configurations, based on the sequence of layer deposition.

1.4.2 Planar Architecture

This design closely resembles conventional silicon-based solar cells.

- Planar PSCs are categorized into two types: standard (n-i-p) and inverted (p-i-n) configurations.
- It generates higher V_{OC} and J_{SC} compared to mesoscopic cells but suffers from J-V hysteresis issues.
- Advances in fabrication techniques have allowed for highly efficient planar PSCs without the need for a mesoporous layer.

1.4.3 ETL and HTL materials

ETLs are particularly useful for extracting electrons and blocking holes from the active layer of PSCs. These n-type semiconductors possess the fewest vacant molecular orbitals and the highest electron mobility. Examples include fullerene derivatives like PC61BM and C60, as well as inorganic metal oxides like TiO₂, SnO₂, and ZnO [2].

Similarly, HTLs are crucial for extracting holes and blocking electrons. Numerous p-type semiconductors have been proposed as HTLs, including both organic and inorganic materials such as spiro-OMeTAD, PEDOT , P3HT, CuSCN, NiOx, Cu₂O, CuO, and many others [2]. Finding the optimal ETL and/or HTL for achieving highly stable PSCs remains a significant challenge [2].

1.4.4 Electrical characterization

A solar cell's principal characteristics are typically defined by its current-voltage (J-V) curves and electrical outputs. The J-V curve, a plot of current density (J) versus voltage (V), is crucial in assessing the performance of a solar cell (see Figure 1.5). Key parameters derived from this curve include the open-circuit voltage (V_{oc}), which is the maximum voltage the cell can produce when not connected to a load; the short-circuit current density (J_{sc}), representing the maximum current per unit area generated when the voltage across the cell is zero; the fill factor (FF), which indicates the squareness of the J-V curve and is a measure of the quality of the solar cell; and the power conversion efficiency (PCE), which quantifies the cell's ability to convert sunlight into electrical energy. These electrical outputs are essential for evaluating and comparing the effectiveness of different solar cell materials and designs. According to the simple model of an ideal solar cell, the J-V characteristic can be described by the following equation [23]:

$$J(V) = J_0 \cdot (e^{\frac{qV}{k_B T}} - 1) - J_{ph}$$
(1.3)

From which Voc can be estimated as:

$$V_{oc} = \frac{k_B T}{q} \cdot ln \left(\frac{J_{sc}}{J_0} + 1 \right) \tag{1.4}$$

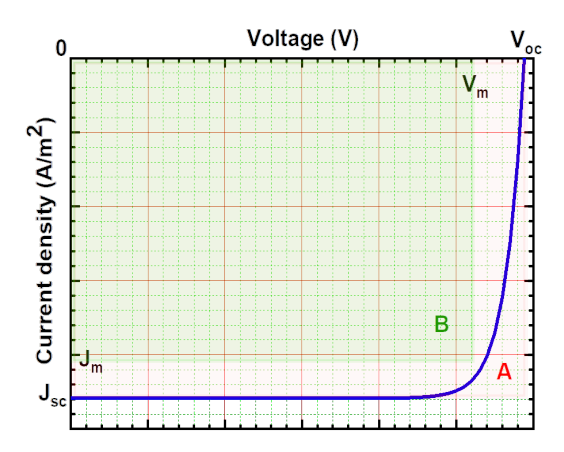


Figure 1.5: J-V characteristic and electrical outputs of a solar cell.

The power conversion efficiency (PCE) is given by:

$$PCE(\%) = \frac{J_m \cdot V_m}{P_{ins}} \tag{1.5}$$

and the Fill Factor by:

$$FF(\%) = \frac{J_m \cdot V_m}{J_{sc} \cdot V_{oc}} = \frac{B}{A} \tag{1.6}$$

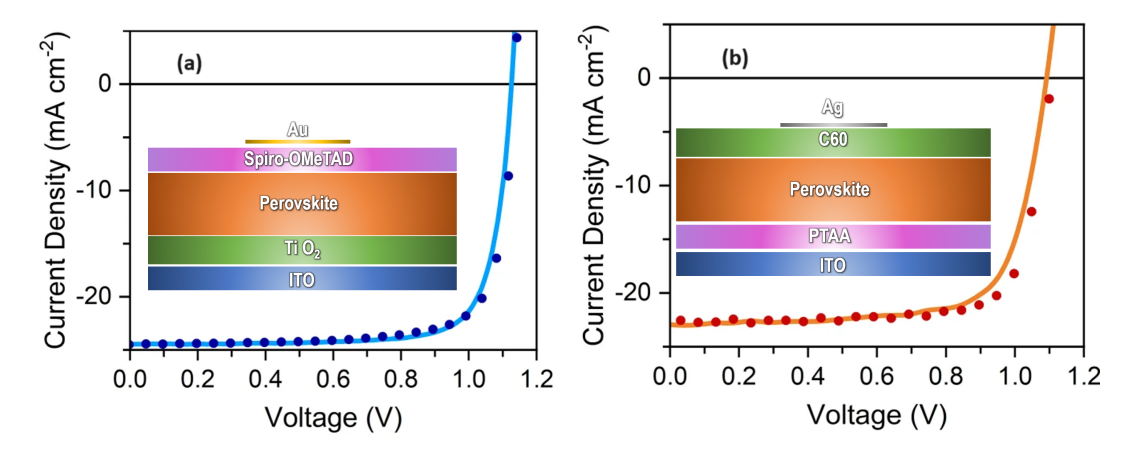


Figure 1.6: Example of J-V characteristics measured for (a) standard and (b) inverted PSCs [24]

Figure 1.6 as reported in reference [24], presents the measured J-V characteristics, showing a power conversion efficiency (PCE) of 20.9% for the n-i-p cell, with a J_{sc} of of 24.4 mA/cm², an V_{oc} of 1.13 V, and a fill factor of 0.76 . The p-i-n cell demonstrated a PCE of 19.1% , with a J_{sc} of 22.8 mA/cm², an V_{oc} of 1.10 V, and a fill factor of 0.76.

1.5 Advancements and Challenges in Perovskite Solar Cells

1.5.1 PSC Modules

Despite the rapid increase in efficiencies of small-area perovskite solar cells (PSCs) in recent years, large-area PSCs still lag behind. This performance loss in larger devices is due to factors such as nonuniform films, higher series resistance, lower shunt resistance, and dead areas—regions that do not contribute to power generation, often due to interconnections and obstructions [3].

To mitigate resistance losses, a common strategy is to divide large cells into smaller subcells with series interconnections. Researchers have been developing PSC modules with these interconnections to bridge the efficiency gap between small-scale cells and large-area modules. However, transitioning from laboratory-scale to practical modules presents challenges, including defining module area (the physical dimensions and active area of a photovoltaic module for power generation), laser-scribing, interconnections, standardized testing, and encapsulation. Laser-srcibing means the separation of individual solar cells within a module. By creating scribe lines, large solar cells can be divided into smaller subcells, which can then be interconnected in series to improve overall module efficiency [3] (Figure 1.7).

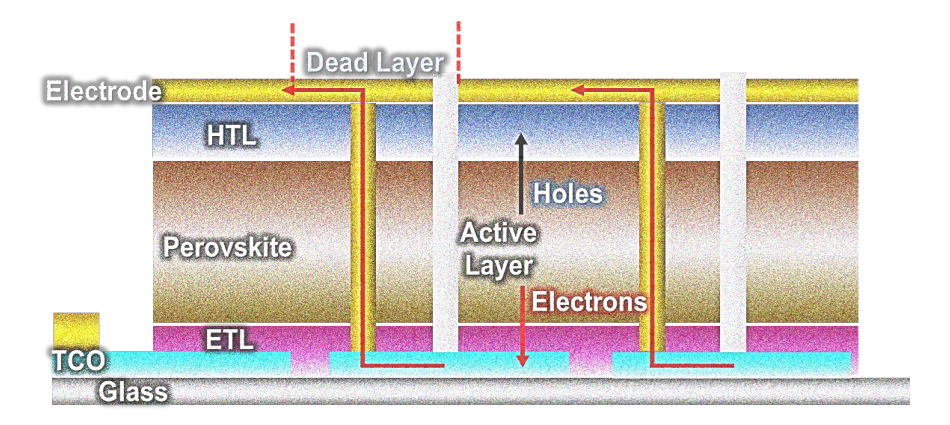


Figure 1.7: PSCs small module illustration [3]

Additionally, considerations for the cost of PSC modules and the development of largearea tandem devices are essential for commercialization [3, 22].

1.5.2 Tandem Devices

The commercialization of perovskite/silicon tandem solar cells depends on scaling up from initial small-area prototypes. Early research focused on devices below 1 cm 2 , with early tandem cells achieving modest efficiencies due to limitations in perovskite subcell performance [3]. In recent advancements, a wider-bandgap perovskite variant (CsFAPbI_{3-x}Br_x) was pivotal, achieving a certified power conversion efficiency (PCE) of 23.6% [3, 25] for a 1 cm 2

2-T Perovskite/Si tandem solar cell . Oxford PV achieved a significant breakthrough with a record-breaking PCE of 28% [3].

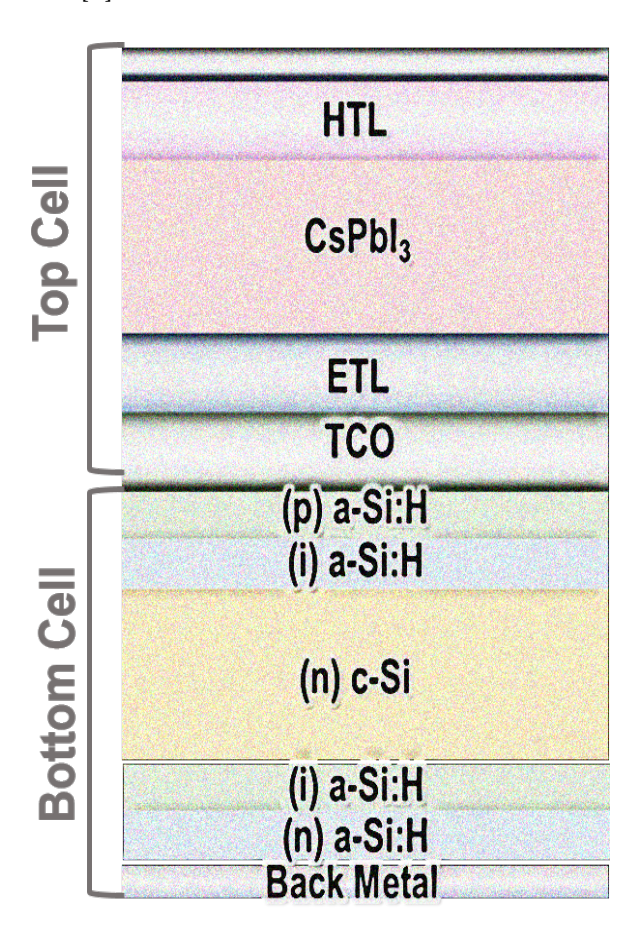


Figure 1.8: Illustration of Tandem Solar cell

The improvement in efficiency from 20% for a single perovskite solar cell to 28% for the tandem $CsFAPbI_{3-x}Br_x$ /silicon hybrid solar cell is attributed to the organic-inorganic hybrid nature of the $CsFAPbI_{3-x}Br_x$ layer. In addition, Tandem solar cells combine two or more semi-conductors with different band gaps. In the case of $CsFAPbI_{3-x}Br_x$ and silicon, $CsFAPbI_{3-x}Br_x$ has a larger band gap than silicon, allowing it to absorb higher-energy photons (blue and green light) that silicon cannot efficiently absorb. By stacking $CsFAPbI_{3-x}Br_x$ on top of silicon, both materials can complement each other's absorption spectra, ensuring more efficient utilization of the solar spectrum.

Chapter 2

Stability Issues In Perovskite Solar cells

2.1 Introduction

Recent advancements in organometal halide perovskite solar cells (PSCs) underscore the potential of these devices to achieve high power conversion efficiencies (PCE) and lower production costs, making them viable competitors to silicon-based photovoltaic (PV) technology, which offers long-term stability and lifespans of over 25 years [26,27]. Initial studies by Miyasaka et al. [28] demonstrated a 3.81% efficiency using $CH_3NH_3PbI_3$ as a light-absorbing material with a TiO_2 mesoporous structure. Subsequently, Etgar et al. [29] improved the design by demonstrating $CH_3NH_3PbI_3$'s dual functionality as both a light harvester and hole transport material (HTM), achieving a 5.5% efficiency.

To address early stability issues, researchers turned to solid-state HTMs. In particular, spiro-MeOTAD was introduced by Kim et al. [30], resulting in a 9.7% efficiency and significant improvement in stability by eliminating the degrading liquid electrolyte. This marked a pivotal development, as previously PSCs experienced rapid degradation upon exposure to moisture and ambient conditions [31]. Continued research on mixed halide perovskites, such as $CH_3NH_3PbI_{3-x}Cl_x$, has led to increased stability and improved charge transport, achieving efficiencies up to 10.9% [32].

With innovations in material composition and device architecture, efficiencies have climbed steadily. Seok et al. [33] reported a PCE of 12.3% with $CH_3NH_3PbI_{3-x}Br_x$, where the bromine's smaller ionic radius enhanced structural stability. By 2014, Jeon et al. [34] achieved a PCE of 20.1% through a combination of methylammonium (MA) and formamidinium (FA) cations. High-performance devices with PCEs of 20.26% on rigid substrates and 17.41% on flexible substrates were subsequently reported by Chen et al. [35, 36] using Cu-doped NiO_x as an HTL.

Further developments have introduced hole transport bilayers, such as NiO/Cu:NiO bilayers, which enhance hole transfer and suppress recombination at the NiO/perovskite interface, achieving a stable PCE of 18.3% after 350 hours [37]. More recently, Min et al. [38]

fabricated PSCs with interlayer modifications that reduced interface defects, resulting in a record PCE of 25.8% and maintaining 90% of initial efficiency after 500 hours of continuous light exposure [2, 39].

Despite these efficiency improvements, PSCs face stability challenges, especially under environmental stressors such as humidity, temperature, and light. Perovskite materials are inherently unstable due to weak interactions within the crystal lattice, such as van der Waals forces and hydrogen bonds [40,41]. The long-term stability of PSCs depends heavily on controlling these environmental factors [2]. For PSC technology to become commercially viable, stability under real-world conditions must match that of silicon and other established PV technologies [2,39,42].

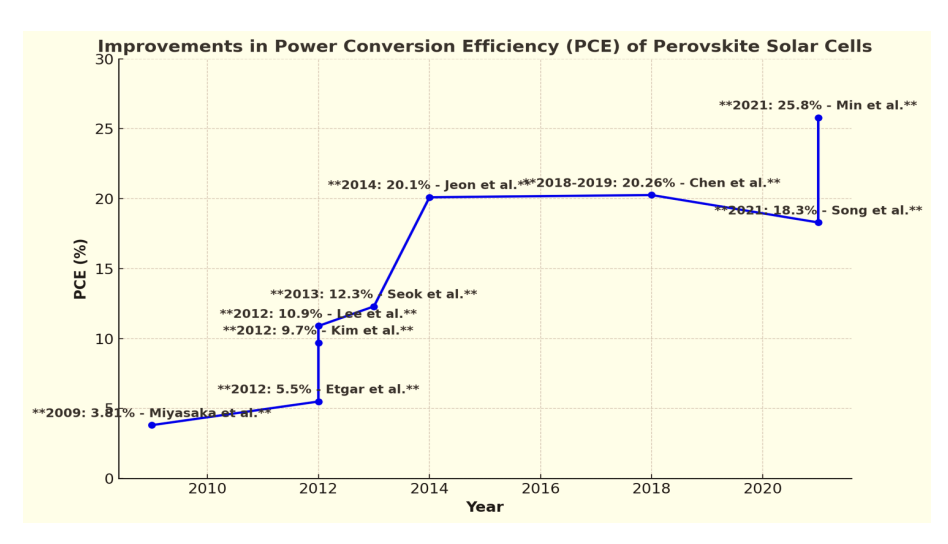


Figure 2.1: Timeline of the development of the PSCs conversion efficiency.

This chapter is organized as follows:

- Major Stability Issues in Perovskite Solar Cells: Environmental Degradation, Structural Instability and Ion Migration, and Lead Leaching Toxicity.
- Alternative Stable Materials for Perovskites.
- Engineering Techniques for Stability Enhancement: Encapsulation Technologies and Interfacial Engineering.

2.2 Major Stability Issues in Perovskite Solar Cells

The challenge of achieving long-term stability in metal halide perovskite-based solar cells, which are supposed to last for over 25 years, remains significant. The stability of perovskites is hindered by various degradation mechanisms. Perovskites are highly sensitive to environmental factors such as humidity, oxygen, and light. They tend to absorb water easily, especially when not properly encapsulated, leading to degradation. Additionally, light exposure can break weak chemical bonds in the perovskite structure or its interface with contact

layers, creating defects such as halogen vacancies, which facilitate the migration of halogens and further degradation [39, 42–45]. In Table 2.1 was presented a summary of some PSCs device architectures and theirs stability [39]. Figure 2.2 is an imaginary illustration which summarizes the different intrinsic and extrinsic types of the degradation.

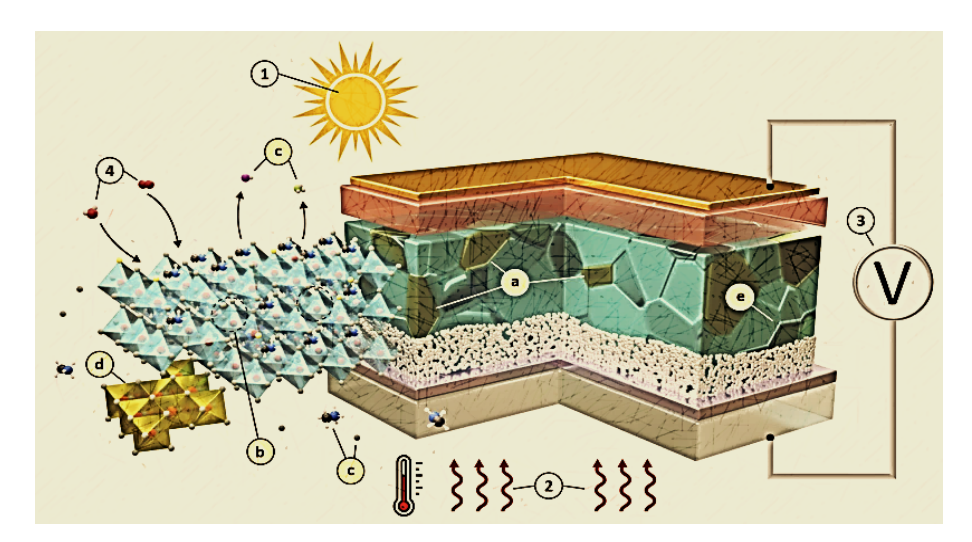


Figure 2.2: Degradation in PSCs by: (1) illumination, (2) heat, (3) electrical bias, and (4) atmosphere (moisture and oxygen). (a) halide/phase segregation, (b) formation of hydrates, crystal decomposition (c) releasing volatile molecules methylamine (MA), I2, NH3, and HI or (d) forming precipitates (Pb0, I2, etc.), and (e) morphology changes [44].

Table 2.1: Summary of some device architectures and theirs stability for PSCs [39]

Device Structure	Stability/h	Temp.	Atmosphere
TiO ₂ /CH ₃ NH ₃ PbI ₃ -liquid electrolyte/Pt	0.17	RT	Air
TiO ₂ /CH ₃ NH ₃ PbI ₃ /spiro-MeOTAD/Au	500	RT	Air
TiO ₂ /CH ₃ NH ₃ PbI ₃ /spiro-MeOTAD/Au	500	45 °C	Air
Al ₂ O ₃ /CH ₃ NH ₃ PbI ₂ Cl ₂ /spiro-MeOTAD/Au	1000	40 °C	N ₂ atmosphere
TiO ₂ /CH ₃ NH ₃ PbI ₃ /PDPPBTE/Au	1000	RT	Air
ZrO ₂ /CH ₃ NH ₃ PbI ₃ /C	1000	RT	Air
M-TiO ₂ /CH ₃ NH ₃ PbI ₃ /C	2000	RT	Air

2.2.1 Environmental Degradation

2.2.1.1 Humidity and Oxygen

External environmental conditions, such as moisture and oxygen, pose significant challenges to the long-term stability of materials, including photovoltaic (PV) components. The risks of corrosion and oxidation must be considered when designing stable materials for PV technologies. Metal-organic halide perovskites (MOHPs), a key component in perovskite solar cells (PSCs), are particularly sensitive to these environmental stressors [44]. When perovskites are exposed to moisture, water molecules penetrate the polycrystalline film, typically through surface defects and grain boundaries. This results in reversible or irreversible

reactions, such as the formation of hydrates through hydrogen bonding, which destabilize the crystal structure, leading to loss of optoelectronic properties [46]. While reversible hydration can restore the original perovskite structure, irreversible degradation occurs when new grain boundaries form or when reaction products like lead iodide (PbI2) precipitate [47]. Similarly, oxygen exposure, when combined with light, accelerates degradation in perovskite films, especially affecting charge transport layers that interact with oxygen [42]. This underscores the importance of understanding the degradation mechanisms of perovskite materials under varying environmental conditions.

Oxidation-induced degradation also impacts the charge transport layers of PSCs, which typically consist of organic small molecules or polymers, and sometimes inorganic materials such as metal oxides. Organic materials like spiro-OMeTAD require oxidation to enhance their conductivity, which can be beneficial to device performance under controlled conditions [42]. However, oxidative degradation of these materials can lower carrier mobility, affecting device efficiency. Metal oxide transport layers, such as TiO2, are prone to oxygen-induced degradation, especially when exposed to UV light, which can generate reactive oxygen species that catalyze the decomposition of nearby materials, including the perovskite absorber layer itself [42, 48]. In the presence of both oxygen and light, perovskite materials degrade more rapidly, underscoring the need for careful consideration of both environmental and packaging factors to ensure the long-term stability and performance of perovskite solar cells [48,49]. Figure 2.3 is a simple illustration for degradation by oxidation and humidity [50].

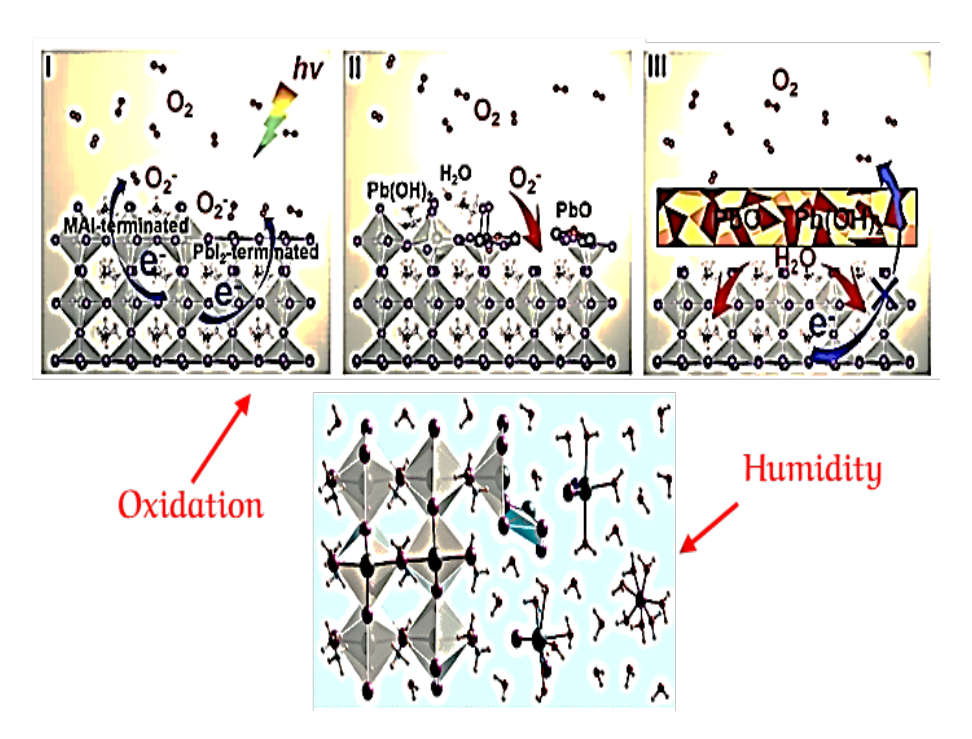


Figure 2.3: Degradation of MAPbI3 by oxidation and humidity [50].

2.2.1.2 Light Induced Degradation

The stability of organic–inorganic hybrid (OInH) perovskite solar cells under light exposure is a critical factor for their longevity and efficiency. One of the primary causes of degradation in OInH-PSCs is ultraviolet (UV) light, which can instigate several degradation mechanisms that compromise device performance over time [39, 42–45] (see Figure 2.4). UV-induced degradation processes are associated with electron recombination, which creates localized trapping sites, reduces the depletion layer, and alters TiO_2 band excitation, leading to oxidation of halide ions in the perovskite or hole transport material (HTM) [39]. Other contributing factors, such as oxygen, heat, and visible light, can also drive degradation, yet UV light remains one of the dominant sources, underscoring the need for stable UV-absorbing materials that protect both the absorber and substrate [42].

Degradation mechanisms under UV illumination can be further analyzed through the surface chemistry of TiO_2 . Mesoporous TiO_2 possesses surface defects (e.g., Ti^{3+}) that serve as electron traps. These electrons bind to O_2 molecules, forming oxygen–titanium complexes and causing degradation by adsorbing oxygen on TiO_2 surfaces [43]. During bandgap excitation, holes recombine with these trapped electrons, desorbing oxygen and creating new traps. Over time, this can lead to oxidation and halogen elimination, resulting in the breakdown of the perovskite into dihalogens (e.g., I_2 , Br_2 , Cl_2) and other byproducts. For instance, the light-induced degradation of MAPbI₃ may yield PbI₂, marking an irreversible breakdown that limits the material's lifespan [39, 42–45].

To achieve durable photovoltaic devices, the perovskite absorber and charge transport layers must demonstrate intrinsic stability under light. Although encapsulated MAPbI $_3$ films exposed to prolonged simulated sunlight have shown no visible decomposition, other studies report that perovskite layers experience complex photoinduced changes, such as halide segregation, ion migration, and compositional degradation [44]. Despite these challenges, certain photoinduced changes can benefit device performance by enhancing properties like conductivity and open-circuit voltage. For instance, CIGS solar cells demonstrate metastable defect reactions under light soaking that increase their efficiency—a phenomenon that has also been observed in perovskite cells [42].

In addition to the absorber, the stability of charge transport layers under illumination is crucial for device performance. Organic transport materials, while relatively robust in inert environments, can degrade through radical formation and bond cleavage upon excitation. Fullerenes, often used as electron transport layers, are known to undergo photodimerization under light, though they retain stability under prolonged illumination in certain configurations. In photodimerization, the light provides energy that enables two adjacent molecules to form covalent bonds, resulting in a single dimeric molecule. In contrast, TiO₂ layers are highly susceptible to UV-induced degradation, leading to rapid trap-induced recombination and performance loss, even under inert conditions. Solutions to this issue include the use of

alternative materials like fullerene or tin oxide electron transport layers or applying UV filters, which can significantly enhance stability by preventing photoexcitation of TiO₂ [39,42].

Finally, light-induced effects on ion distribution within metal halide perovskites have been identified as a critical factor influencing performance. Studies show that exposure to light can activate iodide migration in perovskite films, potentially affecting the film's photoluminescence and open-circuit voltage. This photobrightening effect is often related to ion diffusion and the presence of point defects such as halide vacancies. When combined with oxygen and humidity, light exposure can also lead to surface passivation effects, enhancing photoluminescence and stability. However, this delicate balance between passivation and degradation suggests that non-penetrative passivation techniques may offer better long-term stability without risking further damage to the perovskite structure [39, 42, 44].

These insights underscore the complexity of managing degradation pathways in OInH-PSCs and the importance of choosing materials and structures that support long-term stability.

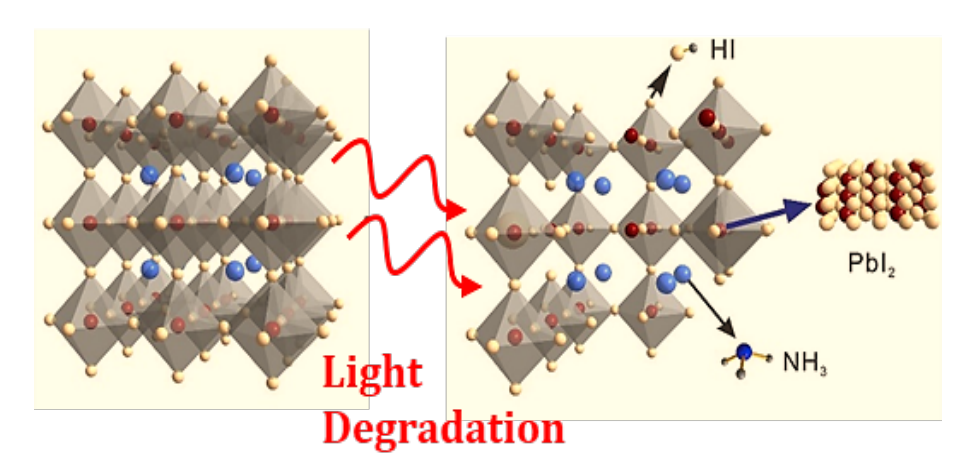


Figure 2.4: light-induced degradation mechanism in MAPbI3 [51].

2.2.1.3 Temperature Induced Degradation

Increasing the annealing temperature from 40° C to 100° C for 30 minutes improved the performance of a perovskite QD-sensitized TiO₂ film. However, further increasing the temperature from 100° C to 160° C resulted in a decrease in efficiency, from 4.73% to 3.71%, primarily due to a reduction in photocurrent density. External quantum efficiency (EQE) spectra revealed that the reduced photocurrent density at higher temperatures (160° C) is attributed to a significant loss in EQE in the long wavelength region (above 500 nm) [39,42,43].

Both the annealing temperature and the storage temperature are crucial parameters influencing the degradation of OInH-PSC devices. Although no specific literature reports on this, it is evident that OInH-PSC devices must undergo tests such as thermal stress tests at 80°C for 1000 hours to ensure their viability for practical applications. In operation, the de-

vice temperature could exceed 80°C, particularly due to continuous illumination from a solar simulator (e.g., 0.1 W cm^{-2} sunlight), which heats the sample film [39, 42, 43].

Apart from light, moisture, and oxygen-induced degradation, OInH-perovskites also experience thermal degradation. This degradation can lead to the formation of PbI_2 and organic salt by-products. The thermal stability of $CH_3NH_3PbI_3$ is confirmed to exceed 300°C, yet recent studies have shown that organic decomposition temperatures can be as low as 140°C. Decomposition of methylammonium iodide can generate HI and CH_3NH_2 , which could remain within the perovskite network and interfere with photovoltaic processes. Furthermore, the presence of degradation products like PbI_2 poses another problem. PbI_2 has poor optical properties, weak light absorption, and a higher bandgap, all of which contribute to device degradation [39, 42, 43].

The mechanisms behind the expansion and compression of the perovskite structure at different temperatures remain unclear. High temperatures can also cause issues such as interlayer diffusion, metal counter-electrode diffusion, ohmic contact degradation, and overall device architecture degradation. As a result, new OInH-perovskites with enhanced intrinsic temperature resistance are better suited for future development in OInH-PSC-based photovoltaic technologies. For example, FAPbI₃ has been shown to have better temperature resistance than MAPbI₃ [39, 42, 43]. A Schematic illustration of thermal degradation processes in MAPbI₃ was presented in Figure 2.5 [52].

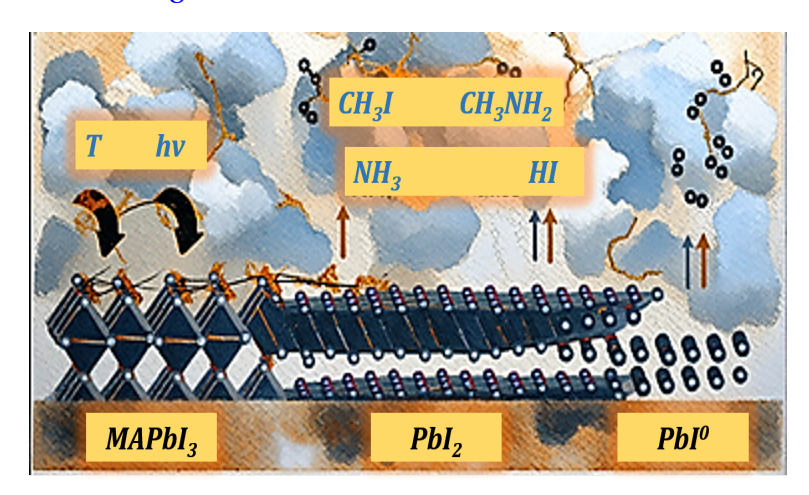


Figure 2.5: Schematic illustration of thermal degradation processes in MAPbI3 [52].

Thermal Stability in an Inert Atmosphere

The thermal stability of perovskite solar cells and understanding how stability scales with temperature is critical for several reasons: (1) annealing is required to form many perovskite films and contacts, (2) module encapsulation processes often exceed 140°C for short periods, (3) solar cells routinely reach 65°C in hot climates, and (4) testing at high temperatures accelerates chemical reactions and degradation processes that could take years in the field [39, 42, 43].

Perovskite Structural Stability (Phase Stability)

A major concern with OInH- perovskites is their ability to maintain the desired photoactive structure during processing, encapsulation, and use, without reverting to a non-photoactive phase or segregating into multiple phases. The structural stability of ABX_3 perovskites is often described using the Goldschmidt tolerance factor, t (see eq. (1.1)), where perovskite structures are stable when t is between 0.71 and 1. This suggests that FA cations are too large for the perovskite structure, while Cs cations are too small, causing them to form the non-photoactive yellow delta phase at room temperature. In contrast, methylammonium (MA)-based perovskites have a tolerance factor of 0.91, allowing them to exist in a black, photoactive tetragonal or cubic structure across operational temperatures ranging from - 15°C to 65°C [42–44].

Although pure FAPbI₃ can be quenched (cooling the material at a rapid rate) into a metastable black perovskite phase at room temperature, it typically reverts to the non-photoactive delta phase after several hours or days. Similarly, CsPbI₃ does not form a metastable black phase and instead reverts to the yellow delta phase. However, limiting crystal size in quantum-dot films or adding surface additives can stabilize the metastable alpha phase of CsPbI₃ at room temperature. Thus, MAPbI₃ compounds are more structurally stable than FAPbI₃ and CsPbI₃, though they are less resistant to thermal decomposition. This drives the push to stabilize alternative perovskite compounds through mixing at the A-site, B-site, or X-site. These mixtures may provide structurally stable perovskite phases with the added benefit of tunable bandgaps for improved optoelectronic properties [42–44].

The A-site cation has the most significant impact on thermal stability due to its effect on the interactions between the lead-halide octahedra and the higher volatilities of organic compounds compared to inorganic salts. FAMA, FACs, and FAMACs compounds are structurally stable across a wide alloying range at room temperature and exhibit improved photovoltaic performance compared to single-cation perovskites. A recent innovation has been the inclusion of rubidium in both triple-cation and quadruple-cation perovskites. A subsequent rubidium-free composition, $Rb_{0.05}Cs_{0.1}FA_{0.85}PbI_3$, achieved efficiencies above 20% and excellent stability under illumination in nitrogen. The stability of rubidium-containing compounds is attributed to increased entropy of mixing and the elimination of the volatile MA cation. However, the exact mechanisms of rubidium incorporation are still under investigation, and some studies suggest rubidium-containing compounds may form non-photoactive secondary phases [42–44].

Thermal Stress

Temperature is an unavoidable stressor in photovoltaic applications, as sunlight radiation includes infrared heating energy. International standards typically consider heating between 60°C and 85°C as normal during operation, but devices must withstand even higher temper-

atures, particularly in hot climates or when integrated into technologies that generate additional heat during operation [43,44].

There is consensus in the literature that PbI_2 is the thermal degradation product of MAP bI_3 . However, the degradation path depends on the stress level and measurement environment. An intermediate PbI_2 -like structure forms first and serves as a precursor to PbI_2 formation, similar to how this intermediate structure facilitates MAI intercalation. Thus, thermal degradation is often referred to as the reverse of perovskite formation. The breaking of Pb-I-Pb bonds in the [001] direction creates channels that allow species such as metallic lead (Pb^0), iodide (I^-), $CH_3NH_3^+$, HI, and CH_3NH_2 to migrate within the material. This migration facilitates the formation of intermediate structures or even amorphization, which ultimately leads to the more stable PbI_2 [43, 44].

At low thermal stress (<130°C), this process occurs as a layer-by-layer transformation, beginning with the formation of dangling bonds on the surface of perovskite crystallites. This layer-by-layer decomposition can be slowed by passivating the dangling bonds or by improving crystal integrity at surfaces and grain boundaries. At higher thermal stress (130–150°C), the process becomes faster and may bypass intermediate states, leading directly to an amorphous phase before finally forming PbI₂. Degradation of MAPbI₃ occurs at all elevated temperatures, but some of the stress may be reversible until the final formation of Pb [43, 44].

2.2.2 Structural Instability and Ion Migration

2.2.2.1 Hole Transport Layer

Hole transporting layers such as spiro-MeOTAD, PEDOT:PSS, and other polymers, as well as inorganic materials, are significantly more stable than liquid electrolytes. However, devices based on these materials are also susceptible to chemical degradation, during which photooxidation processes and hole–electron pair recombination may occur. This section focuses on the most commonly used HTMs, spiro-MeOTAD and PEDOT:PSS [39].

Spiro-MeOTAD

Spiro-MeOTAD is widely used in OInH-PSCs for hole transporting purposes. It is coated beneath the counter electrode and can easily be exposed to the atmosphere, leading to degradation due to air exposure, continuous light irradiation, elevated temperature, and dust. Qi and colleagues investigated the causes of degradation in OInH-PSCs using spiro-MeOTAD as the hole selective material [53, 54]. Due to its amorphous properties, spiro-MeOTAD allows small molecular species from the air to spread and pass through miniscule pinholes in the material, which are too small to be seen with an optical microscope [53, 54]. The decline in Jsc and FF is possibly caused by OInH-perovskite layer degradation, which can be due to air molecules $(O_2, H_2O, \text{ etc.})$ migrating and interacting with OInH-perovskite via the pinholes

and/or outdiffusion of mobile ions in the OInH-perovskite film via the pinholes in the spin-coated spiro-MeOTAD [53]. These pinholes create pathways for foreign molecules such as water and other gases to diffuse through the thin film, leading to impurities in the solar cells and a drop in efficiency.

The presence of oxidized spiro-MeOTAD is required for OInH-PSCs, but oxygen reduction reactions might also occur, changing the oxidized spiro-MeOTAD concentration and device characteristics during operation. For future development of devices with long-term stability, it is important to exclude oxygen reduction. Further work is needed to determine if this can be achieved by sealing the devices after preparation under ambient atmosphere or by fabricating and sealing the devices to exclude oxygen and moisture.

PEDOT:PSS

Poly(ethylenedioxythiophene):poly(styrene sulfonic acid) (PEDOT:PSS) is generally used in the form of a water solution/suspension for solar cells as the HTM [55] and has recently been used in inverted OInH-PSCs as a hole selective material [56,57]. The hygroscopic property of PEDOT:PSS destabilizes the interface and results in device deterioration. Compared to PEDOT, the amount of PSS usually dominates in the polymer mixture, and the diffusion of PSS into other layers can occur, possibly resulting in degradation. For instance, PSS may undergo oxido-de-sulfonato-substitution forming phenolate, which can then react with PSS, forming two PSS chains linked via a sulfonic ester group [58]. Additionally, corrosion is enhanced not only in connection with low work function metals such as Al or Ca used as a counter electrode but also with an ITO electrode [59].

Dauskardt and coworkers verified how the hygroscopic properties and poor adhesion of PEDOT:PSS onto the active layer cause a general loss of device performance in roll-to-roll processed normal geometry organic photovoltaic devices. The objective was to show that thermomechanical stress in a real-life device would suffer [60].

2.2.2.2 Metal Counter Electrode

Gold, silver, and aluminum metals are commonly used as counter electrode materials in mesoporous, planar, and inverted OInH-PSCs [56]. The drawbacks of silver include its corrosion in contact with halide ions from the OInH-perovskite light absorber, forming silver halides such as AgCl in humid environments, and short circuits or shunting paths with mesoporous TiO₂, leading to device degradation [39] (Figure 2.6 [61]). The high cost of a Au electrode also requires a high-vacuum evaporation technique, limiting its future application. Low-cost carbon may be an ideal material to substitute Au as a back contact with OInH-perovskite heterojunction (HJ) solar cells at low temperature, because its function is similar to that of Au [39].

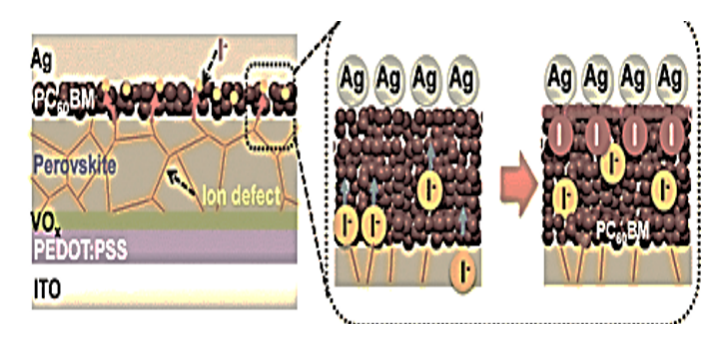


Figure 2.6: Schematic illustration of metal counter electrode degradation processes in OInH-PSCs [61].

2.2.2.3 Effect of Interface

Degradation in OInH-PSC devices is primarily caused by moisture ingress, high temperatures, and UV exposure. However, significant degradation is still observed even in well-encapsulated devices or when tested in inert environments, suggesting that intrinsic factors within the device also play a role. One such factor is the unstable electronic structure at the organic/cathode interface, which results from the gradual diffusion of metal into the organic films. A similar degradation process occurs at the ITO anode/organic interface, where reactive oxygen species generated by UV treatment of the ITO substrate gradually break down the organic layer. Other degradation mechanisms may be linked to the organic/electrode interface, as well as time-dependent chemical reactions at the donor/acceptor interface, leading to device deterioration. Additionally, the spatial isolation of organic films from electrodes and the reduction of the energetic transport barrier may contribute to this degradation [39].

Ion Migration

Electromigration rates are influenced by factors such as temperature, electric field, and illumination. Four essential conditions for electromigration are: the presence of mobile ions, a voltage gradient, a continuous supply of moisture, and soluble ions. Silver, with its low activation energy, is particularly prone to migration. Electromigration severity increases with the applied potential gradient and the time taken for silver to reach active materials. Silver migration can cause short circuits and device failure, particularly in humid conditions. In Pb-based perovskite materials (ABX₃), cations at both the A-site and B-site can be replaced by other cations, depending on their valence and ionic radius. Since the ionic radius of Ag^+ is similar to that of Pb^{2+} , it may replace Pb^{2+} in MAPbX₃ OInH-perovskite materials, though this has not yet been experimentally confirmed. This substitution could also contribute to structural distortions in the MAPbX₃ layer during device operation. The low melting point of silver may explain the structural changes and abnormal grain growth near the interface in OInH-perovskites [53,54].

Reactivity

Chemical reactions and interdiffusion at the interface can significantly affect the overall stability of the device. Interface instability is an area that has been relatively underexplored in OInH-PSC devices. Potential sources of degradation at the interface include: (i) corrosion of silver leading to the formation of silver halides; (ii) the creation of shunting paths between silver connections and mesoporous TiO2 in the absence of oxygen; (iii) photo-oxidation of the HTM organic materials, which degrades electron/hole transport properties and reduces photovoltaic stability; (iv) decomposition of the OInH-perovskite at the TiO₂/CH₃NH₃PbI₃ interface upon light exposure, as TiO₂ has a strong ability to extract electrons from iodide (I⁻); and (v) the formation of metal oxides, which can ultimately lead to device failure. Docampo and Snaith demonstrated that in the absence of oxygen, silver contacts can form shunting paths with mesoporous TiO₂, creating a Schottky barrier. Further, Snaith and colleagues showed that metal migration through the HTM layer is partially responsible for rapid device degradation. They found that using an insulating mesoporous "buffer layer" of Al₂O₃ beneath the HTM prevents this migration, while also allowing for precise control over HTM thickness. This approach helps maintain device stability, even after 350 hours of operation [62, 63].

2.2.2.4 Bias Voltage-Induced Degradation

In commercial solar panels, photovoltaic cells are typically connected in series to increase the output voltage. These panels generally operate close to their maximum power point (MPP), provided that all individual cells have similar efficiencies and receive uniform illumination, resulting in comparable maximum power point voltages (VMPP). VMPP is the voltage near the open-circuit voltage (V_{oc}) where the product of voltage and current (power) is maximized. However, when electrical charges accumulate and are not extracted, they can induce instabilities. For instance, in the presence of O_2 , free electrons may form reactive superoxide species (O_2^-), which degrade the perovskite material [44]. When panels experience partial or total shading, shaded cells may operate in reverse bias to maintain current flow. Reverse bias conditions can create high electric fields that trigger ion drift, compromising perovskite stability. Eventually, such reverse bias conditions can cause breakdown voltages that lead to device failure [44].

Several in situ studies have investigated the effects of bias voltage stress on the stability of PSC devices or thin films with symmetric electrodes. Li et al. performed an in situ photoluminescence (PL) study to quantitatively measure the rate of ionic motion. A bias of approximately 2 x 10^4 V m⁻¹ was applied between two parallel electrodes separated by 150 μ m, resulting in a darkening of the PL intensity that spread from the positive to the negative electrode over time. By tracking the simultaneous current loss under the applied bias, the authors calculated the ion migration speed to be $10~\mu$ m/s. The defects generated by this

migration significantly limited the radiative recombination in the film between the lateral contacts [64].

Advanced transmission electron microscopy (TEM) techniques have also been employed to visualize the degradation of MAPbI₃ under bias conditions. Jeangros et al. concluded that the primary contributors to bias-induced degradation of MAPbI₃ solar cells were the formation of PbI₂ nanoparticles and voids, migration of iodide into the hole transport layer (HTL), and the volatilization of iodide and organic molecules under a 6 V forward bias, as observed through STEM and high-angle annular dark-field (HAADF) imaging. They found that degradation predominantly occurred at the MAPbI₃/HTL interface, likely due to energy dissipation processes that depend on the polarity of the layers at their intersection [65].

In another study, Kim et al. used a TEM stage capable of both heating and applying electrical bias to observe the amorphization of a 300 nm lamella (prepared by focused ion beam, FIB) of a complete PSC suspended between two gold electrodes during the first 5 minutes of a 1 V forward bias. Using high-resolution TEM (HRTEM), they observed that under a +1 V bias, the perovskite grains gradually lost their crystallinity, as though the crystalline layer was dissolving. The PbI₂ phase present did not exhibit crystallinity loss, and no morphological changes were noted, though changes were visible at the lattice spacing resolution. To rule out beam damage, these HRTEM results were cross-verified with selected area electron diffraction (SAED) before and after 5 minutes of biasing at 1 V. SAED revealed clear amorphous ring formation after the biasing. Interestingly, the device fully recovered after resting in the dark, and complete recovery occurred after heating to 50°C for just 3 hours. The authors proposed a mechanism in which halide ion migration and defect generation lead to crystal collapse as the Pb plane decomposes. These findings have significantly advanced the understanding of perovskite degradation under bias conditions and suggest that mild elevated temperatures could be used to heal bias-induced damage [66]. In Figure 2.7 [67]) was presented a schematic illustration of bias voltage-induced degradation.

2.2.3 Lead Leaching Toxicity

High-performance photovoltaic solar cells (PSCs) currently use Pb-based perovskites as the light-absorbing layer. However, these perovskites are unstable and can be easily decomposed by water to release PbI₂, which is 14 orders of magnitude more water soluble than toxic cadmium in CdTe cells. Exposure to Pb can lead to serious cardiovascular, developmental, neurological, and reproductive diseases, making it crucial to assess the environmental impact before commercializing PSCs [3].

Hailegnaw et al. studied the possible environmental effects of PSCs, evaluating the worst-case scenario where the Pb-based perovskites were completely exposed to rain [68]. The pollution scenario introduced by perovskites is classified as "low levels" of contamination (around 400 ppm), but any release into the natural environment should be avoided or mini-

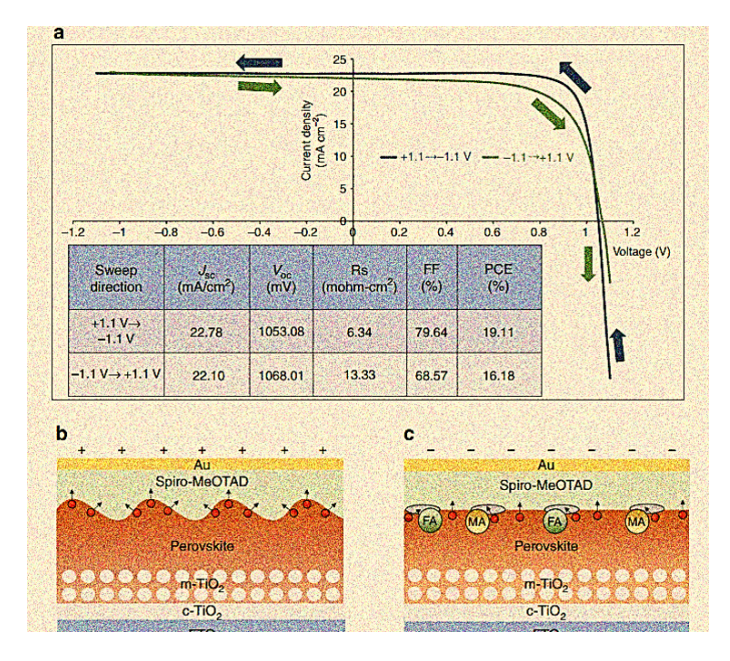


Figure 2.7: Illustration of an example of bias voltage-induced degradation in OInH-PSCs [67].

mized [68].

Numerous attempts have been made to develop Pb-free light absorbers for PSCs, with Sn being considered the best candidate to replace Pb. The perovskite crystal structure of MASnI $_3$ has been extensively investigated, with solar cells using MASnI $_3$ perovskite displaying efficiencies of 5.23% and 6.4%, respectively. The bandgap of MASnI $_3$ can be tuned from 1.30 to 2.15 eV by partially substituting I with Br. The V_{oc} of PSCs increased from 0.68 to 0.88 V as E_g increased, and the best-performing PSCs with a PCE of 5.73% were obtained [3].

The room-temperature crystallization features help in cost control for commercialization due to the simplified process. However, the fast crystallization of Sn-based perovskites acts as an impediment to the formation of uniform films, as partial surface coverage can introduce a high charge recombination pathway between ETL and HTM due to their direct contact. High-quality PSCs with Sn-free perovskites could potentially reduce the environmental impact of Pb and improve the performance of solar cells [3].

It is true that fully Pb-based PSCs have achieved a maximum power conversion efficiency (PCE) of approximately 9%. However, when transitioning to mixed Pb-Sn perovskites, significantly higher PCEs have been reported, with values reaching around 20% and even surpassing this threshold. While the prospect of fully replacing Pb with Sn in perovskite solar cells offers an exciting route toward enhancing sustainability and reducing toxicity, challenges remain in optimizing the material properties of Sn-based perovskites. Nonetheless, the promising results from mixed Pb-Sn systems suggest that further advances could make the complete substitution of Pb by Sn a viable and effective solution for next-generation solar technologies.

2.3 Alternative Stable Materials for Perovskites

The Goldschmidt tolerance factor (t) is a dimensionless parameter used to predict the stability and geometrical distortion of perovskite structures (ABX_3) based on the ionic sizes of the cations and anions. For a stable 3D structure, t should be within the range of 0.80 < t < 1.0. Values outside this range lead to non-perovskite structures. The tolerance factor also helps predict the crystal phase: cubic ($t \approx 1$), tetragonal (0.9 < t < 1.0), or orthorhombic (0.8 < t < 0.9). Phase stability is crucial for material performance, as unstable phases, like the d-phase of FAPbI₃, can impair charge transport. Compositional engineering can adjust tolerance factors to enhance phase stability and improve the performance and stability of perovskites, especially in photovoltaic applications (Figure 2.8 [69]).

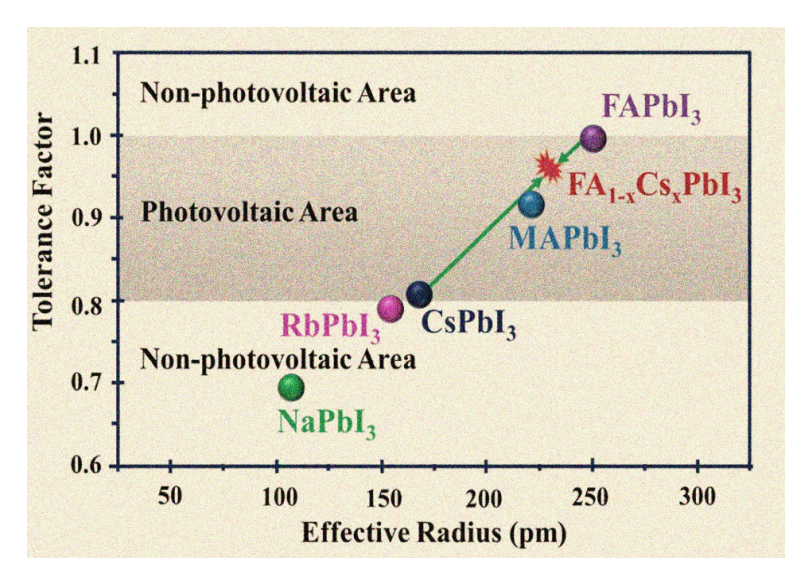


Figure 2.8: Relation between the perovskite structure and the Goldschmidt tolerance factor [69].

2.3.1 Mixed-Halide Perovskites

The research field has expanded to include complex halide perovskite stoichiometries, providing greater stability than simple MAPb I_3 . However, the issue of halide segregation has been a concern since 2015 [70], with the Hoke effect revealing the formation of an I-rich phase on MAPb (Br_xI_{1-x}) $_3$. This has implications for device stability, as it reduces the maximum achievable voltage of mixed-halide-based solar cells [71]. The study of the mechanism behind halide segregation has largely focused on the A-site cation composition of the perovskite. The number of carriers recombining via trap states is believed to be the main driving force. Mixed-halides perovskites dominate the research in solar cells due to their promising device performance. However, they also suffer from unique phase segregation behavior [72], which is detrimental to their device stability. Phase segregation is closely related to defects in the perovskite, with a high concentration of halide defects usually having stronger phase

segregation behavior. Several effective approaches have been developed to prevent phase segregation, such as Duong et al. applying a stoichiometric engineering method to suppress phase segregation in mixed-halides perovskite films, Hu et al. engineering perovskite crystallinity and grain size, and Abdi-Jalebi et al. using potassium iodide to passivate defects and grain boundaries [73].

2.4 Engineering Techniques for Stability Enhancement

Various methods has been performed to enhance the moisture stability of perovskites, including incorporating Br into MAPbI₃, incorporating an inorganic cation at A site, and incorporating 5% Rb into FAPbI₃. Low-dimensional perovskites, such as quasi 2D-Ruddlesdon Popper Perovskites, are known for their high stability and improved photovoltaic properties [74]. These perovskites can be used individually or combined with 3D perovskites for light harvesting (Figure 2.9 [75]). They are represented by the general formula $(R - NH_3)_2 M_{n-1} A_n X 3_{n+1}$ where $(M_{n-1}A_n X 3_{n+1})$ stands for conductive layers of parent 3D Perovskites like MA PbI₃, FAPbI₃, etc and R-NH₃ for a large aliphatic or aromatic ammonium spacer cation like Phenylethylamine (PEA), Butyl amine (BA), etc.

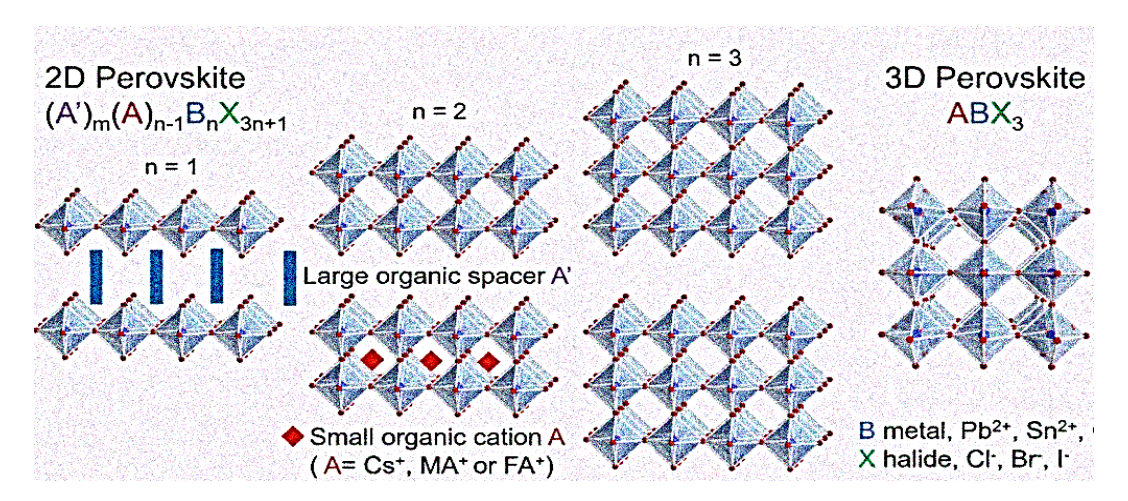


Figure 2.9: Structure illustration of 2D, Quasi 2D, and 3D-Perovskites [75]

Additive assisted treatment is another effective way to enhance the stability of perovskites. The addition of acetic acid as an antisolvent reduces the perovskite film roughness and passivates the defect state. The presence of a carbonyl group in acetic acid helps passivate the defect states [76]. Perovskite-polymer composite films have been studied to improve efficiency and reduce degradation [77]. A surface blocking layer, Sb_2S_3 , between the ETL and the absorber layer had significantly enhanced PCE and J_{sc} stability against light exposure in $TiO_2 Sb_2S_3 CH_3NH_3PbI_3 PSC$ [78, 79]. In addition, a thin conductive reduced graphene oxide (rGO) spacer layer was introduced between the HTL and the Au back contact to overcome the instability of PSCs [78].

2.4.1 Encapsulation Technologies

The commercialization of PSCs requires encapsulation to protect them. Encapsulants must be easy to deposit, dimensionally stable, and low-cost. Mechanical behavior and light transmission capacity are crucial factors. Oxygen transmission rate and water vapor transmission rate are important, with values in the range of 10^{-6} - 10^{-4} cm³ 1 atm respectively. The degradation rate (DR) of PSC is critical for its long-term stability. Tests like the Calcium test and RGB color measurement test evaluate the efficiency of encapsulants as moisture barriers. Popular methods include glass-glass encapsulation, common epoxy resin, Cu C-tape, thin-film encapsulation (TFE), ultrathin plasma polymer, and solvent-free and low temperature melting encapsulation using paraffin. Studies show that PSCs with SiO₂ layer, UV-curable epoxy resin, and desiccant sheet are stable [78, 80]. The decrease in PCE value of PSC is related to WVTR (water vapor transmission rate) value and the relation is given by [80]:

$$DR(d\%) = \frac{DR_{max}.WVRT^n}{(WVTR_{50})^n + WVTR^n}$$
(2.1)

where DR stands for degradation rate of PSC, DR_{max} is the maximum degradation rate, WVTR₅₀ is the WVTR value when DR is 50% of DR_{max} and n is the coefficient of the Hill function that controls the sigmoidicity (the S shape) of the curve.

2.4.2 Interfacial Engineering for efficiency and stability

Interfacial engineering is a crucial strategy for improving the efficiency and stability of Photovoltaic Cells (PSCs). Materials for interfacial engineering include polymers, ligands (a molecule that binds to another (usually larger) molecule), small functional molecules, low-dimensional (low-D) perovskites, and perovskite quantum dots (QDs). Polymer materials act as insulation components and defect passivators in perovskite materials, preventing extrinsic degradation factors. Perovskite surface defects can be passedivated by forming strong bonds with ligands, protecting against degradation [81]. The bandgap and redox potential of small molecules can be easily tuned. The low crystallinity of small molecules allows for better electronic contact with the perovskite layer, reducing interface defects. Low-D (2D) perovskites protect against extrinsic degradation factors and prevent the decomposition of 3D perovskite absorbers due to higher formation energy. This higher energy means that 2D perovskites are more stable in terms of their chemical structure. As a result, they are less likely to decompose or be affected by external factors. As results, interfacial engineering can significantly improve the light and thermal stability of PSCs by using all these 2D materials [82].

Chapter 3

Defects in Perovskite Solar Cells and Passivation Strategies

3.1 Introduction

Any displacement of atoms from their designated positions in a periodic crystal lattice results in the formation of defects. Polycrystalline perovskite films typically exhibit a high defect density due to the solution processing method and low-temperature annealing. The stoichiometry of the material plays a significant role in influencing defect formation in perovskites [43]. The presence of Frenkel and Schottky defects in MAPbI₃ at thermal equilibrium has already been confirmed [43]. Not all defects are detrimental. Defect or trap states located above the conduction band or below the valence band generally have no harmful effect. However, defect states within the bands can act as trap states. Shallow trap states can impede charge carrier movement by trapping and releasing them, while deep trap states disrupt the de-trapping process and contribute to non-radiative recombination. Although perovskites are recognized for their defect-tolerant nature, the presence of certain defects still limits their progress toward commercialization [43].

Non-radiative charge recombination typically occurs through deep level traps or Auger recombination, but this is relatively weak in perovskite solar cells under 1-sun illumination. When imperfections create deep level traps, they trap electrons or holes, which cannot escape thermal activation and are annihilated with an oppositely charged carrier through non-radiative recombination, as described by the Shockley–Read–Hall (SRH) theory [83, 84].

There are four main types of imperfections in Organic-Inorganic Hybrid (O-InH) materials: intrinsic point defects, impurities, two-dimensional extended defects, and three-dimensional defects like lead clusters. These defects can lead to interesting applications, such as narrow-band photodetectors. However, most point defects with low formation energies result in shallow level traps, which can influence the photovoltaic performance of PSCs due to their ionic nature and high ion migration speed [83, 85, 86].

Various methods for passivating imperfections in PSCs have been developed to reduce non-radiative charge recombination and suppress ion migration. These methods include coordinate bonding, ionic bonding, and conversion of extended imperfections to wide bandgap materials [83].

3.2 Defects in MAPbI₃ Perovskite

Imperfections in Organic-Inorganic Hybrid Perovskite (O-InHP) films can affect photovoltaic parameters of perovskite solar cells (PSCs), such as open circuit voltage (V_{oc}), short-circuit current density (J_{sc}), fill factor (FF), and power conversion efficiency (PCE). The V_{oc} is extracted from the splitting of electron and hole quasi-Fermi levels. Non-radiative recombination processes decrease the steady-state charge density, reducing the splitting of quasi-Fermi levels, and consequently, the V_{oc} of solar cells also decreases. The dominant non-radiative recombination process occurs through the Shockley–Read–Hall (SRH) process due to the trapping effect of deep-level defects. Defect passivation in PSCs helps improve the interface between the perovskite layer and charge transport layers by reducing defects. This can lower the contact resistance at the interface, improve the morphology of the perovskite film (reducing pinholes and shunt paths), and lead to a higher fill factor in the solar cell, resulting in better overall efficiency [83, 87].

Figure 3.1 shows the primary imperfections on the surface or grain boundaries of perovskite crystals that may cause deep-level traps, such as undercoordinated halide ions, undercoordinated Pb²⁺ ions, lead clusters, and intrinsic point defects like Pb–I antisite defects (PbI₃⁻). These defects result from growth or processing conditions and can form shallow-level traps, such as I or MA vacancies in the bulk of the material. The required passivation of charged defects in perovskite solar cells is different from that in covalent-bond based semiconductors like silicon. Unique passivation methods, such as coordinate bonding or ionic bonding, can neutralize and deactivate deep-level traps resulting from charged defects [83, 88].

The defects located at the grain boundary and surface of perovskite determine their non-radiative recombination properties. The presence of higher defect density at the grain boundary was confirmed by De Quilettes et al., using microscale PL measurements [89]. High covalency of Pb^{2+} could induce the formation of Pb clusters, which form deep trap states between the valence band (VB) and conduction band (CB). In cases where the film is iodine-rich, such cluster formation will lead to a higher amount of radiative recombination. The layered structure of perovskite-based devices leads to further formation of defect states. The presence of defect states at the junction of the perovskite and carrier layer will complicate the process. At the heterojunction, minority carrier recombination might occur due to the misalignment between the band positions. Charged ionic defects will further cause bending in the band, as reported by De Quilettes et al. They observed slight upward bending of the TiO_2 band at

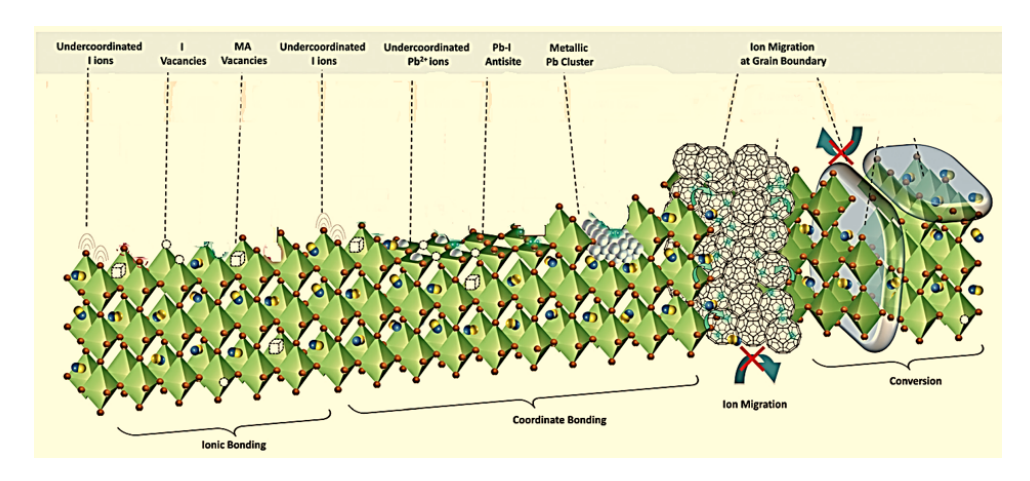


Figure 3.1: Imperfections in MAPbI₃ perovskite [83].

the perovskite boundary due to the accumulation of positive charge [43, 89].

Sharp-level traps originating from easily formed point defects are not detrimental to the photovoltaic performance of perovskite materials. However, the migration of such charged point defects under an electric field could cause the accumulation of charged ions at interfaces and unintentional doping effects. This can result in local band bending, current density–voltage hysteresis, phase segregation, and degradation of perovskites or metal electrodes [83, 90]. The dominant types of defects present in perovskite solar cells and their concentration are sensitive to the device fabrication processes and perovskite compositions. Perovskite precursors with non-stoichiometric PbI_2 and MAI ratios can induce extended defects with different types of defects and change the formation energy of point defects. Thermal annealing for longer periods or at higher temperatures can also result in the evaporation of organic cations and halides, leaving undercoordinated Pb^{2+} ions at the surface or forming PbI_2 [83, 90].

3.3 Defect Migration and Device Stability

The migration of defects under electric fields or illumination can cause device degradation and hysteresis phenomena during I–V measurements. The migration process is influenced by activation energies, which vary depending on the defect type and crystallographic direction [91]. The instability of the perovskite material MAPbI₃ is due to the smaller size of the MA-ion, which makes it adopt the less symmetrical tetragonal phase. Replacement of the MA-ions, either partially or fully, with a suitable ion size at the A site will change it toward a symmetrical lattice structure, which will improve stability. Iodine (I) is the most commonly used anion at the X site in perovskite materials. Under illumination, perovskites with I⁻ anions suffer from oxidation. Oxidation under light soaking can be reduced by mixing the halides. The bandgap of perovskite materials can be tuned by mixing halides, improving their stability, and accelerating charge transport [92, 93].

The device stability is also related to the lead (Pb) element at the B site in PSCs because of the soft nature of Pb–I bonding and Pb $^{2+}$ ions. Under illumination and/or at higher temperatures, the Pb $^{2+}$ ions tend to form Pb atoms and generate deep defect states, which leads to severe degradation. Replacing Pb $^{2+}$ ions at the B site with tin (Sn), either fully or partially, is one of the options for promoting the stability of PSC devices. The oxidation of Sn $^{2+}$ ions creates fewer grain boundary defects, improves the crystal quality, and generates a higher VOC, which enhances both the efficiency and stability of PSCs [92, 94, 95].

There are 12 possible native point defects in the MAPbI₃ structure, such as vacancies $(V_{MA}, V_{Pb}, \text{ and } V_I)$, interstitials $(MA_i, Pb_i, \text{ and } I_i)$, and anti-site occupations $(MA_{Pb}, MA_I, V_{Pb}, V_{P$ Pb_{MA} , Pb_{I} , I_{MA} , and I_{Pb}), which have been widely studied (Figure 3.2) [92, 96]. The common observation about point defects in MAPbI₃ is that defects with high energy can contribute to the formation of deep levels in the bandgap, and low-energy defects can contribute to the formation of shallow defect states. Deep-level point defects may not contribute a high density of non-radiative recombination centers. However, there is some variation in opinion about which point defects can contribute to deep levels, including I_{Pb} , I_{MA} , Pb_i , Pb_I , V_I , and Pb_{MA} . The defect formation energies of I_{MA} , Pb_I , and V_I are low enough to contribute a significant density of recombination centers. The formation energy of the Pb_I anti-site defect is low under iodine-rich conditions. The stable charge state of the Pb_I defect can make a transition at the Fermi level. Acceptors of shallow point defects are V_{Pb} , V_{MA} , MA_{Pb} , and I_i under some growth conditions with low formation energies, and MA_i , V_I , and MA_I are donors of shallow point defects. The donors and acceptors of shallow point defects can convert the MAPbI₃ material from p-type to n-type by intrinsic doping. Under stoichiometric growth conditions, the cation and anion vacancies may also dominate the defect formation. If the defect formation energies are low, unintentional doping can be minimized by compensating the vacancy with opposite charge carriers [92, 96].

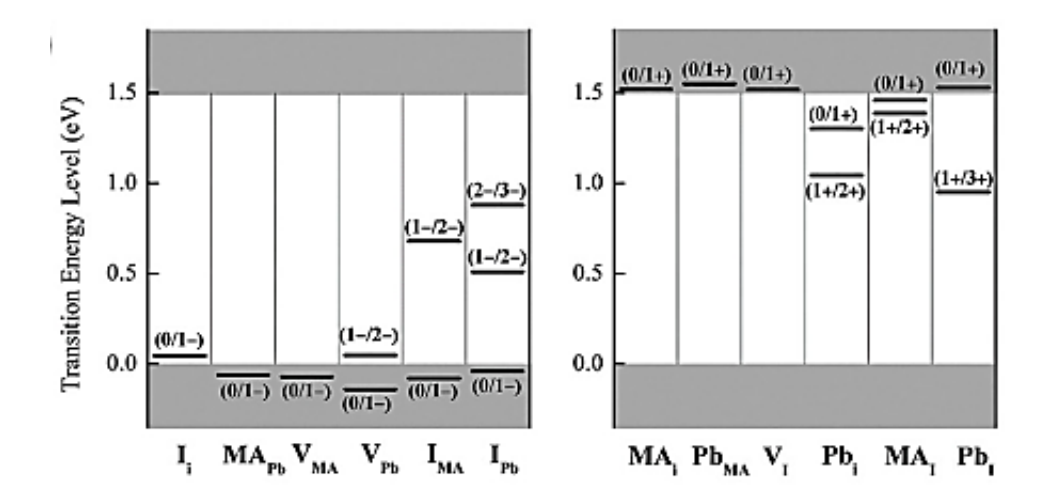


Figure 3.2: The transition energy levels of (a) intrinsic acceptors and (b) intrinsic donors in $MAPbI_3$ [83].

The four native defects, V_x , V_A , V_{Pb} , and Pb_i , in the perovskite crystal and the probable migration path for these four point defects were identified from the theoretical calculations, as shown in Figure 3.3 [92]. The proposed migration pathways are designed based on comparable migration energies for different defects with the displacement of the same chemical species. For example, MA-related defects (e.g., MA_{Pb} or MA_i) should display a similar activation energy as that calculated for V_{MA} . In fact, the activation energies of V_I and I_i are essentially the same [91, 92, 97].

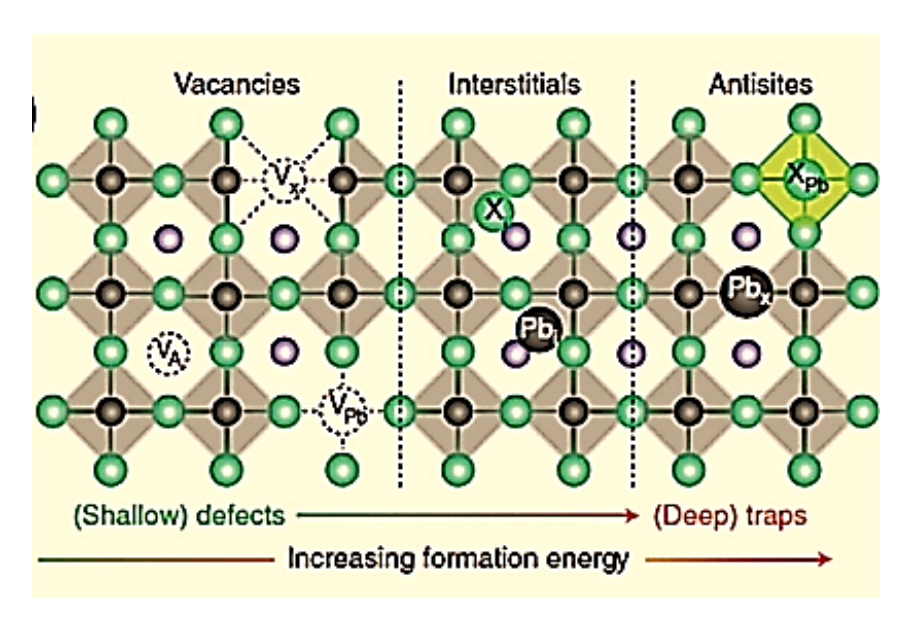


Figure 3.3: Schematic diagram of the MAPbI₃ perovskite structure and diffusion paths of the point defects [92].

The calculated activation energies of V_I and I_i are predicted to be 0.08 eV, which is sufficient for a full hop to take place in each crystallographic direction. In the absence of an external field, the charged defect can migrate forward or backward in any crystallographic direction. Under illumination within the operating conditions of PSCs, the charged defect (positive/negative) favors migration towards the side of the perovskite film that contacts the hole/electron transporting layer. The interstitial defects V_I and I_i can migrate towards the hole/electron contacts that are stabilized due to electrostatic interaction with the electrode. The defects can reach the electrode within tens of nanoseconds, which is much faster than the scanning rate in photovoltaic current–voltage (I–V) measurements [92, 97].

Figure 3.4 summarizes the generated probable defects, dipoles, and ions in perovskite solar cells under illumination, which can lead to device degradation and the hysteresis phenomenon during I–V measurements. During I–V measurements, concerning the scan rate/direction, various processes with respect to ion migration, ferroelectricity, charge trapping, and associated capacitive effects can occur simultaneously, leading to the resultant hysteresis. To overcome the hysteresis problem, as well as enhance the PSC efficiency and device stability, it is very important to control and minimize the various defects and ions in the device structure under illumination [92,97].

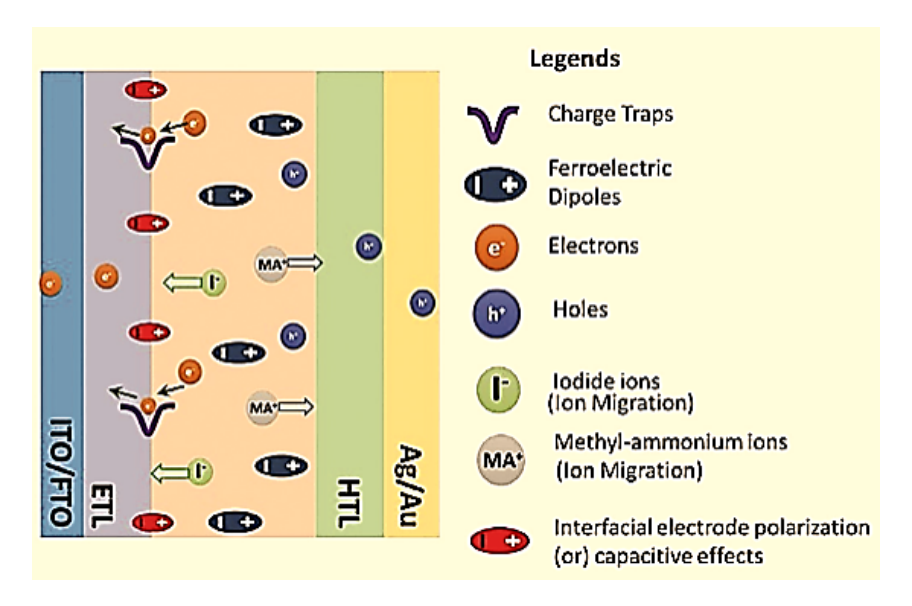


Figure 3.4: The various defects and ions generated under illumination in the perovskite solar cell device structure [92].

3.4 Passivation Strategies

Various passivation methods have been developed to reduce defect densities and enhance device performance. Techniques like coordinate bonding, ionic bonding, and material conversion are effective in passivating deep-level traps. *Coordinate bonding* involves the interaction between a Lewis base (electron donor) and a Lewis acid (electron acceptor). In perovskite materials, this technique can be used to stabilize the material and passivate defects. For example, crown ethers can be used as Lewis base modulators to coordinate with lead ions (Pb²⁺) in the perovskite structure. This coordination helps to stabilize the perovskite precursor and reduce the formation of harmful by-products, leading to improved defect passivation and overall performance. *Ionic bonding* involves the electrostatic attraction between positively and negatively charged ions. In perovskite solar cells, ionic liquids or other ionic compounds can be used to passivate defects. For instance, imidazolium-based ionic liquids can form strong ionic bonds with lead (Pb²⁺) and cesium (Cs⁺) ions, effectively reducing defects and improving the stability and efficiency of the perovskite material. This technique also helps in enhancing the hydrophobicity (chemical property of a molecule that is seemingly repelled from a mass of water) of the perovskite surface, making it more resistant to moisture. *Material conversion* involves transforming the perovskite material into a more stable or defect-free form. This can be achieved by carefully adjusting the composition of the perovskite material or by using alternative materials. For example, researchers have explored using tin (Sn) or germanium (Ge) instead of lead (Pb) to create less toxic and more environmentally friendly perovskite materials. Additionally, converting the perovskite material into a low-dimensional or stable form can help in reducing defects and improving the overall performance of the solar cells [83, 92].

3.4.1 Passivation of Defects in Perovskite Films

3.4.1.1 Ionic Compounds

Perovskite films have primary defects, including point defects with high formation energies and vacancy defects with low energies. Due to their ionic crystal structure, coordination compounds with charged ions form ion bonds for defect passivation [98].

Cations Organic-inorganic hybrid perovskite solar cells can be improved by using ion doping to passivate vacancy defects. Ions like cesium and rubidium can replace A-site ions in perovskites, making crystallization more stable and less susceptible to environmental influences [99]. Alkali metal ions like potassium, sodium, and lithium can also be used for defect passivation. Na⁺ can diffuse into the perovskite layer to enhance its photocatalytic efficiency (Photocatalysis is a process where light energy, typically from the sun or artificial light sources, is used to accelerate a chemical reaction). For instance, the presence of Na⁺ ions can help in the separation of photo-generated electron-hole pairs. This reduces the recombination rate of these pairs, enhancing the efficiency of the photocatalytic process. K²⁺ ions can combine with uncoordinated halide ions to passivate vacancy defects of A-site cations, while potassium ions can prevent the formation of Frenkel defects. Divalent or trivalent metal cations are also used as passivators. Al-acac3 can reduce strain in polycrystalline films, while Ni²⁺ can reduce vacancy defects of Pb and I [100]. However, defect levels can introduce non-radiative recombination, which can negatively impact PCE and device stability. Doping rare-earth elements into perovskite films can achieve high PCE and stability, even after continuous sunlight irradiation for 1500 hours [101].

Anions Anions are used to passivate defects in perovskite films, such as Pb and halide vacancies [102]. Excessive iodide or iodine can inhibit halide vacancy formation, while bromide ions can adjust the bandgap of perovskite [103]. Barrier bending occurs and defects at grain boundaries are passivated after introducing bromide. Barrier bending specifically refers to the distortion or bending of the energy bands at the interfaces between different regions of a material or at the grain boundaries in polycrystalline materials. This occurs because grain boundaries often contain imperfections, like vacancies, dislocations, or impurities, which create localized electric fields. These fields cause the energy bands to bend near the boundary. Additives like PbCl₂ can passivate defects at grain boundaries or surfaces, but may damage device stability [104]. Rubidium chloride can convert excess PbI₂ into inactive complexes, achieving a certified ultra-high PCE of 25.6%.

3.4.1.2 Organic Molecules

Organic molecules with specific functional groups can improve film quality, PCE, and stability in perovskite devices. Despite their larger molecular sizes, these molecules interact with

ions on the perovskite film surface, regulating crystallization and repairing defects [105].

Organic Ammonium Salt As a constituent of perovskite materials, organic ammonium salts can also stimulate defect passivation [106]. Son et al. introduced excess MAI into a perovskite precursor solution (Figure 3.5) and found that Excess MAI can passivate dangling bonds at grain boundaries, suppressing non-radiative recombination and reducing hysteresis in devices [107]. Excess MAI at the interface between perovskite and hole transport layers affects energy level adjustment. Materials with excess MA in H_2O can trigger anti-degradation reactions [108].

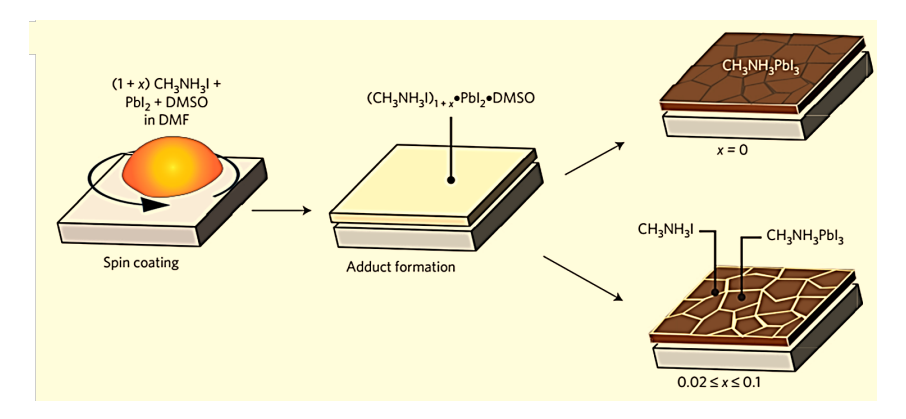


Figure 3.5: Illustration of the coating process utilized to create CH₃NH₃PbI₃ films with and without excess MAI [107].

Lewis Acid Perovskite films contain electron-rich defects, known as Lewis bases, which can be passivated by introducing an electron-withdrawing Lewis acid. This results in reduced non-radiative recombination and improved photovoltaic performance. Fullerenes and their derivatives are widely used for passivating these defects, as they are favorable for carrier transport due to their high electron mobility [109,110]. The development of novel fullerenes with specific functions can further enhance the photovoltaic efficiency of perovskite solar cells (PSC $_s$) [111].

3.4.2 Passivation of Defects on the Surface of Perovskite

Perovskite solar cells have a sandwich structure, with the perovskite absorption layer between electron and hole transport layers. Interfaces between perovskite films and transport layers can cause defects, affecting performance and stability. Defect density at grain boundaries is higher than bulk, leading to recombination losses and degradation. Reducing defect density is crucial for improving PCE and stability [112].

3.4.2.1 Perovskite/Hole Transport Layer Interface

The hole transport layer and perovskite layer interface is a major location for defects, causing degradation and reduced device stability. Defect passivation is crucial for high-performance perovskite solar cells. Research materials for passivation include organic small molecules, polymers, and low-dimensional perovskite structures [113]. Methods like thiophene dicarboxylic acid, phosphine oxide, crown ether complexation, and secondary reactions have improved device stability, reduced defect site reactivation, and enhanced hydrophobicity. Fluorine's hydrophobic nature also enhances stability [114, 115].

3.4.2.2 Electron/Perovskite Transport Layer Interface

Metal oxides like T_iO_2 and SnO_2 in conventional structure devices have defect sites that can cause voltage losses and instability [116]. To address these issues, materials like amphoteric ion molecules, small organic molecules, fullerene, and metal compounds are used. Amphoteric ionic molecules can passivate interface defects by establishing chemical interactions with the perovskite layer and/or ETL [117]. Examples of such modifications include ammonium fluoride and potassium tetrafluoroborate, which have been shown to improve coverage, growth, and charge transfer in perovskite films [118].

Chapter 4

Stability issue- Comparison between P-I-N and N-I-P PSCs

4.1 Introduction

Perovskite solar cells (PSCs) have garnered significant attention in the field of photovoltaics, thanks to their impressive power conversion efficiencies and cost-effective fabrication methods. Despite their potential, a key obstacle to their commercialization is their inherent instability, particularly when exposed to external factors such as moisture, heat, or light over prolonged periods. Addressing and resolving these stability issues is essential for the widespread adoption and success of perovskite solar cells [119].

SCAPS (Solar Cell Capacitance Simulator) is an advanced and widely utilized simulation tool for analyzing the performance and characteristics of various solar cell types, including perovskite solar cells. By SCAPS, the scientific community can advance the development of perovskite solar cells and other photovoltaic technologies, ultimately contributing to the global shift towards renewable energy solutions. Researchers can accurately simulate the behavior of perovskite solar cells under different operating conditions, providing valuable insights into the underlying mechanisms that contribute to their instability [120].

The objective of this study is to conduct a comparative analysis between N-I-P and P-I-N perovskite solar cells to determine which configuration demonstrates greater stability against degradation under operational conditions. Mainly, this work is a continuation of a previous work (Master's dissertation) that resulted in a published paper [79]. In the previous work, the stability issues were studied in a N-I-P structure of a perovskite solar cell (N-I-P PSC). The current work aims to study the stability issue in the P-I-N solar cell and then make a comparison with the N-I-P cell. Therefore, the primary cell targeted for study is the P-I-N.

As detailed in Chapters 2 and 3, degradation is influenced by several factors such as continuous illumination, temperature, humidity, and other environmental conditions. By simulating the degradation processes caused by these factors, researchers can obtain valuable insights into the underlying mechanisms of degradation. Understanding the impact of these degradation-induced defects on device performance is crucial for devising strategies to enhance stability and extend the device's lifetime.

In this study, we employ the Solar Cell Capacitance Simulator (SCAPS) as a simulation tool to investigate stability issues. Our focus is on elucidating the influence of different types of defects created by degradation processes. Through comprehensive analysis, we aim to gain insights into the involved relationship between defect formation and device performance degradation in both P-I-N and N-I-P structures. Ultimately, this research will pave the way for the development of more stable and reliable perovskite solar cell technologies.

4.2 SCAPS

SCAPS-1D has been developed to simulate the operation of thin-film solar cells. SCAPS is originally developed for cell structures of the CuInSe₂ and the CdTe family. Several extensions however have improved its capabilities so that it is also applicable to crystalline solar cells (Si and GaAs family) and amorphous cells (a-Si and micromorphous Si) [121]. SCAPS is a Windows-oriented program, which is opened with the 'Action Panel' (Figure 4.1).

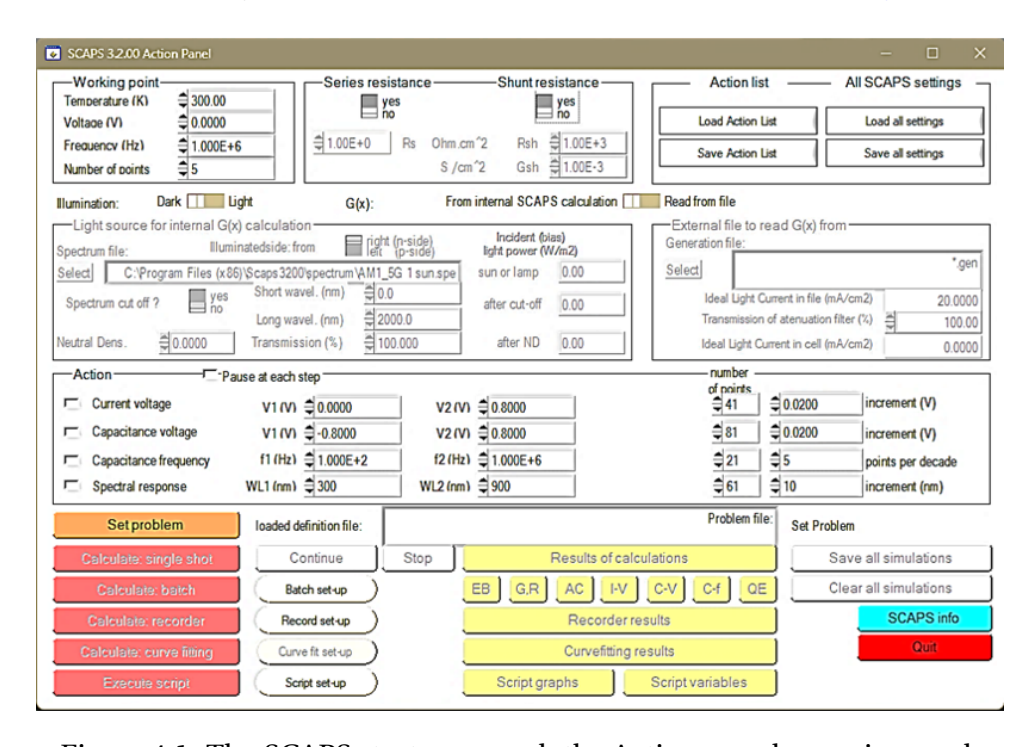


Figure 4.1: The SCAPS start-up panel: the Action panel or main panel.

4.2.1 Definition of the problem

By clicking the button set problem(Figure 4.2)in the action panel, we can chose load in the lower right corner of the new opened panel to select an example to study which can be modified in the cell properties [121].



Figure 4.2: Definition of problem panel and selection of example.

4.2.2 Define the working point

The working point specifies the parameters which are not varied in a measurement simulation, and which are relevant to that measurement (Figure 4.3) [121]. Thus:

- Temperature (T): Necessary for all measurements. $N_c(T)$, $N_v(T)$, the thermal velocities, the thermal voltage K_BT and all their derivaties are the only variables which have an explicit temperature dependence. These parameters must be inserted manually for each temperature.
- The voltage V: is unnecessary in I-V and C-V simulation, but it is taken as the dc-bias voltage in C-f simulation and in $QE(\lambda)$ simulation. SCAPS always starts at 0V, and proceeds at the working point voltage in a number of steps that also should be specified.
- The frequency f: is neglected in I-V, $QE(\lambda)$ and C-f simulation. But C-V measurement is taken into account.
- The illumination: is used for all measurements. For the $QE(\lambda)$ measurement, it determines the bias light conditions. The basis settings are: dark or light, choice of the illuminated side, choice of the spectrum. The default is one sun(=1000 W/m²) illumination with the 'air mass 1.5, global' spectrum, but there is a large choice of monochromatic light and spectra for specialized simulations.

4.2.3 Selection of the measurement(s) to simulate

In the action-part of the Action Panel, the following measurements: I-V, C-V, C-f and $QE(\lambda)$ can be simulated . We can adjust if necessary the start and end values of the argument, and the number of steps (Figure 4.4) [121].

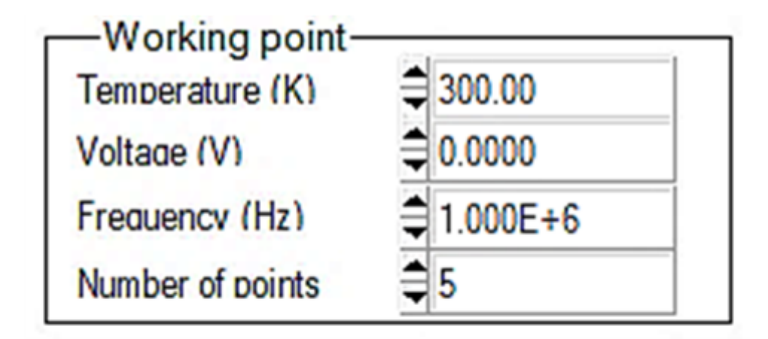


Figure 4.3: Definition of the working point.

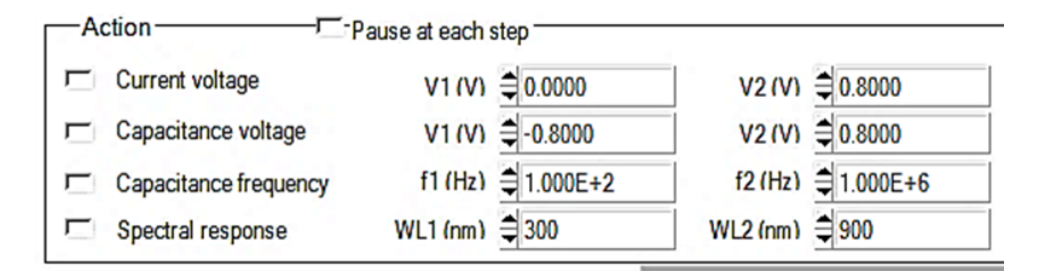


Figure 4.4: Selection of the measurement(s) to simulate.

4.2.4 Starting the calculation(s)

By clicking the button, we calculate: single shot in the action panel. The Energy Bands Panel opens, and the calculations start. Meanwhile, SCAPS offers a free movie how the conduction and valence bands, the Fermi levels and the whole caboodle are evolving [121].

4.2.5 Displaying the simulated curves

After the calculation(s), SCAPS switches to the Energy band panel (or the AC-band panel) in which the band diagrams, carrier densities, current densities are shown. The results (buttons save graphs, show data (the numbers are shown on screen) or save data (the numbers are saved to a file). One of specialized output panels can be switched (Figure 4.5) [121].

Simulation procedure using SCAPS software can be summarized by the scheme presented in Figure 4.6.

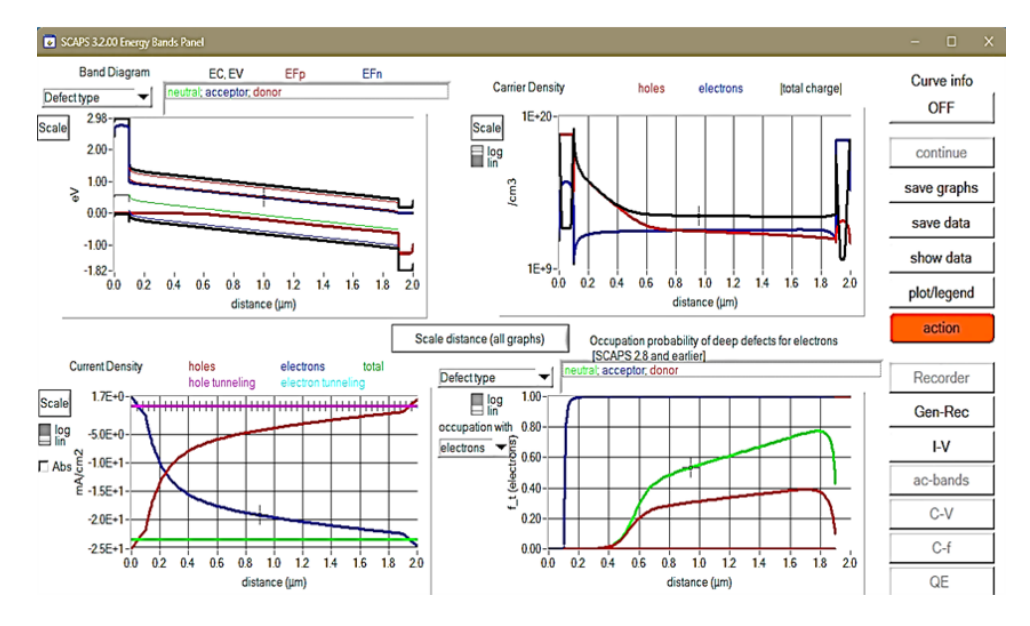


Figure 4.5: Results panels.

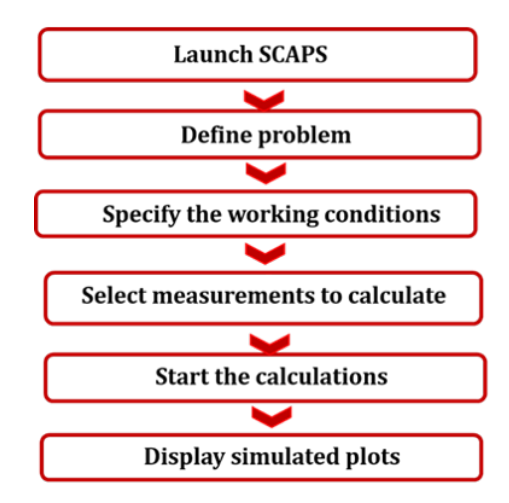


Figure 4.6: : Simulation procedure using SCAPS software.

4.3 Material inputs and defects used to simulate the working condition

There are 12 possible native point defects in the MAPbI₃ structure, such as vacancies V_{MA} , V_{pb} , and V_{I} ; interstitials MA_{i} , Pb_{i} , and I_{i} ; and anti-site occupations MA_{pb} , MA_{i} , Pb_{MA} , Pb_{i} , I_{MA} , and I_{pb} , which have been widely studied [92, 122]. For more details see chapter 3.

In this chapter, the investigation of degradation will be carried out on the basis of four types of defect selected from the 12 listed below. These include the recombination center (N_R) situated at E_v +0.6 eV , which is electrically neutral, the shallow donor trap (N_{DT}) situated at E_c -0.1 eV (known for trapping electrons), the deep donor trap (N_{DP}) situated at E_c -0.38 eV, and the shallow acceptor trap (N_{AT}) situated at E_v +0.1 eV (which serves as hole

traps).

This analysis will consider various probable locations of these defects; at the HTL/bulk interface, the bulk and the ETL/bulk, for both P-I-N and N-I-P configurations. In addition, further material inputs are given in Table 4.1 and Table 4.2 for the respective structures P-I-N and N-I-P, illustrated in Figure 4.7. The P-I-N PSC comprises PEDOT (an organic p-type material) as the hole transport layer (HTL), located at the front of the cell. This means it is on the illuminated side. Then, there is the active layer, responsible for photon absorption, exciton formation, and dissociation, which is the perovskite layer. Following that is the electron transport layer (ETL) formed by PC60BM, an organic n-type material. The N-I-P PSC is quite different regarding the ETL and HTL materials. Indeed, an N-I-P PSC does not simply mean inverting a P-I-N PSC. This is because the materials used should be suitable for both the illumination and collection sides. For example, in the N-I-P PSC, the ETL used is TiO₂, an inorganic, transparent n-type semiconductor, while the HTL is SpiroOMeTED, a p-type organic material. The choice of ETL and HTL materials in both structures was inspired from previous research works [79, 123–128].

Table 4.1: Material's inputs used in the simulation for the P-I-N PSC [123].

Parameter	PEDOT	$MAPbI_3$	$PC_{60}BM$
d (μm)	0.1	1.8	0.1
E_g (eV)	3.0	1.55	2.0
N_c (cm ⁻³)	$1\cdot 10^{19}$	$2\cdot 10^{18}$	$2.5\cdot10^{21}$
$N_{\nu}~(\mathrm{cm}^{-3})$	$1\cdot 10^{19}$	$2 \cdot 10^{19}$	$2.5\cdot10^{21}$
$q\chi$ (eV)	2.4	3.6	3.850
μ_n (cm ² /Vs)	$4.5\cdot10^{-4}$	40	$2 \cdot 10^{-1}$
$\mu_p (\text{cm}^2/\text{Vs})$	$1 \cdot 10^{-3}$	10	$2 \cdot 10^{-1}$
N_D (cm ⁻³)	/	1	$2\cdot 10^{18}$
N_A (cm ⁻³)	$5\cdot 10^{18}$	/	1

Table 4.2: Material's inputs used in the simulation for the N-I-P PSC [124, 125].

Parameter	TiO ₂ (ETL)	$MAPbI_3$	Spiro-OMeTAD
d (μm)	0.1	1.8	0.1
E_{g} (eV)	3.2	1.55	3.3
N_c (cm ⁻³)	$1\cdot 10^{21}$	$2\cdot 10^{18}$	$1\cdot 10^{19}$
$N_{\nu}~(\mathrm{cm}^{-3})$	$2\cdot 10^{20}$	$2 \cdot 10^{19}$	$1\cdot 10^{19}$
$q\chi$ (eV)	4.1	3.9	2.0
μ_n (cm ² /Vs)	20	40	$2 \cdot 10^{-3}$
$\mu_p (\text{cm}^2/\text{Vs})$	10	10	$2 \cdot 10^{-4}$
N_D (cm ⁻³)	$2\cdot 10^{18}$	1	/
N_A (cm ⁻³)	1	/	$2\cdot 10^{18}$

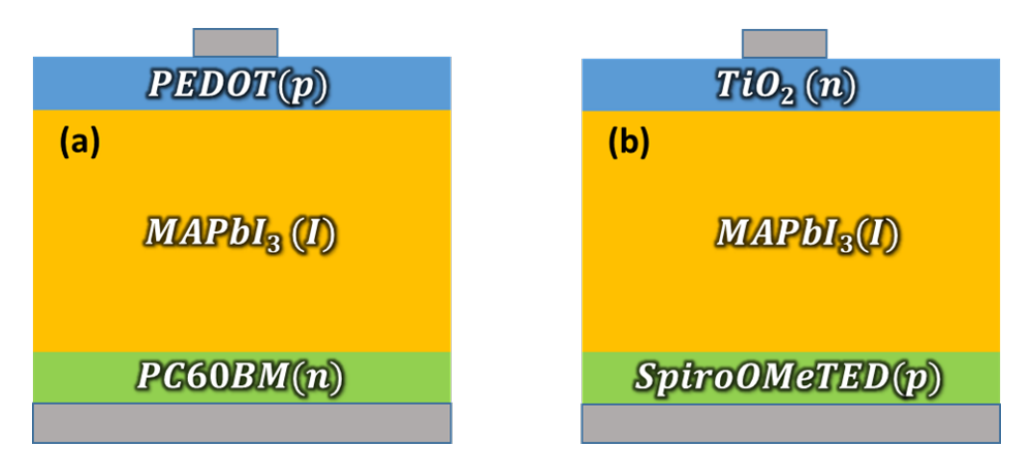


Figure 4.7: The studied structures of the P-I-N and N-I-P PSC.

4.4 Results and discussion

4.4.1 Initial case

In the initial scenario, we are referring to the state before any degradation or instability occurs, which is characterized by low defect densities. The obtained J-V characteristics for both P-I-N PSC and N-I-P PSC are illustrated, respectively, in Figure 4.8. The obtained simulations were also compared to experimental measurement from other works [126–128].

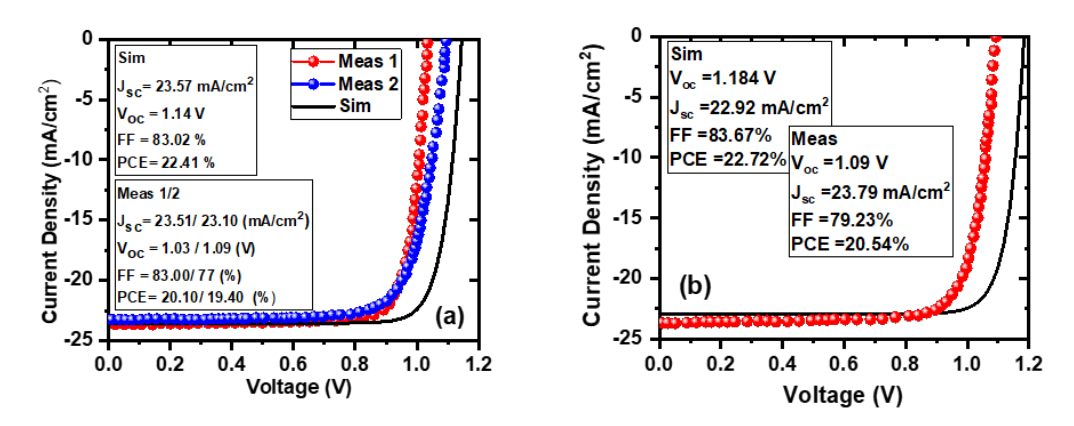


Figure 4.8: J-V characteristic calculated by SCAPS for initial case, i.e. low defect densities: (a) in P-I-N PSC ,(b) in N-I-P PSC.

We observe nearly a similarity in the electrical output parameters for both cells and an acceptable comparison with experimental measurements. In general, the N-I-P PSC cell exhibits slightly higher efficiency than the P-I-N PSC cell in both simulation and experimental results.

Table 4.3: Initial electrical outputs (Before degradation) compared to experimental measurements. Data for the P-I-N PSC are from [126, 128] and data for the N-I-P PSC are from [127].

Structure	J_{SC} (mA/cm ²)	V_{OC} (V)	FF (%)	PCE (%)
P-I-N				
Simulation	23.57	1.14	83.02	22.41
Measurement 1	23.51	1.03	83.00	20.10
Measurement 2	23.10	1.09	77.00	19.40
N-I-P				
Simulation	22.92	1.18	83.67	22.72
Measurement	23.79	1.09	79.23	20.54

4.4.2 Effect of defects at the HTL/bulk interface

Figure 4.9 depicts how the presence of recombination center N_R , shallow donors N_{DT} , and shallow acceptors N_{AT} affects the J-V characteristic when these defects are incorporated at the interface between the perovskite layer and the HTL. The extracted electrical outputs in each case are summarized in Table 4.4 to Table 4.6. According to the obtained results, no significant effect of the HTL/bulk defects is remarked.

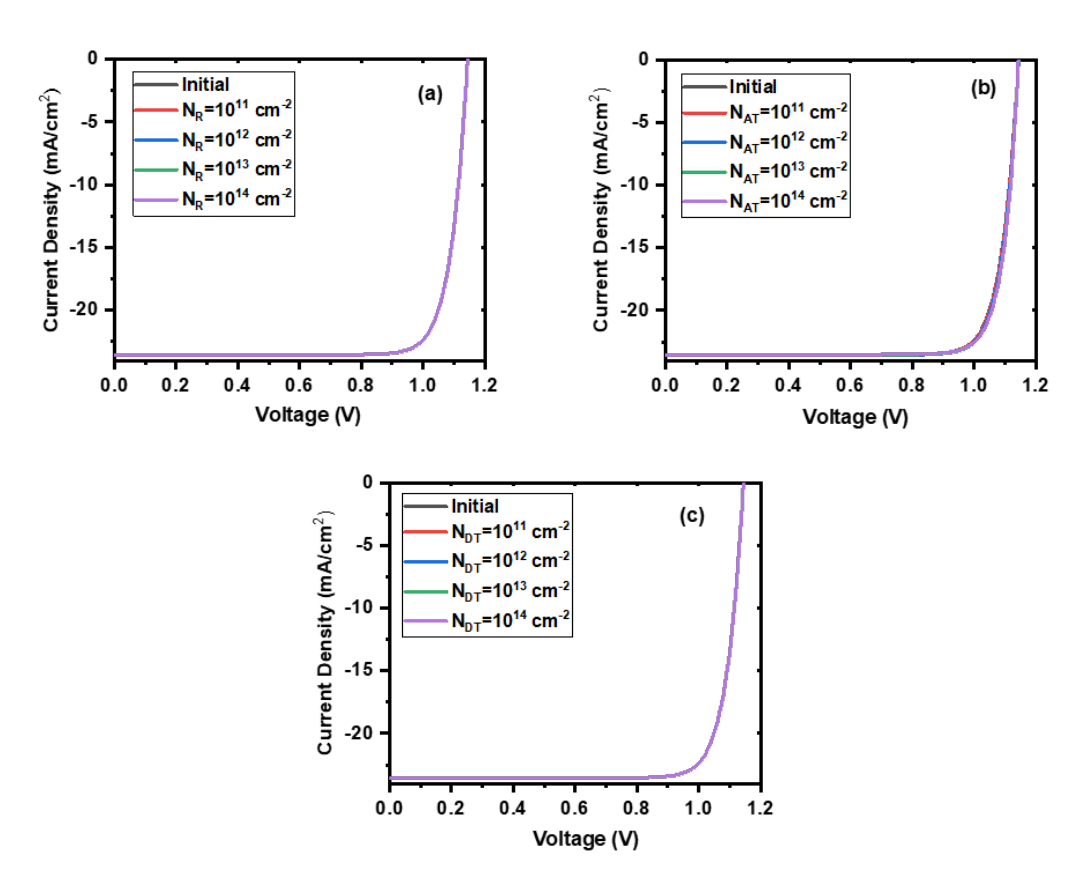


Figure 4.9: J-V characteristic of the P-I-N PSC calculated by SCAPS when defects are at the HTL/bulk interface: (a) recombination center, (b) shallow donor and (c) shallow accepter.

Table 4.4: Effect of HTL/bulk interface defects on electrical output of the P-I-N PSC when defect density of N_R was varied from 10^{11} to 10^{14} cm⁻².

Condition	J_{SC} (mA/cm ²)	V_{OC} (V)	FF (%)	PCE (%)
Initial	23.574	1.145	83.024	22.408
$N_R = 10^{11} \text{ cm}^{-2}$	23.574	1.145	83.024	22.408
$N_R = 10^{12} \text{ cm}^{-2}$	23.575	1.145	83.024	22.408
$N_R = 10^{13} \text{ cm}^{-2}$	23.575	1.145	83.024	22.408
$N_R = 10^{14} \text{ cm}^{-2}$	23.575	1.145	83.025	22.408

Table 4.5: Effect of HTL/bulk interface defects on electrical output of the P-I-N PSC when defect density of N_{AT} was varied from 10^{11} to 10^{14} cm⁻².

Condition	J_{SC} (mA/cm ²)	V_{OC} (V)	FF (%)	PCE (%)
Initial	23.574	1.145	83.024	22.408
$N_{AT} = 10^{11} \text{ cm}^{-2}$	23.574	1.145	83.090	22.425
$N_{AT} = 10^{12} \text{ cm}^{-2}$	23.571	1.145	83.468	22.518
$N_{AT} = 10^{13} \text{ cm}^{-2}$	23.558	1.144	83.826	22.595
$N_{AT} = 10^{14} \text{ cm}^{-2}$	23.527	1.144	83.855	22.571

Table 4.6: Effect of HTL/bulk interface defects on electrical output of the P-I-N PSC when defect density of N_{DT} was varied from 10^{11} to 10^{14} cm⁻².

Condition	J_{SC} (mA/cm ²)	V_{OC} (V)	FF (%)	PCE (%)
Initial	23.574	1.145	83.024	22.408
$N_{DT} = 10^{11} \text{ cm}^{-2}$	23.575	1.145	83.024	22.408
$N_{DT} = 10^{12} \text{ cm}^{-2}$	23.575	1.145	83.024	22.408
$N_{DT} = 10^{13} \text{ cm}^{-2}$	23.575	1.145	83.024	22.408
$N_{DT} = 10^{14} \text{ cm}^{-2}$	23.575	1.145	83.024	22.408

Table 4.7: Effect of HTL/bulk interface defects on electrical output of the P-I-N PSC when all defect densities N_R , N_{DT} , and N_{AT} are equal to 10^{14} cm⁻².

Condition	J_{SC} (mA/cm ²)	V_{OC} (V)	FF (%)	PCE (%)
$N_R = N_{AT} = N_{DT} = 10^{14} \text{ cm}^{-2}$	23.527	1.144	83.855	22.571

When all defects are present at a density of $N_R = N_{AT} = N_{DT} = 10^{14}$ cm⁻² (Figure 4.10, Table 4.7 and Table 4.8), the results are as follows: in the P-I-N structure, J_{sc} decreases very slightly to 23.527 mA/cm², V_{oc} remains at 1.14 V, FF increases slightly to 83.855 %, yielding to a slight increase in PCE of 22.571 %. In the N-I-P structure, J_{sc} remains at 22.927 mA/cm², while V_{oc} drops to 1.091 V . However, FF shows a notable increase, reaching 86.851 %, and a slight reduction in PCE occurs to 21.725 %. These results indicate that, although the P-I-N showed a slightly lower PCE compared to the N-I-P in the initial state, it is less sensitive to HTL/bulk interface defects.

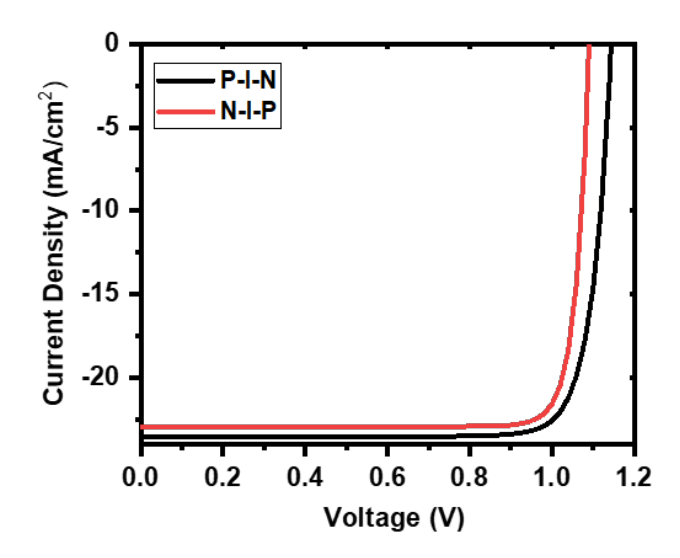


Figure 4.10: : Comparison of the effect of HTL/bulk interface defects in P-I-N PSC and N-I-P PSC .

Table 4.8: Comparison of the effect of HTL/bulk interface defects in P-I-N PSC and N-I-P PSC when all defect densities N_R , N_{DT} , and N_{AT} are equal to 10^{14} cm⁻².

Structure	J_{SC} (mA/cm ²)	V_{OC} (V)	FF (%)	PCE (%)
P-I-N				
Initial	23.574	1.145	83.024	22.408
Degraded	23.527	1.144	83.855	22.571
N-I-P				
Initial	22.927	1.180	83.670	22.720
Degraded	22.927	1.091	86.851	21.725

4.4.3 Effect of defects in the bulk

Figure 4.11 illustrates the influence of recombination centers (N_R), deep and shallow donors (N_{DP} , N_{AT}), and shallow acceptors (N_{AT}) on the J-V characteristic. These defects are in the bulk perovskite layer. The extracted electrical outputs are summarized in Table 4.9 to Table 4.12. We can summarize the obtained results as follows:

Table 4.9: Effect of the bulk defects on electrical output of the P-I-N PSC when defect density of N_R is varied from 10^{14} to 10^{16} cm⁻³.

Condition	J_{SC} (mA/cm ²)	V_{OC} (V)	FF (%)	PCE (%)
Initial	23.574	1.145	83.024	22.408
$N_R = 10^{14} \text{ cm}^{-3}$	23.567	1.106	79.901	20.825
$N_R = 10^{15} \text{ cm}^{-3}$	23.495	1.018	72.724	17.398
$N_R = 10^{16} \text{ cm}^{-3}$	22.796	0.937	58.222	12.432

In the case of N_R :

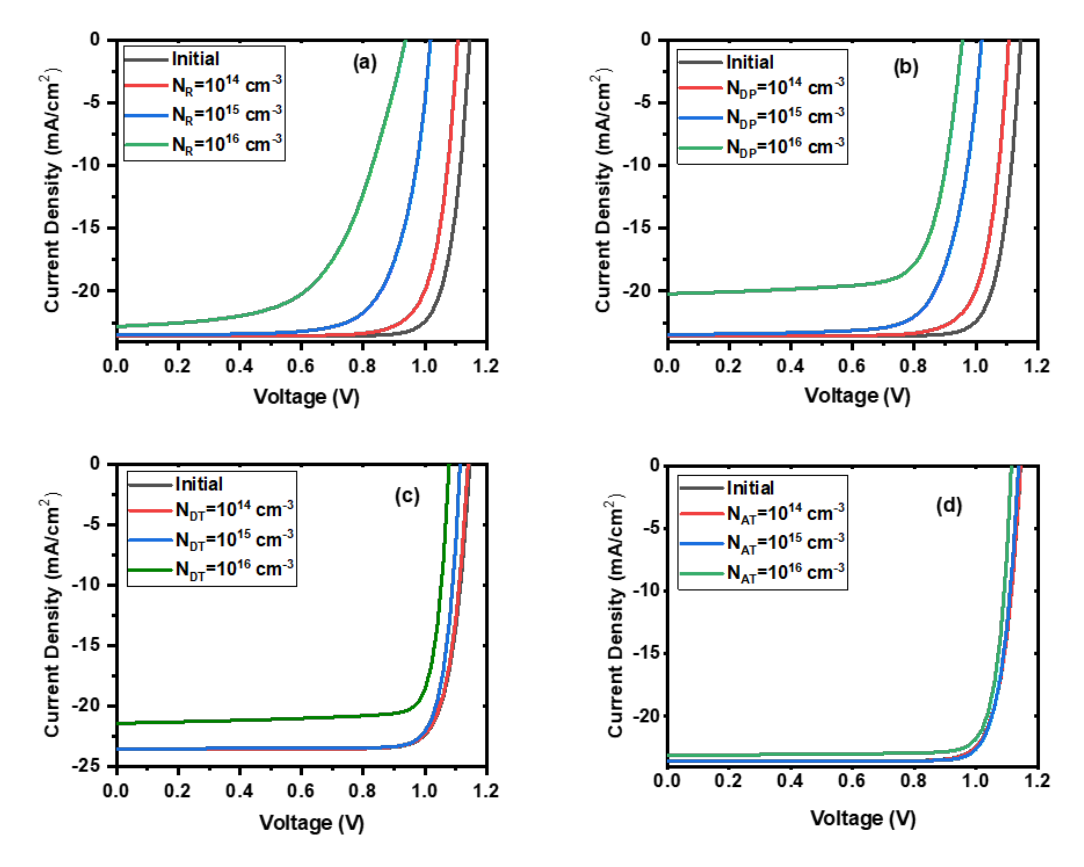


Figure 4.11: J-V characteristic of the P-I-N PSC calculated by SCAPS when defects are in the bulk of the perovskite: (a) recombination center, (b) deep donor, (c) shallow donor and (d) shallow accepter.

- As the defect density increases, all electrical parameters (J_{SC} , V_{oc} , FF, and PCE) degrade significantly
- The PCE drops from 22.408% to 12.432%, indicating that N_R defects introduce severe charge recombination.
- The V_{oc} shows the most drastic decrease from 1.145 to 0.937 V, indicating increased non-radiative recombination losses.

In the case of N_{DP} :

- N_{DP} defects cause significant degradation in J_{sc} and V_{oc} , leading to a reduction in efficiency.
- The impact on FF is less severe compared to N_R defects, implying a different recombination mechanism.
- The PCE reduces to 14.329% at 10^{16} cm⁻³, showing that deep-level defects play a crucial role in non-radiative recombination.

Table 4.10: Effect of the bulk defects on electrical output of the P-I-N PSC when defect density of N_{DP} changes from 10^{14} to 10^{16} cm⁻³.

Condition	J_{SC} (mA/cm ²)	V_{OC} (V)	FF (%)	PCE (%)
Initial	23.574	1.145	83.024	22.408
$N_{DP} = 10^{14} \text{ cm}^{-3}$	23.567	1.106	79.742	20.783
$N_{DP} = 10^{15} \text{ cm}^{-3}$	23.455	1.018	74.194	17.721
$N_{DP} = 10^{16} \text{ cm}^{-3}$	20.209	0.956	74.162	14.329

Table 4.11: Effect of the bulk defects on electrical output of the P-I-N PSC when defect density of N_{DT} is varied from 10^{14} to 10^{16} cm⁻³.

Condition	J_{SC} (mA/cm ²)	V_{OC} (V)	FF (%)	PCE (%)
Initial	23.574	1.145	83.024	22.408
$N_{DT} = 10^{14} \text{ cm}^{-3}$	23.571	1.139	83.267	22.361
$N_{DT} = 10^{15} \text{ cm}^{-3}$	23.539	1.114	84.684	22.209
$N_{DT} = 10^{16} \text{ cm}^{-3}$	21.439	1.079	83.571	19.326

Table 4.12: Effect of the bulk defects on electrical output of the P-I-N PSC when defect density of N_{AT} is varied from 10^{14} to 10^{16} cm⁻³.

Condition	J_{SC} (mA/cm ²)	V_{OC} (V)	FF (%)	PCE (%)
Initial	23.574	1.145	83.024	22.408
$N_{AT} = 10^{14} \text{ cm}^{-3}$	23.577	1.144	83.134	22.426
$N_{AT} = 10^{15} \text{ cm}^{-3}$	23.574	1.138	84.311	22.626
$N_{AT} = 10^{16} \text{ cm}^{-3}$	23.099	1.115	84.738	21.827

Table 4.13: Effect of the bulk defects on electrical output of the P-I-N PSC when all defect densities N_R , N_{DT} , N_{DP} , and N_{AT} are equal to 10^{16} cm⁻³.

Condition	J_{SC} (mA/cm ²)	V_{OC} (V)	FF (%)	PCE (%)
$N_R = N_{AT} = N_{DT} = N_{DP} = 10^{16} \text{ cm}^{-3}$	19.413	0.931	72.871	13.175

Table 4.14: Comparison between P-I-N PSC and N-I-P PSC of the bulk defect's effect when all defect densities N_R , N_{DT} , N_{DP} , and N_{AT} are equal to 10^{16} cm⁻³.

Structure	J_{SC} (mA/cm ²)	V_{OC} (V)	FF (%)	PCE (%)
P-I-N				
Initial	23.574	1.145	83.024	22.408
Degraded	19.413	0.931	72.871	13.175
N-I-P				
Initial	22.927	1.180	83.670	22.720
Degraded	4.559	0.853	62.521	2.430

In the case of N_{DT} :

• N_{DT} defects have a moderate impact on PSC performance.

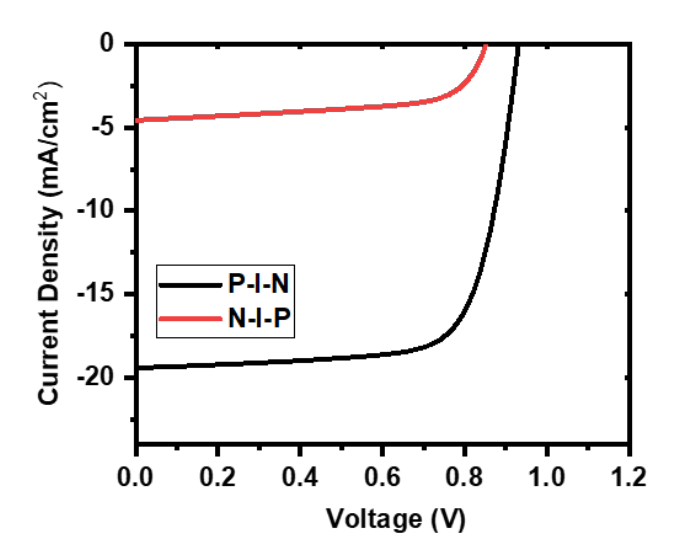


Figure 4.12: Comparison of the effect of the bulk defects in P-I-N PSC and N-I-P PSC.

- Unlike N_R and N_{DP} defects, FF remains high, indicating that charge transport is not significantly affected.
- The drop in V_{oc} and J_{sc} at 10^{16} cm⁻³ suggests recombination still occurs, but less severely than in N_R or N_{DP} defects.
- The PCE decreases to 19.326%, making N_{DT} defects less detrimental compared to the previous two types.

In the case of N_{AT} :

- N_{AT} defects show minimal impact on PSC performance, even at high densities.
- FF even increases slightly, possibly due to better charge transport.
- The overall efficiency remains high (21.827% at $10^{16} \,\mathrm{cm}^{-3}$), indicating N_{AT} defects are less detrimental than N_R , N_{DP} , and N_{DT} .

The electrical outputs obtained when all defects in the perovskite absorber have a high density of 10^{16} cm⁻³ are: J_{sc} =19.413mA/cm², V_{oc} =0.931 V, FF = 72.87%, and PCE = 13.17 % (see Table 4.13, Figure 4.12 and Table 4.14.). This demonstrates the significant impact of a high bulk defect densities on the electrical performance of the P-I-N PSC. According to a previous paper [79], the bulk defects were related to thermal stress and induced a severe degradation of the PCE to 2.43 % in the N-I-P PSC, as presented in Figure 4.12 and Table 4.14. If we compare the effect of the bulk defects as the result of thermal stress in the P-I-N PSC and the N-I-P PSC, we can easily conclude that the P-I-N is more robust.

4.4.4 Effect of defects at Bulk/ETL interface

Figure 4.13 illustrates the influence of recombination centers (N_R) , shallow donors (N_{DT}) , and shallow acceptors (N_{AT}) on the J-V characteristic. These defects are at the interface between the Electron Transport Layer (ETL) and the perovskite layer. The extracted electrical outputs are summarized in Table 4.15 to Table 4.18

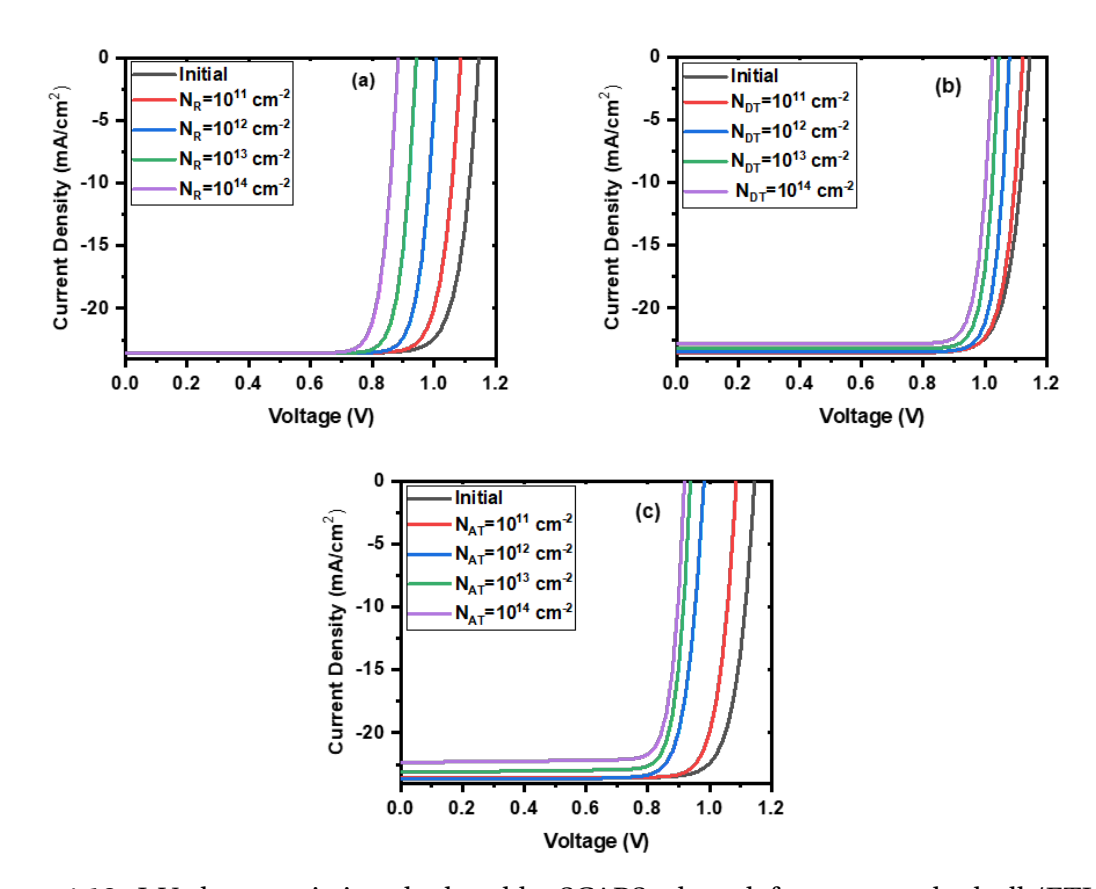


Figure 4.13: J-V characteristic calculated by SCAPS when defects are at the bulk/ETL interface: (a) recombination center, (b) shallow donor and (c) shallow acceptor.

The obtained results can be summarized as follows: In the case of N_R :

- J_{sc} remains constant at approximately 23.574 mA/cm², indicating that N_R defects do not significantly hinder charge generation.
- V_{oc} decreases progressively from 1.145 V to 0.884 V as defect density increases, suggesting that N_R defects act as recombination centers, reducing the built-in potential
- FF% initially increases slightly at 10¹² cm⁻² but decreases at higher defect densities, indicating an initial improvement in charge transport that is negated by excessive recombination at very high defect densities.

• PCE drops from 22.408% to 17.463%, showing a nearly 22% efficiency loss due to N_R defects.

Table 4.15: Effect of the bulk/ETL interface defects on electrical output of the P-I-N PSC when defect density of N_R is varied from 10^{11} to 10^{14} cm⁻².

Condition	J_{SC} (mA/cm ²)	V_{OC} (V)	FF (%)	PCE (%)
Initial	23.574	1.145	83.024	22.408
$N_R = 10^{11} \text{ cm}^{-2}$	23.574	1.087	83.864	21.489
$N_R = 10^{12} \text{ cm}^{-2}$	23.574	1.009	84.905	20.197
$N_R = 10^{13} \text{ cm}^{-2}$	23.574	0.943	84.781	18.845
$N_R = 10^{14} \text{ cm}^{-2}$	23.571	0.884	83.813	17.463

Table 4.16: Effect of the bulk/ETL interface defects on electrical output of the P-I-N PSC when defect density of N_{DT} is varied from 10^{11} to 10^{14} cm⁻².

Condition	J_{SC} (mA/cm ²)	V_{OC} (V)	FF (%)	PCE (%)
Initial	23.574	1.145	83.024	22.408
$N_{DT} = 10^{11} \text{ cm}^{-2}$	23.568	1.122	84.500	22.344
$N_{DT} = 10^{12} \text{ cm}^{-2}$	23.504	1.079	86.412	21.918
$N_{DT} = 10^{13} \text{ cm}^{-2}$	23.214	1.045	86.647	21.029
$N_{DT} = 10^{14} \text{ cm}^{-2}$	22.834	1.025	86.366	20.206

Table 4.17: Effect of the bulk/ETL interface defects on electrical output of the P-I-N PSC when defect density of N_{AT} changes from 10^{11} to 10^{14} cm⁻².

Condition	J_{SC} (mA/cm ²)	V_{OC} (V)	FF (%)	PCE (%)
Initial	23.574	1.145	83.024	22.408
$N_{AT} = 10^{11} \text{ cm}^{-2}$	23.581	1.086	83.745	21.447
$N_{AT} = 10^{12} \text{ cm}^{-2}$	23.636	0.982	82.996	19.255
$N_{AT} = 10^{13} \text{ cm}^{-2}$	23.119	0.938	84.634	18.355
$N_{AT} = 10^{14} \text{ cm}^{-2}$	22.343	0.919	84.868	17.426

Table 4.18: Effect of the bulk/ETL interface defects on electrical output of the P-I-N PSC when all defect densities N_R , N_{DT} , and N_{AT} are equal to 10^{14} cm⁻².

Condition	J_{SC} (mA/cm ²)	V_{OC} (V)	FF (%)	PCE (%)
$N_R = N_{AT} = N_{DT} = 10^{14} \text{ cm}^{-2}$	23.601	0.827	82.495	16.105

In the case of N_{DT} :

• J_{sc} slightly decreases from 23.574 mA/cm² to 22.834 mA/cm² at 10^{14} cm⁻², suggesting a minor impact on charge collection.

Table 4.19: Comparison of the effect of the bulk/ETL interface defects in P-I-N PSC and N-I-P PSC when all defect densities N_R , N_{DT} , and N_{AT} are equal to 10^{14} cm⁻².

Structure	J_{SC} (mA/cm ²)	V_{OC} (V)	FF (%)	PCE (%)
P-I-N				
Initial	23.574	1.145	83.024	22.408
Degraded	23.601	0.827	82.495	16.105
N-I-P				
Initial	22.927	1.180	83.670	22.720
Degraded	22.913	0.879	82.370	16.605

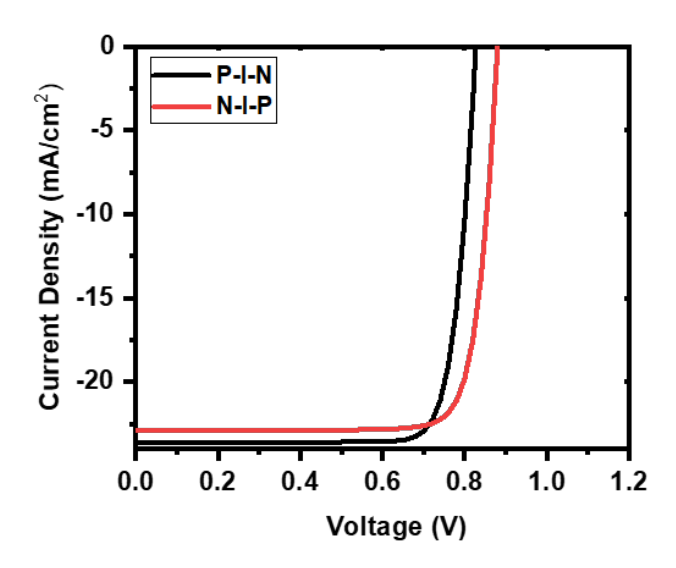


Figure 4.14: : Comparison of the effect of the bulk/ETL defects in P-I-N PSC and N-I-P PSC.

- V_{oc} decreases but remains higher than in the N_R case, dropping from 1.145 V to 1.025 V, implying that N_{DT} defects contribute to recombination but not as severely as N_R defects.
- FF% improves significantly at moderate defect levels (86.647% at $10^{13}~{\rm cm}^{-3}$) before slightly decreasing at higher densities. This suggests that N_{DT} defects initially enhance charge extraction before excessive recombination takes over.
- PCE falls from 22.408% to 20.206%, showing a relatively smaller efficiency loss (10%) compared to N_R defects.

In the case of N_{AT} :

• J_{sc} remains stable at lower defect densities but drops more noticeably at 10^{14} cm⁻² (22.343 mA/cm²), indicating that N_{AT} defects may affect charge collection more than N_R or NDT defects.

- V_{oc} declines from 1.145 V to 0.919 V, showing a significant voltage loss similar to N_R defects.
- FF% increases at moderate defect levels but stabilizes around 84.868% at 10¹⁴ cm⁻².
- PCE decreases significantly from 22.408% to 17.426%, a reduction of 22%, indicating that N_{AT} defects strongly affect efficiency.
- N_{AT} defects influence both charge recombination and collection, leading to significant performance losses. Their effect is similar to N_R defects.

When all defect types are present at high densities, their negative effects are compounded, resulting in severe recombination and voltage loss. P-I-N degrades to PCE = 16.105%, while N-I-P to 16.605%, suggesting that the N-I-P architecture is slightly more resistant to defect-induced degradation.

4.5 Conclusion

This study systematically examined the impact of the HTL/bulk, the bulk and the bulk/ETL defects on the performance of perovskite solar cells (PSCs) with both P-I-N and N-I-P architectures. The findings highlight the critical influence of defect density on key performance metrics, including open-circuit voltage (V_{oc}), short-circuit current density (J_{sc}), fill factor (FF), and power conversion efficiency (PCE). Initially, N-I-P had a slight performance advantage due to higher V_{oc} (1.180 V vs. 1.145 V in P-I-N).

Under extreme defect conditions ($N_R = N_{DA} = N_{DT} = N_{AT} = 10^{16}$ cm⁻³), N-I-P suffered a catastrophic PCE drop to 2.430%, while P-I-N retained at PCE 13.175%. This suggests that P-I-N structures exhibit better defect tolerance, making them more suitable for long-term stability in defect-prone conditions.

Conclusion

Perovskite solar cells (PSCs) are a promising technology in the field of solar energy due to their low cost, high efficiency, and ease of manufacturing. Their efficiency has seen a significant increase from 3.8% to 25.8% within a short time frame, surpassing many established technologies like silicon, cadmium telluride, and gallium arsenide-based solar cells. However, their stability remains a challenge compared to commercial solar cells, as perovskite materials contain elements prone to degradation due to environmental factors such as humidity, temperature, and light exposure. Furthermore, there are still obstacles to the widespread commercialization of this technology, including the need to scale up production to fabricate large-area modules efficiently, as well as concerns regarding the toxicity of materials and manufacturing processes involved.

To address these challenges, the Solar Cell Capacitance Simulator (SCAPS) was used in this study to analyze the stability of perovskite solar cells. The focus was on studying the impact of defects caused by degradation processes in both P-I-N and N-I-P structures, aiming to understand the relationship between defect formation and device performance degradation. The findings revealed that defect density plays a critical role in influencing performance metrics such as open-circuit voltage (V_{oc}), short-circuit current density (J_{sc}), fill factor (FF), and power conversion efficiency (PCE). Under extreme defect conditions, the N-I-P structure suffered a significant drop in PCE to 2.430%, while the P-I-N structure maintained a PCE of 13.175%. These results suggest that P-I-N structures exhibit better defect tolerance, making them more suitable for long-term stability in defect-prone environments. Therefore, P-I-N structures could be the optimal choice for future perovskite solar cell technologies.

Bibliography

- [1] M. Thirugnanasambandam, S. Iniyan, and R. Goic, "A review of solar thermal technologies," *Renewable and Sustainable Energy Reviews*, vol. 14, pp. 312–322, 1 2010.
- [2] T. A. Chowdhury, M. A. B. Zafar, M. S.-U. Islam, M. Shahinuzzaman, M. A. Islam, and M. U. Khandaker, "Stability of perovskite solar cells: issues and prospects," *RSC Advances*, vol. 13, pp. 1787–1810, 1 2023.
- [3] P. Wang, Y. Wu, B. Cai, Q. Ma, X. Zheng, and W. H. Zhang, "Solution-processable perovskite solar cells toward commercialization: Progress and challenges," *Advanced Functional Materials*, vol. 29, 11 2019.
- [4] A. Rajagopal, K. Yao, and A. K. Jen, "Toward perovskite solar cell commercialization: A perspective and research roadmap based on interfacial engineering," *Advanced Materials*, vol. 30, p. 1800455, 8 2018.
- [5] H. C. Fu, V. Ramalingam, H. Kim, C. H. Lin, X. Fang, H. N. Alshareef, and J. H. He, "Mxene-contacted silicon solar cells with 11,5% efficiency," *Advanced Energy Materials*, vol. 9, p. 1900180, 6 2019.
- [6] W. Shockley and H. J. Queisser, "Detailed balance limit of efficiency of p-n junction solar cells," *Journal of Applied Physics*, vol. 32, pp. 510–519, 3 1961.
- [7] H. Min, D. Y. Lee, J. Kim, G. Kim, K. S. Lee, J. Kim, M. J. Paik, Y. K. Kim, K. S. Kim, M. G. Kim, T. J. Shin, and S. I. Seok, "Perovskite solar cells with atomically coherent interlayers on sno2 electrodes," *Nature 2021 598:7881*, vol. 598, pp. 444–450, 10 2021.
- [8] P. K. Kung, M. H. Li, P. Y. Lin, Y. H. Chiang, C. R. Chan, T. F. Guo, and P. Chen, "A review of inorganic hole transport materials for perovskite solar cells," *Advanced Materials Interfaces*, vol. 5, p. 1800882, 11 2018.
- [9] Y. Yang, M. T. Hoang, A. Bhardwaj, M. Wilhelm, S. Mathur, and H. Wang, "Perovskite solar cells based self-charging power packs: Fundamentals, applications and challenges," *Nano Energy*, vol. 94, 4 2022.

- [10] H. Zhang, Y. Lu, W. Han, J. Zhu, Y. Zhang, and W. Huang, "Solar energy conversion and utilization: Towards the emerging photo-electrochemical devices based on perovskite photovoltaics," *Chemical Engineering Journal*, vol. 393, 8 2020.
- [11] B. Chen, Z. Yu, K. Liu, X. Zheng, Y. Liu, J. Shi, D. Spronk, P. N. Rudd, Z. Holman, and J. Huang, "Grain engineering for perovskite/silicon monolithic tandem solar cells with efficiency of 25.4vol. 3, pp. 177–190, 1 2019.
- [12] A. Kojima, K. Teshima, Y. Shirai, and T. Miyasaka, "Organometal halide perovskites as visible-light sensitizers for photovoltaic cells," *Journal of the American Chemical Society*, vol. 131, pp. 6050–6051, 5 2009.
- [13] M. Jung, Y. C. Kim, N. J. Jeon, W. S. Yang, J. Seo, J. H. Noh, and S. I. Seok, "Thermal stability of cuscn hole conductor-based perovskite solar cells," *ChemSusChem*, vol. 9, pp. 2592–2596, 9 2016.
- [14] H. S. Jung and N. G. Park, "Perovskite solar cells: From materials to devices," *Small*, vol. 11, pp. 10–25, 1 2015.
- [15] H. F. Kay and P. C. Bailey, "Structure and properties of catio3," *urn:issn:0365-110X*, vol. 10, pp. 219–226, 3 1957.
- [16] Q. Zhang, F. Hao, J. Li, Y. Zhou, Y. Wei, and H. Lin, "Perovskite solar cells: must lead be replaced and can it be done?" *Science and Technology of Advanced Materials*, vol. 19, pp. 425–442, 12 2018.
- [17] V. M. Goldschmidt, "Die gesetze der krystallochemie," *Die Naturwissenschaften*, vol. 14, pp. 477–485, 5 1926.
- [18] A. Poglitsch and D. Weber, "Dynamic disorder in methyla-trihalogen-oplumbates (ii) observed by millimeter-wave spectroscopy," *The Journal of Chemical Physics*, vol. 87, pp. 6373–6378, 12 1987.
- [19] C. Quarti, E. Mosconi, J. M. Ball, V. D'Innocenzo, C. Tao, S. Pathak, H. J. Snaith, A. Petrozza, and F. D. Angelis, "Structural and optical properties of methylammonium lead iodide across the tetragonal to cubic phase transition: implications for perovskite solar cells," *Energy and Environmental Science*, vol. 9, pp. 155–163, 1 2016.
- [20] B. Yu, S. Tan, D. Li, and Q. Meng, "The stability of inorganic perovskite solar cells: From materials to devices," *Materials Futures*, vol. 2, 9 2023.
- [21] R. Sharma, A. Sharma, S. Agarwal, and M. S. Dhaka, "Stability and efficiency issues, solutions and advancements in perovskite solar cells: A review," *Solar Energy*, vol. 244, pp. 516–535, 9 2022.

- [22] M. I. H. Ansari, A. Qurashi, and M. K. Nazeeruddin, "Frontiers, opportunities, and challenges in perovskite solar cells: A critical review," *Journal of Photochemistry and Photobiology C: Photochemistry Reviews*, vol. 35, pp. 1–24, 6 2018.
- [23] S. Sze and K. K. Ng, *Physics of Semiconductor Devices*. Wiley, 10 2006.
- [24] A. M. Fehr, A. Agrawal, F. Mandani, C. L. Conrad, Q. Jiang, S. Y. Park, O. Alley, B. Li, S. Sidhik, I. Metcalf, C. Botello, J. L. Young, J. Even, J. C. Blancon, T. G. Deutsch, K. Zhu, S. Albrecht, F. M. Toma, M. Wong, and A. D. Mohite, "Integrated halide perovskite photoelectrochemical cells with solar-driven water-splitting efficiency of 20.8%," *Nature Communications*, vol. 14, pp. 3797–3808, 12 2023.
- [25] K. A. Bush, A. F. Palmstrom, Z. J. Yu, M. Boccard, R. Cheacharoen, J. P. Mailoa, D. P. McMeekin, R. L. Hoye, C. D. Bailie, T. Leijtens, I. M. Peters, M. C. Minichetti, N. Rolston, R. Prasanna, S. Sofia, D. Harwood, W. Ma, F. Moghadam, H. J. Snaith, T. Buonassisi, Z. C. Holman, S. F. Bent, and M. D. McGehee, "23.6%-efficient monolithic perovskite/silicon tandem solar cells with improved stability," *Nature Energy 2017 2:4*, vol. 2, pp. 1–7, 2 2017.
- [26] G. Hodes, "Perovskite-based solar cells: A review of recent progress," *Science*, vol. 342, pp. 317–318, 2013.
- [27] M. A. Loi and J. C. Hummelen, "Stability of perovskite solar cells," *Nat. Mater.*, vol. 12, pp. 1087–1089, 2013.
- [28] Y. S. A. Kojima, K. Teshima and T. Miyasaka, "Organometal halide perovskites as visible-light sensitizers for photovoltaic cells," *J. Am. Chem. Soc.*, vol. 131, pp. 6050–6051, 2009.
- [29] P. Gao, Z. Xue, P. Qin, A. Chandiran, B. Liu, M. Nazeeruddin, and M. Graetzel, "Mesoscopic ch(3)nh(3)pbi(3)/tio(2) heterojunction solar cells." *Journal of the American Chemical Society*, vol. 134, pp. 17396–9, 102012.
- [30] H.-S. Kim, C.-R. Lee, J.-H. Im, K.-B. Lee, T. Moehl, A. Marchioro, S.-J. Moon, R. Humphry-Baker, J.-H. Yum, J. E. Moser *et al.*, "Lead iodide perovskite sensitized all-solid-state submicron thin film mesoscopic solar cell with efficiency exceeding 9%," *Scientific reports*, vol. 2, no. 1, p. 591, 2012.
- [31] J.-H. Im, C.-R. Lee, J.-W. Lee, S.-W. Park, and N.-G. Park, "6.5perovskite quantum-dot-sensitized solar cell," *Nanoscale*, vol. 3, pp. 4088–93, 09 2011.
- [32] M. Lee, J. Teuscher, T. Miyasaka, T. Murakami, and J.-H. Im, "Efficient hybrid solar cells based on meso-superstructured organometal halide perovskites," *Science (New York, N.Y.)*, vol. 338, 10 2012.

- [33] J. Noh, S. H. Im, J. H. Heo, T. Mandal, and S. I. Seok, "Chemical management for colorful, efficient, and stable inorganic–organic hybrid nanostructured solar cells," *Nano letters*, vol. 13, 03 2013.
- [34] N. J. Jeon, J. H. Noh, W. S. Yang, Y. C. Kim, S. Ryu, J. Seo, and S. I. Seok, "Compositional engineering of perovskite materials for high-performance solar cells," *Nature*, vol. 517, no. 7535, pp. 476–480, 2015.
- [35] N. Jeon, J. Noh, W. Yang, Y. Kim, S. Ryu, J. Seo, and S. H. Im, "Compositional engineering of perovskite materials for high-performance solar cells," *Nature*, vol. 517, 01 2015.
- [36] W. Chen, Y. Zhou, G. Chen, Y. Wu, B. Tu, F. Liu, L. Huang, A. M. C. Ng, A. Djurišić, and Z. He, "Alkali chlorides for the suppression of the interfacial recombination in inverted planar perovskite solar cells," *Advanced Energy Materials*, vol. 9, 03 2019.
- [37] J. Song, L. Zhao, S. Huang, X. Yan, Q. Qiu, Y. Zhao, L. Zhu, Y. Qiang, H. Li, and G. Li, "A p-p homojunction-enhanced hole transfer in inverted planar perovskite solar cells," *ChemSusChem*, vol. 14, 01 2021.
- [38] H. Min, D. Y. Lee, J. Kim, G. Kim, K. S. Lee, J. Kim, M. J. Paik, Y. K. Kim, K. S. Kim, M. G. Kim *et al.*, "Perovskite solar cells with atomically coherent interlayers on sno2 electrodes," *Nature*, vol. 598, no. 7881, pp. 444–450, 2021.
- [39] T. A. Berhe, W.-N. Su, C.-H. Chen, C.-J. Pan, J.-H. Cheng, H.-M. Chen, M.-C. Tsai, L.-Y. Chen, A. A. Dubale, and B.-J. Hwang, "Organometal halide perovskite solar cells: degradation and stability," *Energy & Environmental Science*, vol. 9, no. 2, pp. 323–356, 2016.
- [40] P.-K. Kung, M.-H. Li, P.-Y. Lin, Y.-H. Chiang, C.-R. Chan, T.-F. Guo, and P. Chen, "A review of inorganic hole transport materials for perovskite solar cells," *Advanced Materials Interfaces*, vol. 5, no. 22, p. 1800882, 2018.
- [41] K. K. Bass, R. E. McAnally, S. Zhou, P. I. Djurovich, M. E. Thompson, and B. C. Melot, "Influence of moisture on the preparation, crystal structure, and photophysical properties of organohalide perovskites," *Chemical Communications*, vol. 50, no. 99, pp. 15819–15822, 2014.
- [42] C. C. Boyd, R. Cheacharoen, T. Leijtens, and M. D. McGehee, "Understanding degradation mechanisms and improving stability of perovskite photovoltaics," *Chemical reviews*, vol. 119, no. 5, pp. 3418–3451, 2018.

- [43] M. K. Rao, D. Sangeetha, M. Selvakumar, Y. Sudhakar, and M. Mahesha, "Review on persistent challenges of perovskite solar cells' stability," *Solar Energy*, vol. 218, pp. 469– 491, 2021.
- [44] F. Baumann, S. R. Raga, and M. Lira-Cantú, "Monitoring the stability and degradation mechanisms of perovskite solar cells by in situ and operando characterization," *APL Energy*, vol. 1, no. 1, 2023.
- [45] C. Harito, S. A. Abrori, M. Khalil, B. Yuliarto, and S. Erten-Ela, "Current progress of perovskite solar cells stability with bibliometric study," *Current Opinion in Colloid & Interface Science*, p. 101862, 2024.
- [46] J. A. Christians, P. A. Miranda Herrera, and P. V. Kamat, "Transformation of the excited state and photovoltaic efficiency of ch3nh3pbi3 perovskite upon controlled exposure to humidified air," *Journal of the American Chemical Society*, vol. 137, no. 4, pp. 1530–1538, 2015.
- [47] A. M. Leguy, Y. Hu, M. Campoy-Quiles, M. I. Alonso, O. J. Weber, P. Azarhoosh, M. Van Schilfgaarde, M. T. Weller, T. Bein, J. Nelson *et al.*, "Reversible hydration of ch3nh3pbi3 in films, single crystals, and solar cells," *Chemistry of Materials*, vol. 27, no. 9, pp. 3397–3407, 2015.
- [48] T. Leijtens, K. Bush, R. Cheacharoen, R. Beal, A. Bowring, and M. D. McGehee, "Towards enabling stable lead halide perovskite solar cells; interplay between structural, environmental, and thermal stability," *Journal of Materials Chemistry A*, vol. 5, no. 23, pp. 11483–11500, 2017.
- [49] W. Chi and S. K. Banerjee, "Achieving resistance against moisture and oxygen for perovskite solar cells with high efficiency and stability," *Chemistry of Materials*, vol. 33, no. 12, pp. 4269–4303, 2021.
- [50] M. L. De Giorgi, S. Milanese, A. Klini, and M. Anni, "Environment-induced reversible modulation of optical and electronic properties of lead halide perovskites and possible applications to sensor development: a review," *Molecules*, vol. 26, no. 3, p. 705, 2021.
- [51] Q.-M. Hong, R.-P. Xu, T.-Y. Jin, J.-X. Tang, and Y.-Q. Li, "Unraveling the light-induced degradation mechanism of ch3nh3pbi3 perovskite films," *Organic Electronics*, vol. 67, pp. 19–25, 2019.
- [52] E. J. Juarez-Perez, L. K. Ono, M. Maeda, Y. Jiang, Z. Hawash, and Y. Qi, "Photodecomposition and thermal decomposition in methylammonium halide lead perovskites and inferred design principles to increase photovoltaic device stability," *Journal of Materials Chemistry A*, vol. 6, no. 20, pp. 9604–9612, 2018.

- [53] Z. Hawash, L. K. Ono, S. R. Raga, M. V. Lee, and Y. Qi, "Air-exposure induced degradation of perovskite solar cells," *Chemistry of Materials*, vol. 27, no. 2, pp. 562–569, 2015.
- [54] L. K. Ono, P. Schulz, J. J. Endres, G. O. Nikiforov, Y. Kato, A. Kahn, and Y. Qi, "Airexposure induced degradation of perovskite solar cells," *Journal of Physical Chemistry Letters*, vol. 5, no. 8, pp. 1374–1379, 2014.
- [55] D. A. Mengistie, M. A. Ibrahem, P.-C. Wang, and C.-W. Chu, "Highly conductive pedot:pss treated with formic acid for ito-free polymer solar cells," *ACS Applied Materials & Interfaces*, vol. 6, no. 4, pp. 2292–2299, 2014.
- [56] C.-H. Chiang, Z.-L. Tseng, and C.-G. Wu, "High-efficiency perovskite solar cells with all-solution-processed hole transport layers," *Journal of Materials Chemistry A*, vol. 2, no. 42, pp. 15897–15903, 2014.
- [57] Y.-J. Jeon, S. Lee, R. Kang, J.-E. Kim, J.-S. Yeo, S.-H. Lee, S.-S. Kim, J.-M. Yun, and D.-Y. Kim, "High-efficiency inverted organic solar cells using a solution-processed aluminum-doped zinc oxide buffer layer," *Scientific Reports*, vol. 4, p. 6953, 2014.
- [58] M. Jørgensen, K. Norrman, and F. C. Krebs, "Stability/degradation of polymer solar cells," *Solar Energy Materials and Solar Cells*, vol. 92, no. 7, pp. 686–714, 2008.
- [59] M. P. de Jong, L. J. van IJzendoorn, and M. J. A. de Voigt, "Stability/degradation of polymer solar cells," *Applied Physics Letters*, vol. 77, no. 14, pp. 2255–2257, 2000.
- [60] S. R. Dupont, M. Oliver, F. C. Krebs, and R. H. Dauskardt, "Stability/degradation of polymer solar cells," *Solar Energy Materials and Solar Cells*, vol. 97, pp. 171–175, 2012.
- [61] Z. Liu and H. He, "Counter electrode materials for organic-inorganic perovskite solar cells," *Nanostructured Materials for Next-Generation Energy Storage and Conversion: Photovoltaic and Solar Energy*, pp. 165–225, 2019.
- [62] P. Docampo, J. M. Ball, M. Darwich, G. E. Eperon, and H. J. Snaith, "Efficient organometal trihalide perovskite planar-heterojunction solar cells on flexible polymer substrates," *Nature Communications*, vol. 4, p. 2761, 2013.
- [63] H. J. Snaith, "The role of hole transport layer in perovskite solar cells," *Journal of Physical Chemistry Letters*, vol. 4, no. 21, pp. 3623–3630, 2013.
- [64] C. Li, A. Guerrero, S. Huettner, and J. Bisquert, "Unravelling the role of vacancies in lead halide perovskite through electrical switching of photoluminescence," *Nature Communications*, vol. 9, no. 1, p. 5113, 2018.

- [65] Q. Jeangros, M. Duchamp, J. Werner, M. Kruth, R. Dunin-Borkowski, B. Niesen, C. Ballif, and A. Hessler-Wyser, "In situ tem analysis of organic-inorganic metal-halide perovskite solar cells under electrical bias," *Nano Letters*, vol. 16, no. 11, pp. 7013–7018, 2016.
- [66] M.-c. Kim, N. Ahn, D. Cheng, M. Xu, S.-Y. Ham, X. Pan, S. J. Kim, Y. Luo, D. P. Fenning, D. H. S. Tan *et al.*, "Imaging real-time amorphization of hybrid perovskite solar cells under bias," *Journal of Materials Chemistry A*, vol. 11, no. 12, pp. 1234–1245, 2023.
- [67] D. Kim, J. S. Yun, P. Sharma, D. S. Lee, J. Kim, A. M. Soufiani, S. Huang, M. A. Green, A. W. Ho-Baillie, and J. Seidel, "Light-and bias-induced structural variations in metal halide perovskites," *Nature communications*, vol. 10, no. 1, p. 444, 2019.
- [68] B. Hailegnaw, S. Kirmayer, E. Edri, G. Hodes, and D. Cahen, "Rain on methylammonium lead iodide based perovskites: possible environmental effects of perovskite solar cells," *The journal of physical chemistry letters*, vol. 6, no. 9, pp. 1543–1547, 2015.
- [69] M. H. Miah, M. U. Khandaker, M. B. Rahman, M. Nur-E-Alam, and M. A. Islam, "Band gap tuning of perovskite solar cells for enhancing the efficiency and stability: issues and prospects," *RSC advances*, vol. 14, no. 23, pp. 15876–15906, 2024.
- [70] Z. Xiao, L. Zhao, N. L. Tran, Y. L. Lin, S. H. Silver, R. A. Kerner, N. Yao, A. Kahn, G. D. Scholes, and B. P. Rand, "Mixed-halide perovskites with stabilized bandgaps," *Nano letters*, vol. 17, no. 11, pp. 6863–6869, 2017.
- [71] E. T. Hoke, D. J. Slotcavage, E. R. Dohner, A. R. Bowring, H. I. Karunadasa, and M. D. McGehee, "Reversible photo-induced trap formation in mixed-halide hybrid perovskites for photovoltaics," *Chemical Science*, vol. 6, no. 1, pp. 613–617, 2015.
- [72] Y. Wang, X. Quintana, J. Kim, X. Guan, L. Hu, C.-H. Lin, B. T. Jones, W. Chen, X. Wen, H. Gao *et al.*, "Phase segregation in inorganic mixed-halide perovskites: from phenomena to mechanisms," *Photonics research*, vol. 8, no. 11, pp. A56–A71, 2020.
- [73] M. Abdi-Jalebi, Z. Andaji-Garmaroudi, S. Cacovich, C. Stavrakas, B. Philippe, J. M. Richter, M. Alsari, E. P. Booker, E. M. Hutter, A. J. Pearson *et al.*, "Maximizing and stabilizing luminescence from halide perovskites with potassium passivation," *Nature*, vol. 555, no. 7697, pp. 497–501, 2018.
- [74] S. Banerjee, C. S. Gerke, and V. S. Thoi, "Guiding co2rr selectivity by compositional tuning in the electrochemical double layer," *Accounts of Chemical Research*, vol. 55, no. 4, pp. 504–515, 2022.

- [75] L. Mao, C. C. Stoumpos, and M. G. Kanatzidis, "Two-dimensional hybrid halide perovskites: principles and promises," *Journal of the American Chemical Society*, vol. 141, no. 3, pp. 1171–1190, 2018.
- [76] S. Bao, H. Yang, H. Fan, J. Zhang, Z. Wei, C. Cui, and Y. Li, "Volatilizable solid additive-assisted treatment enables organic solar cells with efficiency over 18.8% and fill factor exceeding 80%," *Advanced Materials*, vol. 33, no. 48, p. 2105301, 2021.
- [77] K. Hong, Q. Van Le, S. Y. Kim, and H. W. Jang, "Low-dimensional halide perovskites: review and issues," *Journal of Materials Chemistry C*, vol. 6, no. 9, pp. 2189–2209, 2018.
- [78] M. T. Hörantner, P. K. Nayak, S. Mukhopadhyay, K. Wojciechowski, C. Beck, D. McMeekin, B. Kamino, G. E. Eperon, and H. J. Snaith, "Shunt-blocking layers for semitransparent perovskite solar cells," *Advanced materials interfaces*, vol. 3, no. 10, p. 1500837, 2016.
- [79] D. Abdallaoui, A. Meftah, S. Angar, M. Abdallaoui, S. Barkat, W. Laiadi, A. Meftah, and N. Sengouga, "Study by numerical simulation of the effect of instability-induced defects by illumination, thermal, and bias stresses in perovskite solar cells and approaches to reduce their degradation degree," *Journal of Electronic Materials*, pp. 1–12, 2024.
- [80] S. Castro-Hermosa, M. Top, J. Dagar, J. Fahlteich, and T. M. Brown, "Quantifying performance of permeation barrier—encapsulation systems for flexible and glass-based electronics and their application to perovskite solar cells," *Advanced Electronic Materials*, vol. 5, no. 10, p. 1800978, 2019.
- [81] Z. Yang, B. H. Babu, S. Wu, T. Liu, S. Fang, Z. Xiong, L. Han, and W. Chen, "Review on practical interface engineering of perovskite solar cells: from efficiency to stability," *Solar Rrl*, vol. 4, no. 2, p. 1900257, 2020.
- [82] H. Chen, Q. Luo, T. Liu, J. Ren, S. Li, M. Tai, H. Lin, H. He, J. Wang, and N. Wang, "Goethite quantum dots as multifunctional additives for highly efficient and stable perovskite solar cells," *Small*, vol. 15, no. 47, p. 1904372, 2019.
- [83] B. Chen, P. N. Rudd, S. Yang, Y. Yuan, and J. Huang, "Imperfections and their passivation in halide perovskite solar cells," *Chemical Society Reviews*, vol. 48, no. 14, pp. 3842–3867, 2019.
- [84] L. M. Pazos-Outón, T. P. Xiao, and E. Yablonovitch, "Fundamental efficiency limit of lead iodide perovskite solar cells," *The journal of physical chemistry letters*, vol. 9, no. 7, pp. 1703–1711, 2018.

- [85] W. Zhang, S. Pathak, N. Sakai, T. Stergiopoulos, P. K. Nayak, N. K. Noel, A. A. Haghighirad, V. M. Burlakov, D. W. Dequilettes, A. Sadhanala *et al.*, "Enhanced optoelectronic quality of perovskite thin films with hypophosphorous acid for planar heterojunction solar cells," *Nature communications*, vol. 6, no. 1, p. 10030, 2015.
- [86] W. Tress, N. Marinova, T. Moehl, S. M. Zakeeruddin, M. K. Nazeeruddin, and M. Grätzel, "Understanding the rate-dependent j–v hysteresis, slow time component, and aging in ch 3 nh 3 pbi 3 perovskite solar cells: the role of a compensated electric field," *Energy & Environmental Science*, vol. 8, no. 3, pp. 995–1004, 2015.
- [87] T. S. Sherkar, C. Momblona, L. Gil-Escrig, J. Avila, M. Sessolo, H. J. Bolink, and L. J. A. Koster, "Recombination in perovskite solar cells: significance of grain boundaries, interface traps, and defect ions," *ACS energy letters*, vol. 2, no. 5, pp. 1214–1222, 2017.
- [88] C. Bi, X. Zheng, B. Chen, H. Wei, and J. Huang, "Spontaneous passivation of hybrid perovskite by sodium ions from glass substrates: mysterious enhancement of device efficiency revealed," *ACS Energy Letters*, vol. 2, no. 6, pp. 1400–1406, 2017.
- [89] D. d. Quilettes, S. Vorpahl, S. Stranks, H. Nagaoka, G. Eperon, M. Ziffer, H. Snaith, and D. Ginger, "Impact of microstructure on local carrier lifetime in perovskite solar cells," *Science*, vol. 348, no. 6235, pp. 683–686, 2015.
- [90] J. Chen and N.-G. Park, "Causes and solutions of recombination in perovskite solar cells," *Advanced Materials*, vol. 31, no. 47, p. 1803019, 2019.
- [91] N. K. Elumalai and A. Uddin, "Hysteresis in organic-inorganic hybrid perovskite solar cells," *Solar Energy Materials and Solar Cells*, vol. 157, pp. 476–509, 2016.
- [92] L. Duan and A. Uddin, "Defects and stability of perovskite solar cells: a critical analysis," *Materials Chemistry Frontiers*, vol. 6, no. 4, pp. 400–417, 2022.
- [93] J. Prakash, A. Singh, G. Sathiyan, R. Ranjan, A. Singh, A. Garg, and R. K. Gupta, "Progress in tailoring perovskite based solar cells through compositional engineering: Materials properties, photovoltaic performance and critical issues," *Materials today energy*, vol. 9, pp. 440–486, 2018.
- [94] B. Liu, R. Cui, H. Huang, X. Guo, J. Dong, H. Yao, Y. Li, D. Zhao, J. Wang, J. Zhang *et al.*, "Elucidating the mechanisms underlying pcbm enhancement of ch 3 nh 3 pbi 3 perovskite solar cells using gixrd and xafs," *Journal of Materials Chemistry A*, vol. 8, no. 6, pp. 3145–3153, 2020.
- [95] Y. Yin, S. Fu, S. Zhou, Y. Song, L. Li, M. Zhang, J. Wang, P. Mariyappan, S. M. Alshehri, T. Ahamad *et al.*, "Efficient and stable ideal bandgap perovskite solar cell achieved by

- a small amount of tin substituted methylammonium lead iodide," *Electronic Materials Letters*, vol. 16, pp. 224–230, 2020.
- [96] M. L. Agiorgousis, Y.-Y. Sun, H. Zeng, and S. Zhang, "Strong covalency-induced recombination centers in perovskite solar cell material ch3nh3pbi3," *Journal of the American Chemical Society*, vol. 136, no. 41, pp. 14570–14575, 2014.
- [97] A. Dualeh, T. Moehl, N. Tétreault, J. Teuscher, P. Gao, M. K. Nazeeruddin, and M. Gratzel, "Impedance spectroscopic analysis of lead iodide perovskite-sensitized solid-state solar cells," *ACS nano*, vol. 8, no. 1, pp. 362–373, 2014.
- [98] W. Baker and W. Ollis, "Meso-ionic compounds," *Quarterly Reviews, Chemical Society*, vol. 11, no. 1, pp. 15–29, 1957.
- [99] S.-H. Turren-Cruz, M. Saliba, M. T. Mayer, H. Juárez-Santiesteban, X. Mathew, L. Nienhaus, W. Tress, M. P. Erodici, M.-J. Sher, M. G. Bawendi *et al.*, "Enhanced charge carrier mobility and lifetime suppress hysteresis and improve efficiency in planar perovskite solar cells," *Energy & Environmental Science*, vol. 11, no. 1, pp. 78–86, 2018.
- [100] M. Saliba, T. Matsui, K. Domanski, J.-Y. Seo, A. Ummadisingu, S. M. Zakeeruddin, J.-P. Correa-Baena, W. R. Tress, A. Abate, A. Hagfeldt *et al.*, "Incorporation of rubidium cations into perovskite solar cells improves photovoltaic performance," *Science*, vol. 354, no. 6309, pp. 206–209, 2016.
- [101] Y. Guo, F. Zhao, J. Tao, J. Jiang, J. Zhang, J. Yang, Z. Hu, and J. Chu, "Efficient and hole-transporting-layer-free cspbi2br planar heterojunction perovskite solar cells through rubidium passivation," *ChemSusChem*, vol. 12, no. 5, pp. 983–989, 2019.
- [102] F. Zhang, B. Yang, X. Mao, R. Yang, L. Jiang, Y. Li, J. Xiong, Y. Yang, R. He, W. Deng *et al.*, "Perovskite ch3nh3pbi3–x br x single crystals with charge-carrier lifetimes exceeding 260 μ s," *ACS applied materials & interfaces*, vol. 9, no. 17, pp. 14827–14832, 2017.
- [103] W. S. Yang, B.-W. Park, E. H. Jung, N. J. Jeon, Y. C. Kim, D. U. Lee, S. S. Shin, J. Seo, E. K. Kim, J. H. Noh *et al.*, "Iodide management in formamidinium-lead-halide-based perovskite layers for efficient solar cells," *Science*, vol. 356, no. 6345, pp. 1376–1379, 2017.
- [104] V. L. Pool, A. Gold-Parker, M. D. McGehee, and M. F. Toney, "Chlorine in pbcl2-derived hybrid-perovskite solar absorbers," *Chemistry of Materials*, vol. 27, no. 21, pp. 7240–7243, 2015.
- [105] B. R. Stockwell, "Exploring biology with small organic molecules," *Nature*, vol. 432, no. 7019, pp. 846–854, 2004.

- [106] J. Park, J. Kim, H.-S. Yun, M. J. Paik, E. Noh, H. J. Mun, M. G. Kim, T. J. Shin, and S. I. Seok, "Controlled growth of perovskite layers with volatile alkylammonium chlorides," *Nature*, vol. 616, no. 7958, pp. 724–730, 2023.
- [107] D.-Y. Son, J.-W. Lee, Y. J. Choi, I.-H. Jang, S. Lee, P. J. Yoo, H. Shin, N. Ahn, M. Choi, D. Kim *et al.*, "Self-formed grain boundary healing layer for highly efficient ch3nh3pbi3 perovskite solar cells," *Nature Energy*, vol. 1, no. 7, pp. 1–8, 2016.
- [108] M. Long, T. Zhang, H. Zhu, G. Li, F. Wang, W. Guo, Y. Chai, W. Chen, Q. Li, K. S. Wong *et al.*, "Textured ch3nh3pbi3 thin film with enhanced stability for high performance perovskite solar cells," *Nano Energy*, vol. 33, pp. 485–496, 2017.
- [109] Y. Ma, S. Zhang, Y. Yi, L. Zhang, R. Hu, W. Liu, M. Du, L. Chu, J. Zhang, X. Li *et al.*, "Deep level defects passivated by small molecules for the enhanced efficiency and stability of inverted perovskite solar cells," *Journal of Materials Chemistry C*, vol. 10, no. 15, pp. 5922–5928, 2022.
- [110] G. Wang, L. Wang, J. Qiu, Z. Yan, C. Li, C. Dai, C. Zhen, K. Tai, W. Yu, and X. Jiang, "In situ passivation on rear perovskite interface for efficient and stable perovskite solar cells," *ACS applied materials & interfaces*, vol. 12, no. 6, pp. 7690–7700, 2020.
- [111] F. Zhang, W. Shi, J. Luo, N. Pellet, C. Yi, X. Li, X. Zhao, T. J. S. Dennis, X. Li, S. Wang *et al.*, "Isomer-pure bis-pcbm-assisted crystal engineering of perovskite solar cells showing excellent efficiency and stability," *Advanced Materials*, vol. 29, no. 17, p. 1606806, 2017.
- [112] Z. Ni, C. Bao, Y. Liu, Q. Jiang, W.-Q. Wu, S. Chen, X. Dai, B. Chen, B. Hartweg, Z. Yu *et al.*, "Resolving spatial and energetic distributions of trap states in metal halide perovskite solar cells," *Science*, vol. 367, no. 6484, pp. 1352–1358, 2020.
- [113] F. Gao, Y. Zhao, X. Zhang, and J. You, "Recent progresses on defect passivation toward efficient perovskite solar cells," *Advanced Energy Materials*, vol. 10, no. 13, p. 1902650, 2020.
- [114] L. Meng, C. Sun, R. Wang, W. Huang, Z. Zhao, P. Sun, T. Huang, J. Xue, J.-W. Lee, C. Zhu *et al.*, "Tailored phase conversion under conjugated polymer enables thermally stable perovskite solar cells with efficiency exceeding 21%," *Journal of the American Chemical Society*, vol. 140, no. 49, pp. 17255–17262, 2018.
- [115] A. Krishna, H. Zhang, Z. Zhou, T. Gallet, M. Dankl, O. Ouellette, F. T. Eickemeyer, F. Fu, S. Sanchez, M. Mensi *et al.*, "Nanoscale interfacial engineering enables highly stable and efficient perovskite photovoltaics," *Energy & Environmental Science*, vol. 14, no. 10, pp. 5552–5562, 2021.

- [116] K. Liu, S. Chen, J. Wu, H. Zhang, M. Qin, X. Lu, Y. Tu, Q. Meng, and X. Zhan, "Fullerene derivative anchored sno 2 for high-performance perovskite solar cells," *Energy & Environmental Science*, vol. 11, no. 12, pp. 3463–3471, 2018.
- [117] S. Sonmezoglu and S. Akin, "Suppression of the interface-dependent nonradiative recombination by using 2-methylbenzimidazole as interlayer for highly efficient and stable perovskite solar cells," *Nano Energy*, vol. 76, p. 105127, 2020.
- [118] K. Choi, J. Lee, H. I. Kim, C. W. Park, G.-W. Kim, H. Choi, S. Park, S. A. Park, and T. Park, "Thermally stable, planar hybrid perovskite solar cells with high efficiency," *Energy & Environmental Science*, vol. 11, no. 11, pp. 3238–3247, 2018.
- [119] J. Deng, X. Yang, and P. Wang, "Study on the second-order transfer function models for dynamic tests of flat-plate solar collectors part i: A proposed new model and a fitting methodology," *Solar Energy*, vol. 114, pp. 418–426, 2015.
- [120] X. Yang, C. Liu, B. D. Walker, and P. Ren, "Accurate description of molecular dipole surface with charge flux implemented for molecular mechanics," *The Journal of Chemical Physics*, vol. 153, no. 6, 2020.
- [121] A. Niemegeers, M. Burgelman, K. Decock, J. Verschraegen, and S. Degrave, "Scaps manual," *University of Gent*, vol. 13, pp. 1–155, 2014.
- [122] W.-J. Yin, T. Shi, and Y. Yan, "Unusual defect physics in ch3nh3pbi3 perovskite solar cell absorber," *Applied physics letters*, vol. 104, no. 6, 2014.
- [123] S. J. Lee, H. P. Kim, A. R. bin Mohd Yusoff, and J. Jang, "Organic photovoltaic with pedot: Pss and v2o5 mixture as hole transport layer," *Solar energy materials and solar cells*, vol. 120, pp. 238–243, 2014.
- [124] F. Azri, "Study of hybrid organic-inorganic solar cells based on perovskite materials," *PhD Thesis*, vol. University of Biskra, 2022.
- [125] F. Eslami and S. Matloub, "Advancing perovskite solar cell performance: Enhanced efficiency and stability through superimposed pbs qds," *Solar Energy*, vol. 265, p. 112152, 2023.
- [126] C.-H. Chiang, M. K. Nazeeruddin, M. Grätzel, and C.-G. Wu, "The synergistic effect of h 2 o and dmf towards stable and 20% efficiency inverted perovskite solar cells," *Energy & Environmental Science*, vol. 10, no. 3, pp. 808–817, 2017.
- [127] S.-A. Kim, H. S. Kim, W. Lee, N. J. Jeon, J. Lim, and T.-Y. Yang, "Improvement of stability of perovskite solar cells with pbs buffer layer formed by solution process," *Applied Surface Science*, vol. 626, p. 157286, 2023.

[128] E. Almuqoddas, W. Budiawan, I. Paramudita, B. Yuliarto, Y. Firdaus *et al.*, "Near fundamental limit performance of inverted perovskite solar cells with anti-reflective coating integration," *Results in Optics*, vol. 16, p. 100670, 2024.

REPUBLIQUE ALGERIENNE DEMOCRATIQUE ET POPULAIRI MINISTERE DE L'ENSEIGNEMENT SUPERIEUR ET DE LA RECHERCHE SCIENTIFIQUE UNIVERSITE MOHAMED KHIDER - BISKRA

(ma)

الجمهورية الحزائرية الديمقراطية الشعبية وزارة التعليم العالي والبحث العلمي جأمعنة محمط حيضر مسركرة كلية العلوم الحششة

Faculté des SE

Département des Sciences de la matière

قسم : علوم المادة

Filière: Physique

<u>تصریح شرفیی</u>

خاص بالالتزام بقواعد النزاهة العلمية لإنجاز بحث

(ملحق القرار 1082 المؤرخ في 2021/12/27)

	معلة بالفنزياء	
13	قسم الرد	E
*	علوم المسادة)*/
	مة العلب وم اللينية	

	انا الممضني اسفله،
	السيد(ة): مسلمم المارة
الصفة: طالب سنة	تخصص فيزساء المواد
٤٠٥٤.٦.٩١٩٩٩ الصادرة بتاريخ:٨.تعبده ٥٨٥٩	الحامل(ة) لبطاقة التعريف الوطنية رقم:
قسم: علوم المادة	المسجل بكلية: العالج م الد فيقنة
	والمكلف بانجاز أعمال بحث : مذكرة
Stability usue in perover Kite Solar Cel	Die . 3. Com Panis on
between conventional and winested	Studines

أصرح بشرفي أني ألتزم بمراعاة المعايير العلمية والمنهجية ومعايير الأخلاقيات المهنية والنزاهة الأكاديمية المطلوبة في انجاز البحث المذكور أعلاه وفق ما ينص عليه القرار رقم 1082 المؤرخ في 2021/12/27 المتعلقة بالوقاية من السرقة العلمية ومكافحتها.

التاريخ: 22 هـ 2 م. .. 52 هـ 2 م

إمضاء المعنى بالأمر